Stony Brook University

The official electronic file of this thesis or dissertation is maintained by the University Libraries on behalf of The Graduate School at Stony Brook University.

Mechanism and Inhibition of the Enoyl-ACP Reductases from Biodefense and Emerging

Opportunistic Pathogens

A Dissertation Presented

by

Carla Neckles

to

The Graduate School

in Partial Fulfillment of the

Requirements

for the Degree of

Doctor of Philosophy

in

Chemistry

Stony Brook University

August 2014

Stony Brook University

The Graduate School

Carla Neckles

We, the dissertation committee for the above candidate for the

Doctor of Philosophy degree, hereby recommend

acceptance of this dissertation.

Peter J. Tonge – Dissertation Advisor
Professor of Chemistry, Stony Brook University

Isaac Carrico – Chairperson of Defense
Associate Professor of Chemistry, Stony Brook University

Kathlyn Parker – Committee Member of Defense
Professor of Chemistry, Stony Brook University

Jessica Seeliger – Committee Member of Defense
Assistant Professor of Pharmacological Sciences, Stony Brook University

Miguel Garcia-Diaz– Outside Member of Defense
Associate Professor of Pharmacological Sciences, Stony Brook University

This dissertation is accepted by the Graduate School

Charles Taber
Dean of the Graduate School

Abstract of the Dissertation

Mechanism and Inhibition of the Enoyl-ACP Reductases from Biodefense and Emerging

Opportunistic Pathogens

by

Carla Neckles

Doctor of Philosophy

in

Chemistry

Stony Brook University

2014

The enoyl-acyl-carrier-protein reductase (ENR) catalyzes the last reaction in the elongation cycle in the fatty acid biosynthesis type II (FAS-II) pathway. To date, there are four known ENR isoenzymes: FabI, FabK, FabL, and FabV. We have rigorously characterized the FabV ENR from *Burkholderia mallei* (*Bm*FabV) and have shown that this enzyme catalyzes substrate reduction via an ordered bi-bi mechanism, in which NADH binds first to the enzyme followed by the enoyl substrate [Lu, H. (2010) *Biochemistry* 49, 1281–1289]. However, this pathogen contains both FabI and FabV ENRs, and mechanistic insights into ENR substrate recognition are lacking in pathogens that solely express the FabV ENR. Thus, we extended our mechanistic studies to the FabV ENR from *Yersinia pestis* (*Yp*FabV).

Here, steady-state kinetic analysis revealed that *Yp*FabV catalyzes substrate reduction via a random bi-bi mechanism. Site-directed mutagenesis at the N-terminal end of the helical substrate binding loop revealed that residue T276 plays a key role in substrate specificity and

catalytic efficiency. Kinetic analysis and X-ray crystallographic structures demonstrated that the hydroxyl side chain of T276 is essential for hydrogen bonding interactions with NADH, while the methyl group provides favorable hydrophobic interactions with the acyl-coenzyme A (CoA) substrate.

Our studies also revealed that alteration of the substrate binding mechanism through site-directed mutagenesis may affect the mode of inhibition of *Yp*FabV. Structure-activity relationship (SAR) studies on the FabI ENR isoenzymes have been used as a platform to determine how slow binding inhibitors effect the transition and ground states of the drug-target complex. In turn, we were able to use rational inhibitor design to translate the slow-onset inhibition mechanism from FabI to FabV. Steady-state kinetic analysis of the P142W *Yp*FabV mutant revealed a gain of slow-onset inhibition for an inhibitor (**PT156**) that displays rapid-reversible binding kinetics for the wild-type enzyme. This is the first example of slow-onset inhibition of a FabV ENR.

Table of Contents

List of Figures

List of Tables

List of Schemes

List of Abbreviations

AccABCD	Acetyl-CoA carboxylase
AccAD	Carboxyltransferase component of AccABCD
AccB	Biotin carboxyl carrier protein
AccC	Biotin carboxylase component of AccABCD
ACP	Acyl carrier protein
acyl-ACP	Acylated acyl carrier protein
αKG	α-Ketoglutarate
ANOVA	A one-way analysis of variance
B. anthracis	*Bacillus anthracis*
B. mallei	*Burkholderia mallei*
B. pseudomallei	*Burkholderia pseudomallei*
B. subtilis	*Bacillus subtilis*
*Bm*FabV	ENR FabV from *Burkholderia mallei*
*Bp*FabI	ENR FabI from *Burkholderia pseudomallei*
*Bp*FabV	ENR FabV from *Burkholderia pseudomallei*
BSA	Bovine serum albumin
BSAT	Tier 1 Biological Select Agent or Toxin
C12-ecACP	*trans*-2-Dodecenoyl-ecACP
CDC	Centers for Disease Control and Prevention
CFU	Colony-forming unit
ClogP	Partition-coefficient of a compound

CoA	Coenzyme A
crot-CoA	Crotonyl coenzyme A
Da	Dalton
ddCoA	*trans-2*-Dodecenoyl-CoA
decCoA	*trans-2*-Decenoyl-CoA
DMPK	Drug metabolism and pharmacokinetics
DMSO	Dimethyl sulfoxide
DNA	Deoxyribonucleotide
DPE	Diphenyl ether-based inhibitor
E	Free enzyme
E. coli	*Escherichia coli*
EcFabI	ENR FabI from *Escherichia coli*
EDTA	Ethylenediaminetetraacetic acid
E-NADH	Enzyme-NADH complex
E-NAD$^+$	Enzyme-NAD$^+$ complex
ENR	Enoyl-ACP reductase
ESI	Electrospray ionization
F. tularensis	*Francisella tularensis*
FabA	β-Hydroxylacyl-ACP dehydratase
FabB	β-Ketoacyl-ACP synthase I
FabD	Malonyl-CoA:ACP transacylase
FabF	β-Ketoacyl-ACP synthase II
FabG	β-Ketoacyl-ACP reductase

FabH	β-Ketoacyl-ACP synthase III
FabI	Enoyl-ACP reductase
FabK	Enoyl-ACP reductase
FabL	Enoyl-ACP reductase
FabV	Enoyl-ACP reductase
FabZ	β-Hydroxylacyl-ACP dehydratase
FAS	Fatty acid synthase
FAS-I	Eukaryotic fatty acid biosynthesis
FAS-II	Bacterial fatty acid biosynthesis
FDA	Food and Drug Administration
FMN	Flavin mononucleotide, oxidized form
$FMNH_2$	Flavin mononucleotide, reduced form
HTS	High-throughput screening
IC_{50}	Half maximal inhibitory concentration
IDH1	Isocitrate dehydrogenase 1
IPTG	Isopropyl-1-thio-β-D-galactopyranoside
INH	Isoniazid
InhA	ENR from *Mycobacterium tuberculosis*
$INH-NAD^+$	Inhibitor adduct with NAD^+
KatG	Mycobacterial catalase-peroxidase
K_d	Dissociation constant
K_i	Inhibition constant
K_i^{app}	Apparent inhibition constant

K_i'	Apparent inhibition constant
K_M	Michaelis-Menten constant for the substrate
k_{obs}	Pseudo-first rate order constant
k_{off}	Dissociation rate constant
k_{on}	Association rate constant
LB	Luria-Bertani Agar
M. tuberculosis	*Mycobacterium tuberculosis*
MALDI-TOF	Matrix-assisted laser desorption/ionization time-of-flight mass spectrometer
MIC	Minimum inhibitory concentration determination
MRSA	Methicillin-resistant *Staphylococcus aureus*
NAC	N-acetylcysteamine
NAD^+	Nicotinamide adenine dinucleotide, oxidized form
NADH	Nicotinamide adenine dinucleotide, reduced form
NADPH	Nicotinamide adenine dinucleotide phosphate, reduced form
octCoA	*trans-2*-Octenoyl-CoA
oct-*ec*ACP	*trans*-2-octenoyl- *E. coli* ACP
OD_{600}	Optical density at 600 nm
P	Product
P. aeruginosa	*Pseudomonas aeruginosa*
*Pa*FabV	ENR FabV from *Pseudomonas aeruginosa*
PBS	Phosphate buffered saline
PCR	Polymerase chain reaction

PDB	Protein Data Bank
2-Pyr	2-Pyridone-based inhibitor
4-Pyr	4-Pyridone-based inhibitor
RMSD	Root-mean-square deviation
RND	Resistance-nodulation-division family
S	Substrate
SAR	Structure-activity relationship
S. aureus	*Staphylococcus aureus*
St. pneumoniae	*Streptococcus pneumoniae*
SDR	Short chain dehydrogenase reductase
SDS	Sodium dodecyl sulfate polyacrylamide gel electrophoresis
TCL	Triclosan
T_m	Midpoint temperatures of the protein-unfolding transition
t_R	Residence time
v_c	Uninhibited reaction velocity
v_i	Initial velocity
V_{max}	Maximum velocity
v_s	Steady-state velocity
wt	Wild type
X. oryzae	*Xanthomonas oryzae*
Y. pestis	*Yersinia pestis*
*Yp*FabV	ENR FabV from *Yersinia pestis*

Acknowledgments

I would like to express my sincere appreciation for my advisor, Professor Peter J. Tonge, for his continuous support and guidance throughout my doctoral studies. His enthusiasm, encouragement and knowledge greatly influenced my development as an independent scientist. I am tremendously appreciative of the freedom and support he provided me to explore my research interests, along with opportunities that match my career goals. I would also like to thank my co-advisor, Professor Jessica Seeliger, for her unwavering support. She challenged and diversified my research interests through literature discussions and meetings. I hope that both Professor Peter J. Tonge and Professor Jessica Seeliger will continue to be lifelong mentors.

I would like to thank the chairperson of my dissertation committee, Professor Isaac Carrico, for his insightful comments and suggestions that guided the progress of my research and future research interests. I am grateful for the selection of Professor Kathyln Parker as the third member of my dissertation committee. She was pleasant to work with as a rotation student. Her guidance, support, and advice throughout my doctoral studies were immensely appreciated. Also, I would like to thank Professor Miguel Garcia-Diaz for his advice and insights as the outside member of my committee. We engaged in interesting discussions about my research.

I would like to thank all the past and present members of the Tonge group. You stimulated interesting discussions, scientific debates, and offered genuine help. I will cherish the moments we shared in and outside the laboratory.

Last but not least, I would like to thank my wonderful parents and siblings for their guidance throughout my life. Your love and confidence encourages me to complete this work, and I am proud to be a member of the family.

List of Publications

- **Neckles, C**.; Hirschbeck, M.W.; Lai, C.; Davoodi, S.; Liu, N.; Pan P.; Shah S; Bommineni G.; Lai C; Simmerling, C.; Kisker, C.; and Tonge, P.J. (2014) "Mechanistic and Inhibition of the FabV Enoyl-ACP Reductase from *Yersinia pestis*". *Unpublished Manuscript.*

- **Neckles, C**.*; Yu, W.*; Bommineni, G.; Cummings, J.; Hirschbeck, M.W.; Daryaee, F.*; Zhang, Z.; Kim M.; Kisker, C.; Slayden, R.; and Tonge, P.J. (2014) "MUT056399 and *p*-Fluoro Diphenyl Ethers: Detailed Kinetic Analysis on the Slow Binding Inhibition of Enoyl-ACP Reductase FabI from *Burkholderia pseudomallei*". *In Preparation.*

- Yu, W.; Chang, A.; **Neckles, C.**; Liu, N.; Bommineni, G.; Pan, P.; Spagnuolo, L.; and Tonge, P.J. (2014) "A [^{32}P] Nicotinamide Adenine Dinucleotide Method to Identify and Quantitate Long Residence Time Enoyl- ACP Reductase Inhibitors". *Unpublished Manuscript.*

- Cummings, J.; Beaupre, A.; Knudson, S.; Liu, N.; Yu, W.; **Neckles, C**.; Wang, H.; Khanna, A.; Bommineni, G.; Trunck, L.; Schweizer, H.; Tonge, P.J.; Slayden, R. (2014) "Substituted Diphenyl Ethers as a Novel Chemotherapeutic Platform against *Burkholderia pseudomallei*". *Antimicrobial Agents and Chemotherapy* 58 (3), 1646-51.

- Hirschbeck, M.W.; Kuper, J.; Liu, N.; Lu, H., **Neckles, C**.; Shah, S.; Wagner, S.; Sotriffer, C.A.; Tonge, P.J.; Kisker, C. (2012) "Structure of the *Yersinia pestis* FabV enoyl-ACP reductase and its interaction with two novel 2-pyridone inhibitors". *Structure* 20 (1), 89–100.

* These authors contributed equally to this work

Chapter 1: Targeting the Fatty Acid Biosynthesis Type II Pathway

Antibiotics: Historical Perspective and Future Directions

In 1877, Pasteur and Joubert observed that co-infection of certain air-borne organisms with *Bacillus anthracis* inhibited the growth of *B. anthracis*. Since then investigators have found that a substance produced by one microbe may inhibit the growth of another microbe (*1*). During the late 1880s, Nobel Laureate Paul Ehrlich performed a large-scale screen of dyes against various organisms. Subsequently, in 1904, he discovered syphilis—an incurable endemic disease at that time—could be treated with arsphenamine (Salvarsan) (*2*). Ehrlich sparked the birth and foundation of the antibiotic revolution through his hypothesis of a "magic bullet" that has target selectivity to disease-causing microbes, rather than its host (*2, 3*). The "magic bullet" was later termed an antibiotic, which is a substance that inhibits growth or kills bacteria.

Most current synthetic and natural product-based antibiotics were first identified and characterized during the golden era of antibiotic discovery (1940-1960), and the discovery of new treatments has drastically declined since the early 1960s (*4*). More importantly, drug resistance emerged shortly after antibiotics were introduced into the market. Now there is an urgent need to develop novel agents that can combat worldwide antibacterial resistance mechanisms (*5-7*).

To combat drug resistance, one approach is to be 'one step ahead' of resistant microorganisms by incremental improvements of existing drugs (*8*). However, only a small subgroup out of the essential bacterial targets is inhibited by the existing classes of antibiotics (*9*). Hence, new strategies are needed to keep pace with microbial resistance. As a result of

extensive gene sequencing comparisons, genomic-based drug discovery is an alternative strategy to determine the next generation antibiotics (Figure 1.1). New targets can be identified based on gene essentiality and the conservation of genes across bacterial species that are not present in humans (*10*). Inhibitors of these targets can be identified by appropriate high-throughput screens and diverse compound libraries. Hit compounds from the library can then be further validated and optimized through structure-activity relationship (SAR) studies to develop lead candidates. Subsequently, lead candidates can be tested for safety and efficacy, and then investigated in animal infection models followed by human studies.

Unfortunately, there are several drawbacks to utilizing genomic-based drug discovery. First, bacterial species are diverse and genes that are essential in one pathogen may not be essential in another pathogen. Second, most antibiotic classes have emerged from old-school natural product screening, and synthetic compound libraries have been unable to produce suitable leads (*11*). Third, the introduction of new drugs into the clinic is a long and difficult process (*12*). These concerns induced a transition within the pharmaceutical industry from novel targets to good targets (*13*). Therefore, academic settings have been obliged to discover and validate novel drug targets, which can then be followed up by the pharmaceutical industry as good targets.
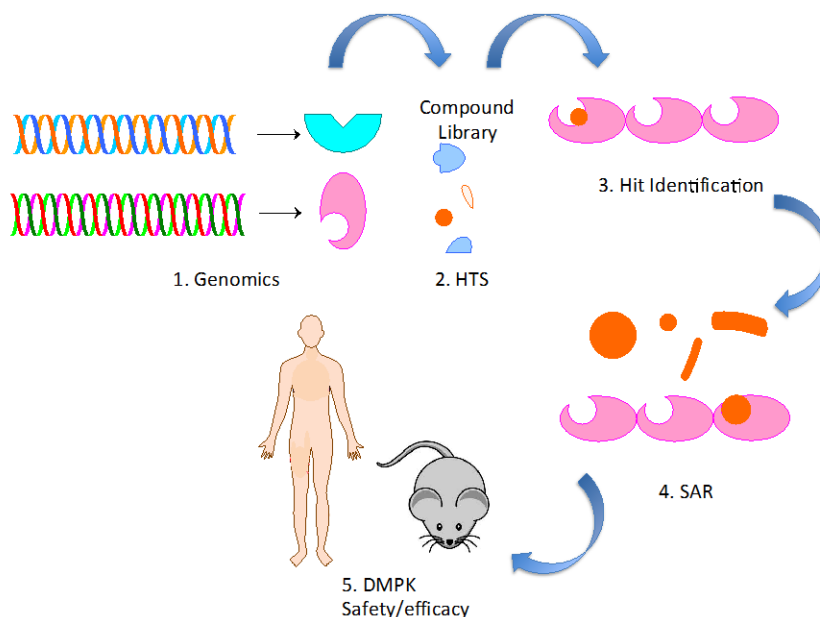
Figure 1.1 Stages of genomic-based drug discovery approach adapted from McDevitt *et al* (*8*).
Abbreviations: HTS, high-throughput screening; SAR, structure-activity relationships; DMPK, drug metabolism and pharmacokinetics.

Fatty Acid Biosynthesis Type II (FAS-II) Pathway

The fatty acid synthase (FAS) is responsible for the synthesis of essential fatty acid precursors for the phospholipid bilayer of the cell membrane. Mammals utilize the type 1 (FAS-I) system in which a single, large polypeptide is composed of distinct enzymatic domains. Bacteria, plants, and protozoans on the contrary utilize the type II (FAS-II) system in which the FAS components are discrete proteins (*14-17*). In spite of the fact that the enzyme homologues found in FAS-I and FAS-II systems are related in structure and function, these enzymes lack overall sequence homology (*18*). These fundamental differences between the two FAS systems, including protein sequence and FAS component composition, allow the enzymes in the FAS-II from bacteria to be potentially good drug targets. Enzymes within the bacterial FAS-II pathway were shown to be a source for novel antimicrobial targets through genomics, bioinformatics,

functional assays, and structural analyses (*18*). Moreover, the essentiality of most FAS-II enzymes for bacterial viability suggests that the FAS-II pathway is a source of novel antibacterial targets (*19*).

The FAS-II pathway in *Escherichia coli* has been the most studied. Additionally, almost all of the *E. coli* FAS-II enzyme homologues are well conserved among all bacteria. Therefore, the *E. coli* FAS-II pathway serves as a mechanistic model to understand each step of the FAS-II pathway (Figure 1.2) (*20*). FAS-II is comprised of two key stages: initiation and elongation. During the initiation process, a heterotetrameric enzyme acetyl-CoA carboxylase (AccABCD), which is encoded by four genes accA, accB, accC, and accD, catalyzes the biotin-dependent carboxylation of acetyl-CoA to malonyl-CoA (*21*). The malonyl moiety from the product malonyl-CoA is then transferred to the terminal sulfhydryl of acyl carrier protein (ACP) to produce malonyl-ACP. This reaction occurs through a transthioesterification that is catalyzed by malonyl-CoA:ACP transacylase (FabD) (*22*). ACP then shuttles the acyl chain to all the enzymes in the subsequent elongation steps (*23*).

The first step of the elongation cycle is catalyzed by the β-ketoacyl-ACP synthase III (FabH) via a condensation reaction between acetyl-CoA and malonyl-ACP to yield β-ketoacyl-ACP (*24*). The product β-ketoacyl-ACP is then reduced at the C3 position to produce β-hydroxylacyl-ACP by the β-ketoacyl-ACP reductase FabG (*25*). The next step in the elongation cycle is catalyzed by β-hydroxylacyl-ACP dehydratase FabZ or FabA, in which β-hydroxylacyl-ACP undergoes dehydration to form *trans*-2-enoyl-ACP (*26, 27*). Finally, the enoyl-ACP reductase (ENR) FabI reduces the C2 and C3 carbon-carbon double bond to a single bond to produce saturated acyl-ACP. The elongation cycle repeats until the specific chain length is reached and subsequently a thioesterase cleaves the fatty acids for further cell wall synthesis.
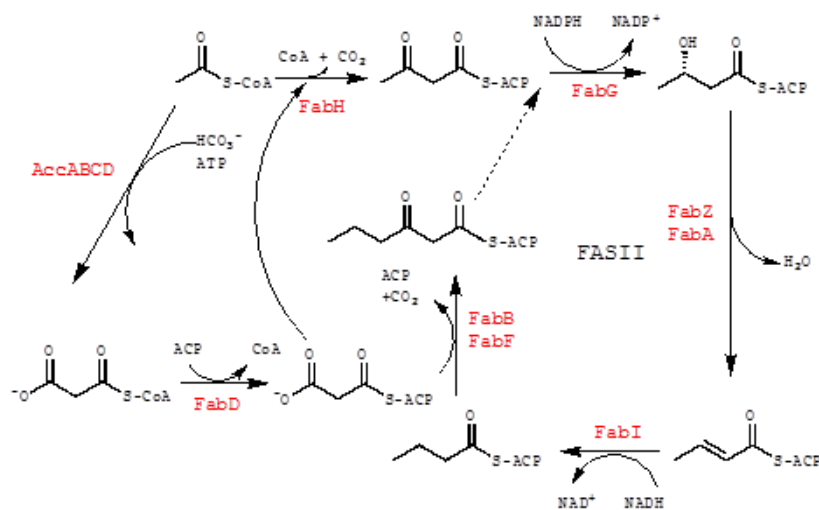
Figure 1.2 Fatty acid synthesis in *E. coli* adapted from Heath *et al* (*20*).
AccABCD is the acetyl-CoA carboxylase; FabH is the malonyl-CoA:ACP transacylase; FabG is the β-ketoacyl-ACP reductase; FabA and FabZ are the β-hydroxylacyl-ACP dehydratases; FabI is the enoyl-ACP reductase; FabH, FabB, and FabF are the β-ketoacyl-ACP synthases. FabH catalyzes initial condensation reaction, while FabB or FabF initiates further rounds of elongation.
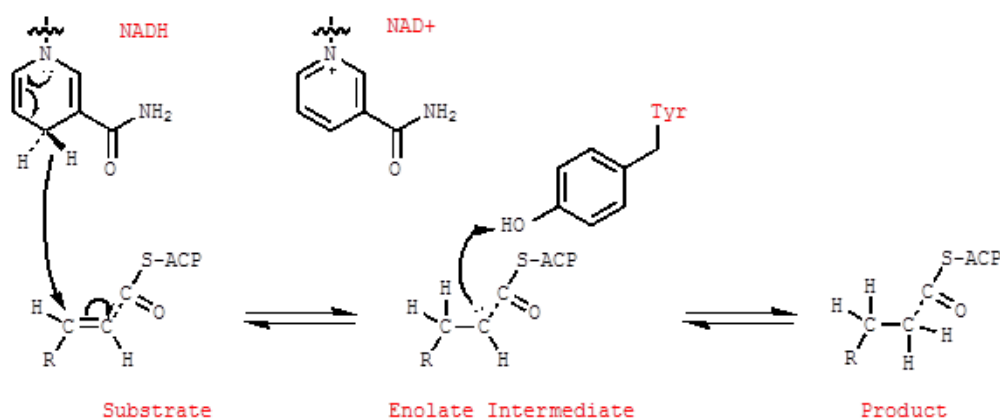
Figure 1.3 Reduction reaction of *E. coli* enoyl-ACP reductase adapted from Massengo-Tiassé *et al* (*28*).

Enoyl-ACP Reductase (ENR)

The ENR catalyzes the reduction of a *trans*-2-enoyl-ACP to a saturated acyl-ACP, in which the reductant is either NADH or NADPH, and in one case a reduced flavin $FMNH_2$ is used as an intermediate by the reductase (*28*). The reduction of the double bond with the pyridine nucleotide proceeds via the formation of an enzyme-stabilized enolate intermediate that subsequently collapses through protonation at C2 (*29, 30*). The conjugate addition of a hydride ion from NAD(P)H to C3 of the *trans*-2-enoyl-ACP is summarized in Figure 1.3. This bacterial FabI ENR utilizes the 4*S* hydrogen as the pyridine nucleotide cofactor hydride ion, whereas the mammalian FAS-I pathway utilizes the 4*R* hydrogen (*31*). The physiological substrates of ENRs are *trans*-2-enoyl-ACPs. However, these enzymes have shown activity with model substrates, specifically *trans*-2-enoyl-CoA and -N-acetylcysteamine. Enzyme specificity with these model substrates generally has higher K_M values and lower V_{max} values in comparison to its natural substrates (*28*).

The ENR was relatively neglected compared to other enzymes within the field of fatty acid biosynthesis until the ENR from *Mycobacterium tuberculosis* (InhA) was identified as the target of isoniazid, an anti-tuberculosis drug (*32*). Successively, investigators found that *E. coli* FabI and other ENR's from bacteria were targets of broad-spectrum antimicrobial triclosan, and that ENR was a good drug target candidate (*33*). Nonetheless, some bacteria were resistant to triclosan, which suggested the presence of triclosan-resistant ENRs. Interest in triclosan resistance inherently expanded the ENR literature, which led to the discovery of four different classes of ENRs within the FAS-II pathway (*28, 34*).

ENR Diversity

In contrast to most enzymes in the FAS-II pathway, the ENR has an unusual diversity with at least four known classes: FabI, FabK, FabL, and FabV. The FabI, FabL, and FabV ENR classes belong to the short chain dehydrogenase reductase (SDR) superfamily, in which they have a conserved SDR-fold for coenzyme-binding and definitive active site regions (*28*). FabI and FabL have a highly conserved active site motif, Tyr-X_6-Lys, while FabV active site motif is slightly larger, Tyr-X_8-Lys (*35, 36*).

FabK is a flavin-dependent oxidoreductase that is a TIM barrel flavin-containing enzyme, like the ENRs found in mitochondria and the ENR domains of mammalian and fungal megasynthases (*28*). For instance, *Streptococcus pneumoniae* FabK utilize NADH as the reductant, in which FabK reduces the tightly bound flavin cofactor FMN and employs $FMNH_2$ as an intermediate for the reductase.

Gene comparison of ENR classes found in biodefense and clinically relevant pathogens show that FabI and FabV are the most prevalent. One or both classes are present in many of pathogens that are of interest (Table 1.1). Interestingly, Gram-positive and Gram-negative bacterial model systems may express FabI. However, there is precedent for Gram-positive pathogens to also express FabL or FabK. For example, in addition to the expression of FabI, *Bacillus subtilis* expresses FabL and *St. pneumoniae* expresses FabK *(37, 38).* The biological reasons for bacterial species to express diverse ENR classes or combinations thereof are currently unknown.

Table 1.1 Comparison of enoyl-ACP in different bacterial species.

	Enoyl-ACP Reductase Class				Reference
	FabI	FabV	FabK	FabL	
Biodefense Pathogens					
Bacillus anthracis	X				*(39)*
Burkholderia mallei	X	X			*(40)*
Burkholderia pseudomallei	X	X			*(40)*
Coxiella burnetii		X			ZP_01947648
Francisella tularensis	X				*(41)*
Yersinia pestis		X			*(40, 42)*
Clinically Relevant Pathogens					
Acinetobacter baumannii	X				YP_001715024
Enterococcus faecium	X		X		WP_024635157 EPI26117
Enterobacter spp.	X	X			YP_006578944 ESL68295
Klebsiella pneumoniae	X				YP_001334947
Mycobacterium tuberculosis	X				*(30)*
Pseudomonas aeruginosa	X	X			*(43)*
Staphylococcus aureus	X				*(44)*
Streptococcus pneumoniae	X		X		*(37)*
Vibrio cholerae		X			*(36)*
Model Systems					
Bacillus subtilis	X			X	*(38)*
Escherichia coli	X				*(31)*
Mycobacterium smegmatis	X				*(45)*

ENR Inhibition

The ENR FabI has been the most extensively studied as a potential drug target among the enzymes in the FAS-II pathway (*46*). FabI is highly conserved among most pathogenic bacteria, and *E. coli* FabI has been shown to be essential for bacterial viability (*47, 48*). Also, several natural products and synthetic compounds have been shown to inhibit FabI homologues.

Microbial natural products can provide chemical entities for novel chemotherapeutics with low toxicity. For instance, studies revealed antibacterial effects of various natural products

that target FabI (Figure 1.4). Screening of antibacterial natural products led to hit compounds, such as aquastatin A (*49*), chalcomoracin (*50*), curcumin (*51*), luteolin (*51*), methyl-branched fatty acids (*52*), verrulactone A (*53*), and vinaxanthone (*54*). Likewise, some naturally occurring inhibitors of fungal origin have been shown to specifically target FabK (atromentin and leucomelone) and FabI (cephalochromin and cyperin) (*28, 55-57*).

Furthermore, many synthetic compounds inhibit FabI homologues in complex with the oxidized (NAD^+) or reduced (NAD(P)H) cofactor, such as diazaborines, isoniazid (INH), triclosan, 2-pyridones and 4-pyridones (Figure 1.5). Diazaborines (**2**, Figure 1.5) are bisubstrate inhibitors since they resemble the binding model of the enoyl-ACP and cofactor. These compounds are heterocyclic boron-containing compounds that form a dative bond between the 2'-hydroxyl of the nicotinamide ribose of NAD^+ and the boron atom of the inhibitor (*58*). Several derivatives of diazaborines exhibit antibacterial activity against *E. coli*, *Salmonella enterica*, *M. tuberculosis* and *Klebsiella pneumoniae* (**3-4**, Figure 1.5) (*59-61*). Another example of a bisubstrate inhibitor is INH (**1**, Figure 1.5). INH is a pro-drug that is activated by KatG, the mycobacterial catalase-peroxidase (*32*). It forms an inhibitor adduct with NAD^+ (INH-NAD^+), and it is a potent inhibitor of *M. tuberculosis* ENR InhA (*62, 63*).

The broad-spectrum antibacterial triclosan is a noncovalent inhibitor that interacts with the enzyme-cofactor binary complex. Inhibitor optimization on both of the inhibitor rings (**5**, Figure 1.5) have been attempted in order to improve binding affinity along with antibacterial activity (*33, 64-68*). Unfortunately, these potent diphenyl ethers have modest *in vivo* efficacy since they are lipophilic and are liable to Phase II metabolism due to *O*-glucuronidation at the phenolic hydroxyl (*69*). Alternative compounds are 2-pyridones and 4-pyridones because they replace the phenolic hydroxyl. These compounds have lower ClogP values and increased

9

metabolic stability (**6-7**, Figure 1.5) (*70-72*). Phenylimidazole derivatives of 4-pyridones are dual inhibitors of both FabI and FabK classes (*73*). Also, the 2-pyridone inhibitor CG400549 was shown to target *S. aureus* FabI, and it is currently in Phase II clinical trials (*72*).

Sensitivity to inhibitors is diverse among the ENR classes. For example, triclosan is a potent nanomolar inhibitor of the FabI class, while a poor inhibitor of FabL (*38*). FabK is not inhibited by triclosan, and triclosan is a micromolar inhibitor of the *Burkholderia mallei* FabV (*37, 40*). Additionally, there is limited ENR literature on inhibitors against the FabV homologues. The newly discovered FabV class is of interest, along with FabI class, since the FabV gene is found in some biodefense and clinically relevant pathogens and inhibitory activity of this class is lacking (Table 1.1).
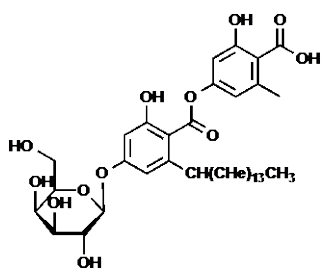
Aquastatin A
S. aureus FabI
$IC_{50}=3.2$ μM/MIC= 32 μg/mL (*49*)
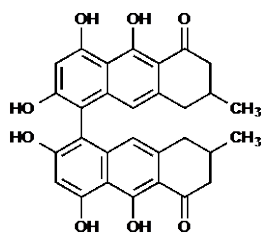
Cephalochromin
S. aureus FabI
$IC_{50}=1.9$ μM/MIC= 8 μg/mL (*56*)
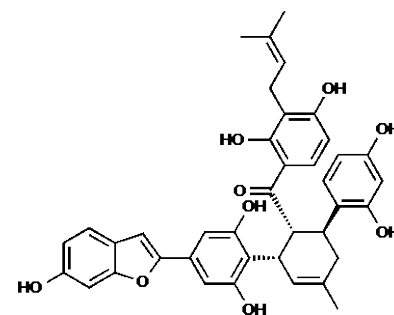
Chalcomoracin
S. aureus FabI
$IC_{50}=5.5$ μM/MIC= 4 μg/mL (*50*)
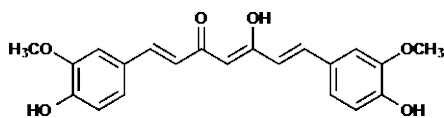
Curcumin
E. coli FabI
$K_i=15$ μM/MIC= 74 μg/mL (*51*)
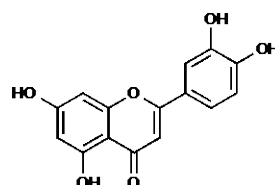
Luteolin
E. coli FabI
$K_i=7.1$ μM/MIC= 74 μg/mL (*51*)
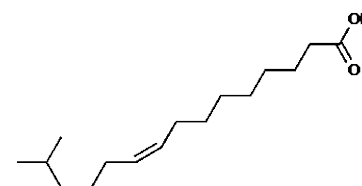
Methyl-branched fatty acids
S. aureus FabI
$IC_{50}=16$ μM/MIC= 32 μg/mL (*52*)
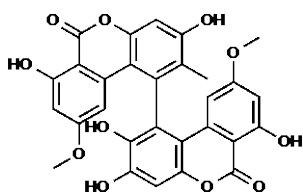
Verrulactone A
S. aureus FabI
$IC_{50}=0.92$ μM/MIC= 8-16 μg/mL (*53*)
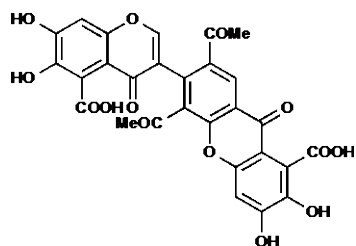
Vinaxanthone
S. aureus FabI
$IC_{50}=0.5$ μM/MIC= 32 μg/mL (*54*)
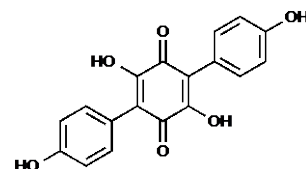
Atromentin
St. pneumoniae FabK
$IC_{50}=0.24$ μM/MIC= N/A (*55*)
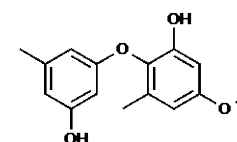
Cyperin
A. thaliana FabI
$K_i=14$ μM; MIC= N/A(*57*)

Figure 1.4 Natural product inhibitors of FabI.

11
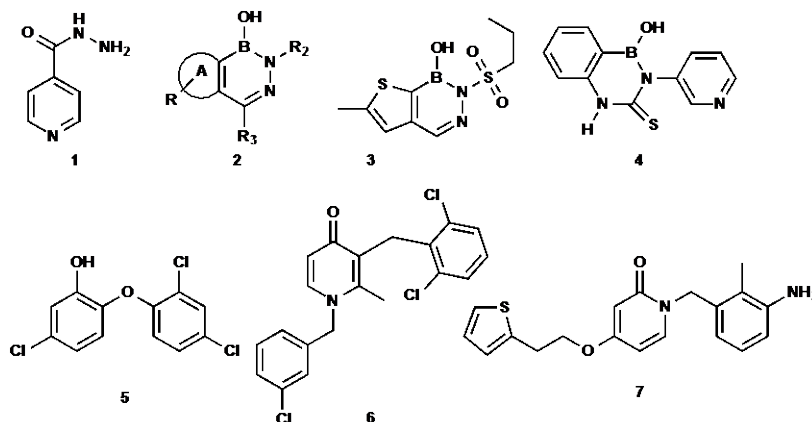
Figure 1.5 Examples of enoyl-ACP reductase inhibitors.
Covalent inhibitors include isoniazid **1** and diazaborines **2,** such as thiodiazaborine **3** and benzodiazaborine **4**. Noncovalent inhibitors include triclosan **5**, 4-pyridone derivatives resembling compound **6** (*70*), and 2-pyridone derivatives like CG400549 in phase II clinical trial.

Research Project Overview

This project focuses on the mechanism and inhibition of the ENRs from different biodefense and emerging opportunistic pathogens. ENRs are responsible for the last elongation step in fatty acid synthesis, which involves the reduction of the double bond of *trans*-2-enoyl-ACP. Currently, there are four known classes of ENRs (FabI, FabL, FabK, and FabV), and their specificity and selectivity to inhibitors must be understood before we can develop ENR inhibitors with broad-spectrum antibacterial activity.

In particular, comparison of FabI and FabV is important since one or both are present in many pathogens that are of interest. In Chapter 2, detailed mechanistic analyses are described for substrate recognition of the sole ENR FabV found in *Yersinia pestis (Yp*FabV*)*. In Chapter 3, we explore the effect between an altered substrate binding mechanism for *Yp*FabV and its mutants. Also, we investigate the mode of inhibition for diphenyl ether-, 2-pyridone-, and 4-pyridone-based scaffolds that target *Yp*FabV and T276S *Yp*FabV, and we compare the mode of inhibition to *B. pseudomallei* ENRs, FabI and FabV.

We extend our inhibition studies to slow-onset diphenyl ether inhibitors of the *B. pseudomallei* FabI in Chapter 4. In turn, we were able to use rational inhibitor design to translate the slow-onset inhibition mechanism from FabI to FabV. In Chapter 5, steady-state kinetic analysis of the P142W *Yp*FabV mutant revealed a gain of slow-onset inhibition for an inhibitor (**PT156**) that displays rapid-reversible binding kinetics for the wild-type enzyme.

Chapter 2: Mechanistic Analysis of the Enoyl-ACP Reductase FabV from *Yersinia pestis*

Background

Yersinia pestis

Plague is an infectious, zoonotic disease that has affected the human population during historical epidemics such as the Plague of Justinian (542), the Black Death (1347-1353), and the Third Pandemic (1855) (*74*). The causative agent of plague is a Gram-negative bacterium called *Yersinia pestis (Y. pestis).* It was independently identified by Alexandre Yersin and Shibasaburo Kitasato during the Hong Kong epidemic in 1894 (*75*). Plague is transmitted from infected rodents to humans through fleas, ticks, and body lice. For example, fleas can retain *Y. pestis* within its stomach through an antibacterial mechanism, and the flea can then regurgitate the bacteria into the mammalian blood during the feeding process (*74, 76*). Yersin was the first to note the relationship between rodents and plague, and Paul Simon introduced the role of the rat flea in the transmission of plague (*75*).

Once *Y. pestis* is transmitted, there are three primary forms of plague that can be observed—bubonic (infection of the lymph nodes), pneumonic (infection of the lungs), and septicemic (infection of the blood). While bubonic and septicemic plague are the predominant cases, pneumonic plague is the most hazardous form because it can be transmitted by aerosolic propagation through the coughing and sneezing of infected humans (*74*). Additionally, if left

14

untreated, bubonic plague has a 40% to 60% fatality rate, while septicemic and pneumonic cases have a 100% mortality rate (*77*).

Since the 14th century second plague pandemic, *Y. pestis* was deliberately used as a biological weapon (*78*). During the siege of Caffa, the Tartar force hurled cadavers infected with *Y. pestis* into the city of Genoese (now Feodosiya, Ukraine), which forced the Genoese forces to retreat after an outbreak of plague (*79, 80*). Additional use of *Y. pestis* as a weapon continued for the next centuries. For instance, the Japanese army, Unit 731, experimented on *Y. pestis* and dropped plague-infected fleas over populated areas in China and Manchuria during World War II (*78, 79*).

After World War II, the USA, the former Soviet Union, and several other countries performed research on *Y. pestis* as biological weapon. The former Soviet Union focused on the elimination of transmission vectors in order to release an aerosolized form of *Y. pestis*, which includes the elimination of the flea dependent vector (*78*). Unfortunately, Soviet scientists were even able to produce large quantities of *Y. pestis* for biological weapons (*81*). After September 11, 2001, the attacks on the USA World Trade Center ignited the reemergence of the threat of bioterrorism. *Y. pestis* is now classified as a Tier 1 Biological Select Agent or Toxin (BSAT) by the Centers for Disease Control and Prevention (CDC) because deliberate dissemination of *Y. pestis* can result in high mortality rates (*82*).

Treatment of Plague and Y. pestis Antibiotic Resistant Strains

Historically, streptomycin has been used to treat plague and it still remains the preferred treatment (*83*). Although streptomycin is the only antibiotic approved by the Food and Drug Administration (FDA) to treat plague, the supply of streptomycin is limited in the USA. Therefore, many experts suggest gentamicin as an alternative treatment (*78*). The routes of administration for both drugs are by intramuscular or intravenous injection, which may decrease patient compliance. Thus, oral antibiotics that are not FDA-approved for treatment of plague are recommended, including tetracycline, doxycycline, chloramphenicol, and fluoroquinolones (*84*).

A plague isolate was found in Madagascar in 1995 that contained a multidrug-resistant transferable plasmid. This organism produced TEM-1 β-lactamase, chloramphenicol acetyltransferase, and a streptomycin-modifying enzyme (*85*). Within the same year, a second *Y. pestis* strain was identified to exhibit a high-level of streptomycin resistance. This strain contained a plasmid that encoded the streptomycin-modifying phosphotransferase gene (*86*). More importantly, plasmids in both drug-resistant strain isolates were shown to be transferred to other *Y. pestis* strains and *E. coli*, and this exchange of genetic material can occur with other bacterial species within the same Enterobacteriaceae family (*85, 86*).

While *Y. pestis* natural resistance to antibiotics is rare, there is an increase in concern for the engagement of natural or bioengineered drug-resistant strains in bioterrorism attacks. Former Soviet Union bioweapons operations have been reported to engineer multidrug-resistant and

fluoroquinolone-resistant *Y. pestis* strains, which support the need for future development of

novel chemotherapeutics to treat plague (*81, 84*).

Acyl-carrier-protein (ACP)   Coenzyme A
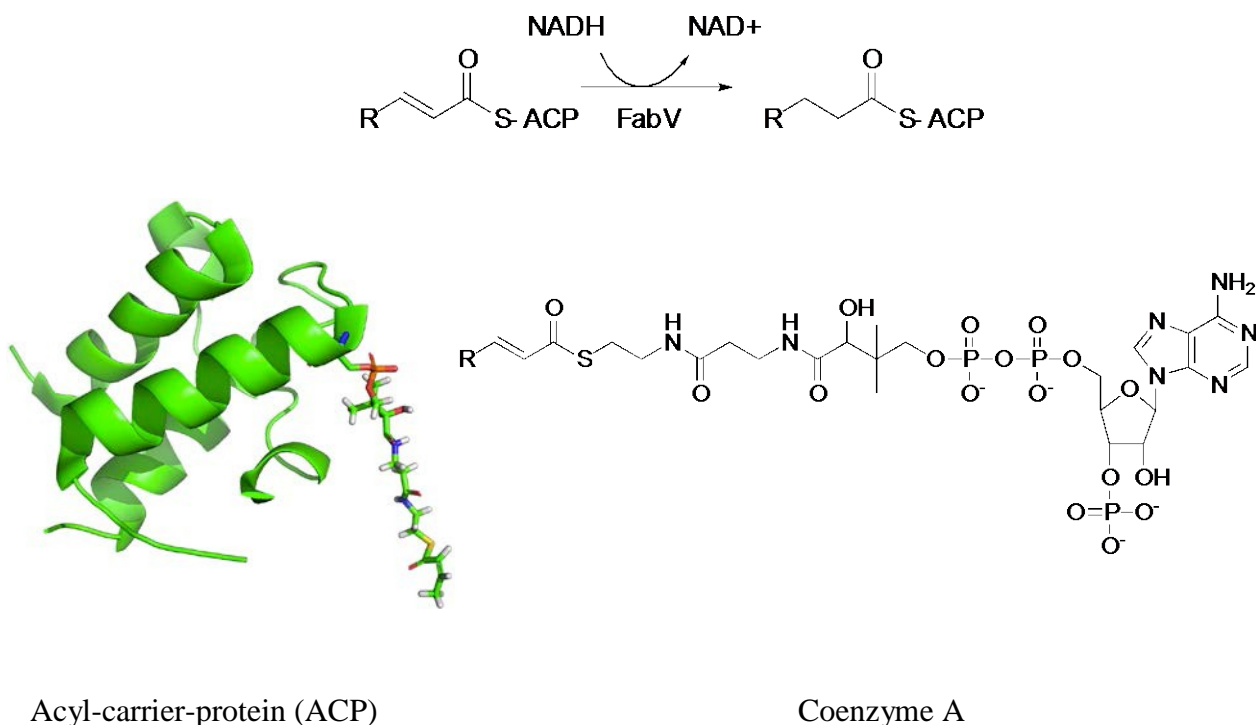
Scheme 2.1 Mechanism of the enoyl-ACP reductase.
Trans-2-enoyl-ACP (modified PDB 1T8K) is the natural substrate for the enoyl-ACP reductase.
This enzyme is also active with model substrates (*trans*-2-enoyl-coenyzme A).

The FAS-II pathway and the Fourth Enoyl-ACP Reductase (FabV)

The fatty acid biosynthesis type II (FAS-II) pathway is responsible for the synthesis of

fatty acid precursors that are needed to build the bacterial cell membrane, and most of the FAS-II

enzymes are essential for bacterial viability (*19*). In bacteria, distinct enzymes catalyze each step

of this pathway, which differs fundamentally from the mammalian FAS-I system where catalysis occurs via a multi-domain enzyme complex. One important enzyme within the FAS-II pathway is the enoyl-ACP reductase (ENR), which catalyzes the last reaction in the elongation cycle and it reduces a double bond to a single bond upon the oxidation of NADH to NAD^+ (Scheme 2.1).

The first ENR to be identified was FabI from *E. coli* (*87*), which was initially considered to be the only ENR in bacteria. FabI has been extensively analyzed on the basis of antibacterial compounds that target this enzyme (*65, 88*). However, other ENR classes were discovered because some pathogens lacked FabI homologues, and other pathogens were resistant to antibiotics that were meant to inhibit FabI. A flavin-dependent ENR FabK was discovered in *Streptococcus pneumoniae (37),* and an ENR that belongs to the short-chain dehydrogenase/reductase (SDR) superfamily, FabL, was isolated from *Bacillus subtilis (38).* Another ENR that belongs to the SDR superfamily, FabV, was discovered in *Vibrio cholera (36), Pseudomonas aeruginosa (43),* and *Burkholderia mallei (40).* Interestingly, certain bacteria may express more than one ENR. FabI and FabL coexist in *B. subtilis (38),* and FabI and FabV are present in *P. aeruginosa (43)* and *B. mallei (40).* The biological reasons why some bacteria express different ENR classes or combinations thereof are currently unknown.

Previously, we characterized FabV from *B. mallei* and showed that *Bm*FabV catalyzes substrate reduction through an ordered bi-bi mechanism, in which NADH binds first to the enzyme, and after catalysis NAD^+ dissociates last *(40).* However, this pathogen contains both FabI and FabV ENRs, and mechanistic insights into substrate recognition are lacking in

pathogens that solely express the FabV. Thus, we extended our mechanistic studies to the FabV ENR from *Y. pestis* (*Yp*FabV).

Project Goal

To gain further mechanistic insights into substrate recognition of the ENR FabV, we extended our studies to the Gram-negative biological warfare agent *Y. pestis*, which expresses only FabV. The projected outcome of this proposed work is to reveal the substrate binding mechanism of *Yp*FabV through steady-state kinetic analysis and direct binding experiments. In addition, we would like to evaluate the role of key amino acid residues that are essential for enzymatic activity via site-directed mutagenesis. We are particularly interested in the role of T276 that is found on the N-terminal end of the helical substrate binding loop.

Materials and Methods

Materials.

His-bind Ni^{2+}-NTA resin was purchased from Invitrogen. *trans*-2-Dodecenoic acid, *trans*-2-decenoic acid, and *trans*-2-octenoic acid were purchased from TCI. Lauroyl coenzyme A was purchased from Sigma-Aldrich. Luria broth was obtained from VWR. All other chemical reagents were purchased from Fisher.

19

Synthesis of trans-2-dodecenoyl-CoA (ddCoA), trans-2-decenoyl-CoA (decCoA), and trans-2-octenoyl-CoA (octCoA).

ddCoA, decCoA, and octCoA were synthesized from *trans*-2-dodecenoic acid, *trans*-2-decenoic acid, and *trans*-2-octenoic acid, respectively, using the mixed anhydride method as previously described (*89*). Product formation was confirmed by ESI mass spectrometry.

Cloning, expression, and purification of YpFabV.

The *fabV* gene was amplified from *Y. pestis* A1122 and CO92 (T276S variant) strains using the polymerase chain reaction (PCR) with the primers listed in Table 2.1. The amplified PCR product was digested with XhoI and EcoRI and inserted into the pET15b vector (Novagen), such that it contained an N-terminal hexa-histidine tag. The sequence of the gene was confirmed by DNA sequencing (DNA Sequencing Facility, Health Science Center, Stony Brook University).

Protein expression and purification were performed as previously described using *E. coli* BL21(DE3) pLysS cells (*42*). The concentration of FabV was spectrophotometrically determined at 280 nm and by using an extinction coefficient of 48,360 M^{-1} cm^{-1} calculated from the primary sequence of the protein (ExPASy ProtParam tool).

Site-directed mutagenesis, expression, and purification of YpFabV mutants.

The *Yp*FabV mutants T276A, T276G, T276V, T276C, and T276Y were prepared using the primers listed in Table 2.1 and the forward and reverse primers for wild-type *Yp*FabV. The amplified PCR product that consisted of the mutated FabV gene was digested with XhoI and EcoRI and inserted into the pET15b vector (Novagen), like the wild-type enzyme. The sequence of each mutant plasmid was confirmed by DNA sequencing. All mutants were expressed and purified using the same procedure described above for the wild-type enzyme.

Cloning, expression, and purification of BpFabV.

The *fabV* gene was amplified by PCR using the *B. pseudomallei* strain Bp82 with the primers listed in Table 2.1. The PCR amplified products were treated with NdeI and BamHI and inserted into the pET15b vector (Novagen), such that a hexa-histidine tag was encoded at the N-terminus. The constructs were transformed, purified and sequenced as described above. Protein expression and purification were performed as described previously using *E. coli* BL21(DE3) pLysS cells *(40)*. The concentration was spectrophotometrically determined at 280 nm and by using an extinction coefficient of 43,890 $M^{-1}cm^{-1}$.

Table 2.1 Designed primers for cloning and mutagenesis.

Name	Primers[a]
*Yp*FabV Forward	5'CCG<u>CTCGAG</u>ATGATTATAAAACCACGTGATA3'
*Yp*FabV Reverse	5'CCG<u>GAATTC</u>TTAACCCTGAATCAAGTTAGG3'
*ec*ACP Forward	5' CCG<u>CTCGAG</u>ATGAGCACTATCGAAGAACGCGTT 3'
*ec*ACP Reverse	5' CCG<u>GAATTC</u>TTACGCCTGGTGGCCGTTGATGTA 3'
*Bp*FabV Forward	5' GGAATTC<u>CATATG</u>ATCATCAAACCGCGCGTACGC 3'
*Bp*FabV Reverse	5' CGC<u>GGATCC</u>TCATTCGATCAGATTCGGAATCCG 3'
T276A *Yp*FabV Forward	5'GTATTAAAAGCAGTCGTG<u>GCC</u>CAAGCCAGCTCTGCC3'
T276A *Yp*FabV Reverse	5'GGCAGAGCTGGCTTG<u>GGC</u>CACGACTGCTTTTAATAC3'
T276C *Yp*FabV Forward	5'GTATTAAAAGCAGTCGTG<u>TGC</u>CAAGCCAGCTCTGCC3'
T276C *Yp*FabV Reverse	5'GGCAGAGCTGGCTTGG<u>CA</u>CACGACTGCTTTTAATAC3'
T276Y *Yp*FabV Forward	5'GTATTAAAAGCAGTCGTG<u>TAC</u>CAAGCCAGCTCTGCC3'
T276Y *Yp*FabV Reverse	5'GGCAGAGCTGGCTTG<u>GTA</u>CACGACTGCTTTTAATAC3'
T276V *Yp*FabV Forward	5'GTATTAAAAGCAGTCGTG<u>GTC</u>CAAGCCAGCTCTGCC3'
T276V *Yp*FabV Reverse	5'GGCAGAGCTGGCTTG<u>GAC</u>CACGACTGCTTTTAATAC3'

[a] Restriction and mutation sites are underlined

Cloning, expression, and purification of E. coli ACP.

The acyl carrier protein (ACP) from *E. coli* was amplified by PCR using the primers listed in Table 2.1. The PCR amplified product was treated with EcoRI and XhoI and ligated into the pET23b vector (Novagen) to encode a hexa-histidine tag at the C-terminus of the protein. The construct was transformed, purified, and sequenced as described above. Expression and purification of *ec*ACP were performed as previously described using *E. coli* BL21(DE3) pLysS cells (*44*). The concentration of the protein was spectrophotometrically determined at 280 nm and by using an extinction coefficient of 1490 M^{-1} cm^{-1}.

Enzymatic preparation of trans-2-octenoyl-ecACP and trans-2-dodecenoyl-ecACP.

Apo-*ec*ACP was converted to the *trans*-2-enoyl-*ec*ACP using the phosphopantetheinyl transferase from *Bacillus subtilis* Sfp (*44*). In a 1.5 mL reaction volume, 100 μM apo-*ec*ACP was incubated for 1 h at 37 °C with 200 μM octCoA and 1 μM Sfp in a buffer solution containing 75 mM Tris HCl, and 10 mM $MgCl_2$ at pH 7.5. The reaction was loaded onto an anion exchange column, MonoQ 5/50, and eluted with a gradient from buffer A (20mM Tris HCl at pH 7.0) to buffer B (20 mM Tris HCl and 800 mM NaCl at pH 7.0). Fractions were analyzed by a conformationally sensitive SDS-PAGE, and those that contained *trans*-2-octenoyl-*ec*ACP (oct-*ec*ACP) or *trans*-2-dodecenoyl-ecACP (C12-ecACP) were pooled and exchanged into 20 mM Tris-HCl, pH 7.5. The purified acylated protein was analyzed by MALDI-TOF mass spectrometry.

Direct binding experiments.

A titration fluorescence assay was used to determine the dissociation constant, K_d, of the substrate. Tryptophan fluorescence intensity changed based upon a change of the microenvironment as the substrate concentration was increased. In the binding experiments, the substrate was titrated to a buffer solution containing 0.5 μM enzyme, 30 mM PIPES, 150 mM NaCl and 1.0 mM EDTA (pH 8.0) at 25°C. Titrations were monitored using a Quanta Master fluorometer (Photon Technology International) at the excitation and emission wavelengths of

280 and 332 nm with slit widths of 4.0 and 2.0 mm, respectively. The K_d values were calculated using a Scatchard equation (*90*) from the software GraFit (Equation 2.1).

$$y = \frac{[L] \times Cap}{K_d + [L]}$$

Equation 2.1

y is the amount of ligand bound per the amount of receptor; *Cap* is the capacity for the binding ligand; [*L*] is the concentration of the free ligand, and K_d is the dissociation constant of the ligand from the receptor.

Steady-state kinetic analysis

Steady-state kinetics were performed on a Cary 100 Bio (Varian) spectrophotometer at 25 °C in a buffer solution containing 30 mM PIPES, 150 mM NaCl and 1.0 mM EDTA at pH 6.8, as previously reported (*42*). The initial velocities were measured by monitoring the oxidation of NADH to NAD^+ at 340 nm ($\varepsilon = 6{,}220\ M^{-1}\ cm^{-1}$).

$$v_o = \frac{v_{max}[S]}{K_M + [S]}$$

Equation 2.2

Substrate specificity was analyzed using the Michaelis-Menten equation (Equation 2.2) by measuring initial velocities at varying concentrations of CoA-based substrates and a fixed concentration of 250 μM NADH; in which, v_{max} is the maximum velocity, [*S*] is the substrate concentration, and K_M is the Michaelis-Menten constant for the substrate. The substrate binding mechanism was analyzed by measuring initial velocities at varying concentrations of one substrate, while keeping the other substrate concentration fixed at subsaturating or saturating concentrations.

The product inhibition mechanisms were analyzed using Lineweaver-Burk plots by measuring the initial velocities at a fixed concentration of 250 µM NADH and at varying concentrations of ddCoA and inhibitor. Inhibition constants for competitive, uncompetitive, and noncompetitive inhibitors were analyzed using Equations 2.3-2.5.

$$v_o = \frac{v_{max}[S]}{K_M\left(1 + \frac{[I]}{K_i}\right) + [S]}$$

Equation 2.3

$$v_o = \frac{v_{max}[S]}{K_M + [S]\left(1 + \frac{[I]}{K_i'}\right)}$$

Equation 2.4

$$v_o = \frac{v_{max}[S]}{K_M\left(1 + \frac{[I]}{K_i}\right) + [S]\left(1 + \frac{[I]}{K_i'}\right)}$$

Equation 2.5

[S] is the substrate concentration, [I] is the concentration of inhibitor added, K_M is the Michaelis-Menten constant for the substrate, v_{max} is the maximum velocity, and K_i and K'_i are inhibition constants.

Results

YpFabV has remote substrate binding interactions with trans-2-enoyl-ACP

The structure of T276S *Y. pestis* FabV in complex with NADH was solved by Hirschbeck *et al* (*42*), along with complexes bound to 2-pyridone inhibitors. Structural studies showed the admission of the inhibitor into the major portal of active site was coupled with the opening of the substrate binding loop, which may resemble the coupling interaction between FabV and its ACP substrate. Although these key structural insights provided a glimpse into substrate recognition, there is currently little mechanistic information provided on substrate binding for wild-type *Yp*FabV. Thus, kinetic analysis of substrate reduction catalyzed by *Yp*FabV was monitored using *trans*-2-octenoyl-*E. coli* ACP (oct-*ec*ACP) and *trans*-2-octenoyl-coenzyme A (octCoA) (Scheme 2.1). Apo-*ec*ACP shares 90% sequence identity with the putative ACP from *Y. pestis*. Therefore, we assumed that the ACP from *E. coli* would serve as a suitable substrate for *Yp*FabV. Apo-*ec*ACP was enzymatically modified to oct-*ec*ACP by *B. subtilis* phosphopantetheinyl transferase. The steady-state kinetic parameters k_{cat}, K_M, and k_{cat}/K_M for oct-*ec*ACP were 895 ± 125 min^{-1}, 6 ± 2 μM, and 150 ± 53 μM^{-1}min^{-1}, respectively. The k_{cat}/K_M for oct-*ec*ACP increased 75-fold compared to octCoA (Table 2.2), in which ACP-based substrates are preferred over CoA-based substrates.

Table 2.2 Steady-state kinetic parameters of *Yp*FabV using *E. coli* acyl-carrier-protein (*ec*ACP) and coenzyme A (CoA) based substrate analogs—octenoyl (C8), decenoyl (C10), and dodeceonyl (C12) CoA.

Substrate	K_M (µM)	k_{cat} (min^{-1})	k_{cat}/K_M (µM^{-1}min^{-1})
trans-2-octenoyl-ecACP	6 ± 2	895 ± 125	150 ± 53
trans-2-octenoyl-CoA	7 ± 1	16 ± 1	2 ± 0.4
trans-2-decenoyl-CoA	23 ± 3	332 ± 20	14 ± 2
trans-2-dodecenoyl-CoA	19 ± 2	1543 ± 66	81 ± 9

It is interesting to note that the K_M values for the oct-*ec*ACP and octCoA substrates are similar, while the k_{cat} for the oct-*ec*ACP is significantly higher. Since k_{cat} was exclusively affected, a reaction step following substrate binding was impacted indicating that the increase in the catalytic efficiency is most likely due to remote substrate binding interactions between oct-*ec*ACP and enzyme.

Although the fatty acid thioesters of ACP are the natural substrates for the ENRs, all FabIs and FabV to date are able to accept the enoyl-CoA substrates or artificial carrier molecules (*30, 36, 40, 41, 43, 44, 91-93*). Subsequently, enoyl-CoA substrates were used to assay this enzyme because enoyl-CoA substrates are easier to synthesize and purify than the natural enoyl-ACP substrates. The catalytic efficiency of *Yp*FabV was further characterized to determine the substrate carbon-length preference using CoA-based substrate analogs—octCoA, *trans*-2-decenoyl-CoA (decCoA), and *trans*-2-dodecenoyl-CoA (ddCoA). The steady-state kinetic parameters are summarized in Table 2.2 and they indicate an enzyme preference for longer acyl

chains over shorter acyl chains. This trend resembles similar substrate preferences by ENR FabI

class (*30, 44, 94*).

Table 2.3 Binding constants and mechanism summary for *Yp*FabV and its mutants.

Enzyme	K_M (µM)		K_d (µM)		Substrate Binding Mechanism	k_{cat}/K_M (µM^{-1}min^{-1})
	NADH	ddCoA	NADH	ddCoA		
Wt *Yp*FabV	10 ± 2	19 ± 2	13 ± 0.8	13 ± 0.7	Random	81 ± 9
T276S *Yp*FabV	32 ± 8	18 ± 2	4 ± 0.05	33 ± 0.4	Ordered	92 ± 12
T276A *Yp*FabV	129 ± 23	53 ± 5	11 ± 0.4	3 ± 0.2	Ordered	1 ± 0.2
T276G *Yp*FabV	78 ± 17	38 ± 6	2 ± 0.3	47 ± 4	Ordered	10 ± 2
T276C *Yp*FabV	—	—	1 ± 0.2	4 ± 0.3	—	—
T276V *Yp*FabV	150 ± 20	17 ± 3	112 ± 4	3 ± 0.5	Ordered	1 ± 0.1
T276Y *Yp*FabV	364 ± 65	15 ± 2	120 ± 1	2 ± 0.1	Ordered	0.31 ± 0.04

YpFabV catalyzes substrate reduction via a random bi-bi mechanism

To investigate the substrate binding mechanism of *Yp*FabV, a matrix of initial velocities

was measured at varying concentrations of ddCoA and NADH. Analyses by double-reciprocal

plots permit the discrimination between a ternary complex mechanism and a ping-pong

mechanism of substrate binding. Since the double-reciprocal plots converged to the left of the y-

axis when both substrates were varied, the results were indicative of a ternary complex

mechanism (Figure 2.1.A and 2.1.B) (*95, 96*), eliminating the possibility of a ping-pong

mechanism. Product inhibition studies were then used to analyze the order of substrate addition

and differentiate between ordered and random bi-bi mechanisms. We thus investigated the

pattern of inhibition caused by the products lauroyl CoA and NAD$^+$. At subsaturating substrate

concentrations, NAD$^+$ was competitive with respect to NADH and ddCoA (Figure 2.1.C and

2.1.D). Product inhibition studies with lauroyl CoA coincided with this finding, such that lauroyl CoA was competitive with respect to NADH and ddCoA (Figure 2.2). Thus, this combination of product inhibition patterns indicated that substrate reduction occurs through a random bi-bi mechanism (*95, 96*). Fluorescence binding experiments further validated the ability of both substrates to bind to the free enzyme (Table 2.3). The K_d values for NADH and ddCoA were 13 $\pm$ 0.8 μM and 13 $\pm$ 0.7 μM, thereby supporting a random bi-bi mechanism (Scheme 2.2).
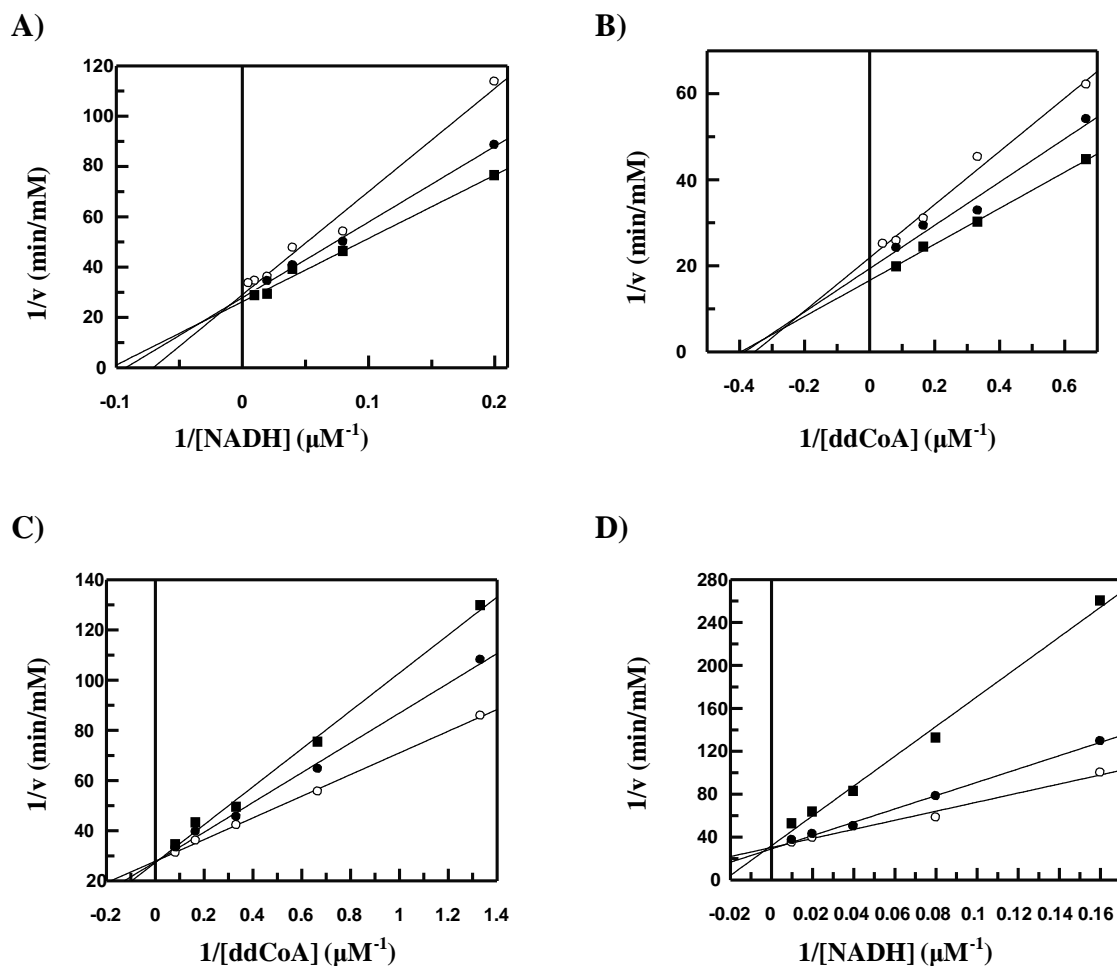
Figure 2.1 Two-substrate steady-state kinetics and product inhibition studies to determine the substrate binding mechanism of wild-type *Yp*FabV.
Initial velocity patterns: (A) 1/v versus 1/[NADH] double-reciprocal plot in which [ddCoA] was fixed (**O**) 6 μM ddCoA, (•) 12 μM ddCoA, and (□) 24 μM ddCoA. (B) 1/v versus 1/[ddCoA] double-reciprocal plot in which [NADH] was fixed at (**O**) 50 μM NADH, (•) 100 μM NADH, and (□) 250 μM NADH. To evaluate product inhibition, one substrate concentration was varied, while the second substrate concentration was fixed and in the presence of NAD^+. Initial velocity patterns: (C) 1/v versus 1/[ddCoA] double-reciprocal plot in which $[NAD^+]$ was fixed at (**O**) 0 μM NAD^+, (•) 50 μM NAD^+, and (□) 100 μM NAD^+. (D) 1/v versus 1/[NADH] double-reciprocal plot in which $[NAD^+]$ was fixed at (**O**) 0 μM NAD^+, (•) 50 μM NAD^+, and (□) 100 μM NAD^+.

30

A)

B)

Figure 2.2 Product inhibition studies to determine the substrate binding mechanism of *Yp*FabV.

Initial velocity patterns: (A) 1/v versus 1/[ddCoA] double-reciprocal plot in which [Lauroyl CoA] was fixed at (**O**) 0 μM Lauroyl CoA, (□) 8 μM Lauroyl CoA and (•) 16 μM Lauroyl CoA. (B) 1/v versus 1/[NADH] double-reciprocal plot in which [Lauroyl CoA] was fixed at (**O**) 0 μM Lauroyl CoA, (•) 8 μM Lauroyl CoA and (□) 16 μM Lauroyl CoA.
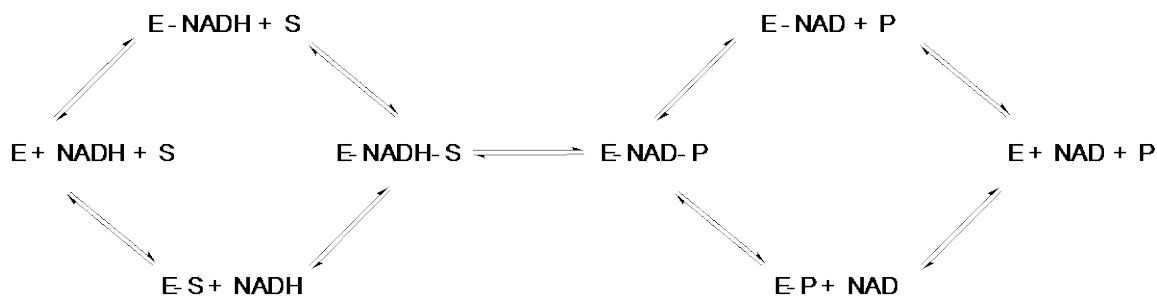
Scheme 2.2 Wild-type *Yp*FabV catalyzes substrate reduction via a random bi-bi mechanism.

E= free enzyme; S=substrate; P=product.

The hydroxyl side-chain of T276 enhances the binding affinity of NADH in the active site, while the methyl side-chain of T276 enhances the binding affinity of the enoyl-CoA substrate

Direct binding experiments for *Yp*FabV showed that both substrates could bind to the free enzyme and these values were comparable to the binding of each substrate to the binary complex. Therefore, we hypothesized that the random bi-bi mechanism may correlate with the similar binding affinity of NADH and ddCoA for the free enzyme. The role of amino acids in the substrate binding loop that could enhance or decrease NADH or ddCoA binding affinity led us to evaluate the substrate specificity and mechanism of *Yp*FabV mutants at position T276 (Table 2.3). This threonine residue was reported to be essential for enzymatic activity in *Xanthomonas oryzae* FabV (*99*). Also, we isolated a T276S *Yp*FabV variant from the pathogenic strain *Y. pestis* CO92 and we speculated it to be a spontaneous mutation caused by exposure to triclosan (*42*).

In this study, when T276 was mutated to alanine in *Y. pestis* FabV, the k_{cat}/K_M decreased by 81-fold compared to the wild-type enzyme. The methyl side-chain of alanine may have hydrophobic interactions with ddCoA since the binding affinity of the substrate increased by approximately 4-fold compared to the wild-type enzyme. Also, the T276V and T276Y *Yp*FabV mutants had comparable K_d values for ddCoA as T276A. The data reveal that the methyl-group in threonine may play an important role in the active site by providing favorable hydrophobic interactions to promote binding to the enoyl substrate. The loss of these preferential hydrophobic interactions is illustrated by the weaker binding affinity of ddCoA to T276G and T276S *Yp*FabV. The binding affinity for ddCoA to T276C *Yp*FabV mutant also resembled the K_d values for T276A, T276V and T276Y *Yp*FabV mutants.

32

Alanine has the least bulky side-chain compared to valine and tyrosine, and this side-chain can promote a comparable binding affinity of NADH to T276A mutant as the wild-type enzyme. The binding affinity decreased by at least 8-fold for NADH to both T276V and T276Y YpFabV mutants. The k_{cat}/K_M decreased by 81- and 270-fold for T276V and T276Y YpFabV mutants. NADH binds favorably to T276G, T276C, and T276S YpFabV, where the binding affinities increased approximately by 6-, 13-, and 3-fold.

The k_{cat}/K_M decreased by 8-fold for T276G YpFabV mutant, while the k_{cat}/K_M for T276S YpFabV was comparable to that of the wild-type enzyme. The T276C YpFabV mutant did not have detectable activity within the limit of detection of our assay. To determine if the lack of activity for the T276C YpFabV mutant was due to a low k_{cat}, we assayed this enzyme using $trans$-2-dodecenoyl-ecACP, C12-ecACP (Table 2.4). Substitution of the enoyl-CoA substrate with an enoyl-ACP substrate allowed us to assay the effect of k_{cat} because we showed that ACP substrates affected k_{cat} and not K_M for the wild-type enzyme. Using C12-ecACP substrates, we found that the k_{cat}/K_M for T276C YpFabV was approximately 80,000-fold smaller than that of the wild-type enzyme. Since the K_M values for C12-ecACP to the wild-type enzyme and T276C YpFabV were comparable, the change in k_{cat}/K_M is exclusively affected by k_{cat}. Thus, the cysteine residue destabilizes the rate limiting transition state on the reaction pathway following substrate binding.

Table 2.4 Catalytic efficiency and binding constants for FabV and its mutants, using *trans*-2-dodecenoyl-ecACP substrates.

Enzyme	K_M (μM)	k_{cat}/K_M (μM^{-1}min^{-1})
wild-type *Yp*FabV	11 ± 2	819 ± 159
T276C *Yp*FabV	28 ± 2	0.01 ± 0.0009
T276Y *Yp*FabV	11 ± 2	0.07 ± 0.01

A mutation in the substrate binding loop changes YpFabV substrate binding mechanism from random to ordered bi-bi

Dr. Nina Liu investigated the substrate binding mechanism of T276S *Yp*FabV and analysis of the double-reciprocal plots showed that the substrate binding mechanism follows a ternary complex mechanism (Figure 2.3.A and 2.3.B) (*95, 96*). Product inhibition studies revealed that NAD$^+$ follows a competitive pattern with respect to NADH, and a noncompetitive pattern with respect to ddCoA (Figure 2.3.C and 2.3.D). The product inhibition pattern indicates that the substrates bind via an ordered bi-bi mechanism, in which NADH binds first to the enzyme (Scheme 2.3) (*95, 96*). The substrate binding mechanism for this mutant differs from the wild-type enzyme, which occurs via random bi-bi.

In order to investigate the mechanistic basis for the change in substrate binding mechanism from random to ordered bi-bi, we evaluated the substrate binding mechanism for the T276 mutants (Ala, Tyr, Val, and Gly). Product inhibition plots with lauroyl CoA for all tested T276 mutants showed substrate reduction occurs through an ordered bi-bi mechanism, in which NADH binds first to each enzyme (Figure 2.4-2.7). Data suggest that the enzyme-NADH

complex is preferred over the enzyme-ddCoA complex for an enzyme activity. The binding affinity of ddCoA to the Ala, Val, and Tyr mutants increased by 3- to 6- fold in comparison to wild-type, yet the formation of the ternary complex was not preferential if ddCoA binds first to the enzyme. This implies that productive substrate binding and the formation of enzyme-NADH complex are needed for efficient catalysis.

A)

B)

C)

D)
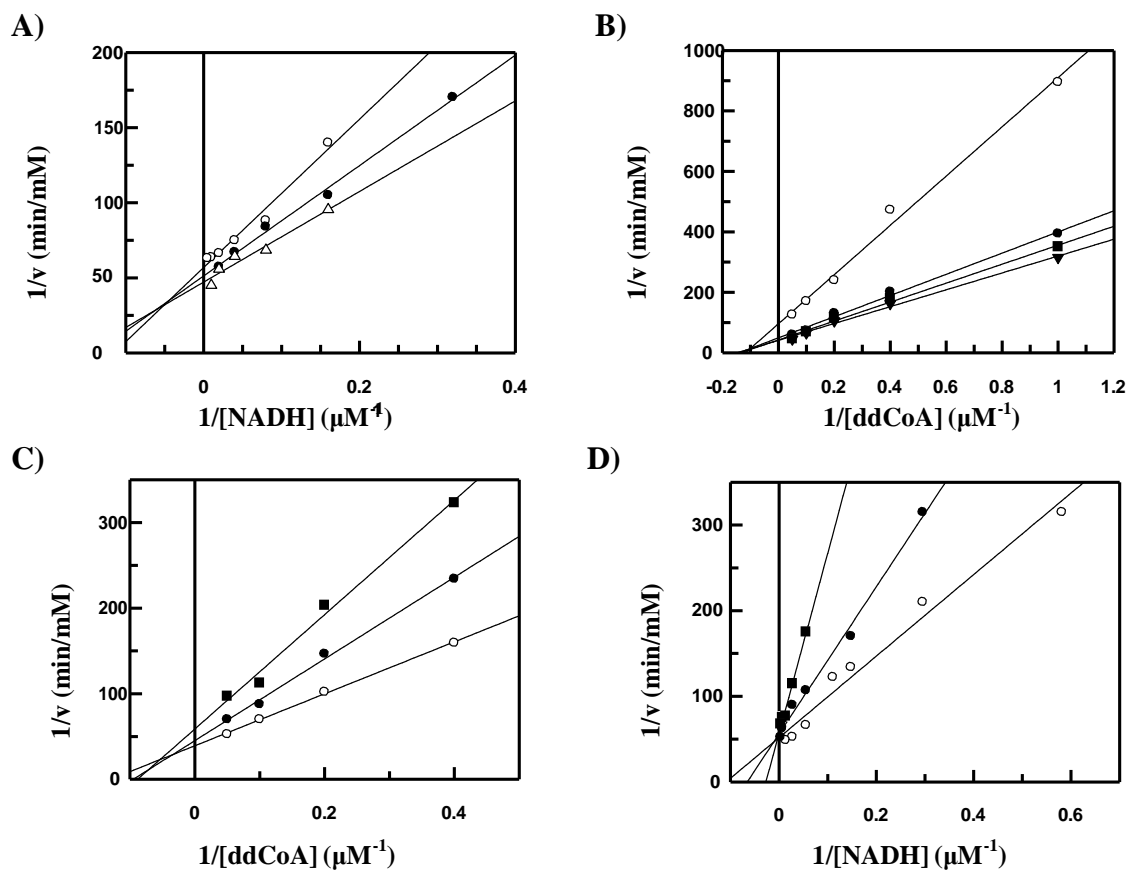
Figure 2.3 Two-substrate steady-state kinetics and product inhibition studies to determine the substrate binding mechanism of T276S *Yp*FabV.
Data provided by Dr. Nina Liu. Initial velocity patterns: (A) 1/v versus 1/[NADH] double-reciprocal plot in which [ddCoA] was fixed at (O) 6 μM ddCoA, (•) 12 μM ddCoA, and (Δ) 24 μM ddCoA. (B) 1/v versus 1/[ddCoA] double-reciprocal plot in which [NADH] was fixed at (O) 10 μM NADH, (•) 33 μM NADH, (□) 100 μM NADH, and (▼) 250 μM NADH. To evaluate product inhibition, one substrate concentration was varied, while the second substrate concentration was fixed and in the presence of NAD^+. Initial velocity patterns: (C) 1/v versus 1/[ddCoA] double-reciprocal plot in which $[NAD^+]$ was fixed at (O) 0 μM NAD^+, (•) 50 μM NAD^+, and (□) 100 μM NAD^+. (D) 1/v versus 1/[NADH] double-reciprocal plot in which $[NAD^+]$ was fixed at (O) 0 μM NAD^+, (•) 50 μM NAD^+, and (□) 100 μM NAD^+.

36

Scheme 2.3 T276S *Yp*FabV catalyzes substrate reduction via an ordered bi-bi mechanism.
E= free enzyme; S=substrate; P=product

A)

B)
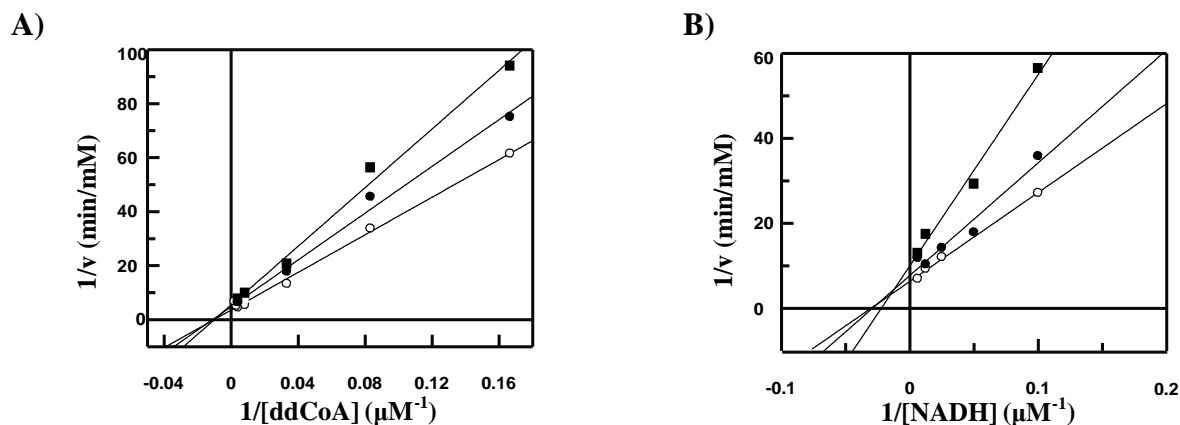
Figure 2.4 Product inhibition studies to determine the substrate binding mechanism of T276A *Yp*FabV.
Initial velocity patterns for T276A (A) 1/v versus 1/[ddCoA] double-reciprocal plot in which [lauroyl CoA] was fixed at (O) 0 μM lauroyl CoA, (•) 6 μM lauroyl CoA, and (□) 12 μM lauroyl CoA. (B) 1/v versus 1/[NADH] double-reciprocal plot in which [lauroyl CoA] was fixed at (O) 0 μM lauroyl CoA, (•) 6 μM lauroyl CoA, and (□) 12 μM lauroyl CoA.

37

A)

B)

Figure 2.5 Product inhibition studies to determine the substrate binding mechanism of T276G *Yp*FabV.
Initial velocity patterns: (A) 1/v versus 1/[ddCoA] double-reciprocal plot in which [lauroyl CoA] was fixed at (**O**) 0 μM lauroyl CoA, (•) 5 μM lauroyl CoA, and (□) 10 μM lauroyl CoA. (B) 1/v versus 1/[NADH] double-reciprocal plot in which [lauroyl CoA] was fixed at (**O**) 0 μM lauroyl CoA, (•) 5 μM lauroyl CoA, and (□) 10 μM lauroyl CoA.

A)

B)

Figure 2.6 Product inhibition studies to determine the substrate binding mechanism of T276V *Yp*FabV.
Initial velocity patterns: (A) 1/v versus 1/[ddCoA] double-reciprocal plot in which [lauroyl CoA] was fixed at (**O**) 0 μM lauroyl CoA, (•) 15 μM lauroyl CoA, and (□) 30 μM lauroyl CoA. (B) 1/v versus 1/[NADH] double-reciprocal plot in which [lauroyl CoA] was fixed at (**O**) 0 μM lauroyl CoA, (•) 15 μM lauroyl CoA, and (□) 30 μM lauroyl CoA.

38

A)

B)

Figure 2.7 Product inhibition studies to determine the substrate binding mechanism of T276Y *Yp*FabV.
Initial velocity patterns: (A) 1/v versus 1/[ddCoA] double-reciprocal plot in which [lauroyl CoA] was fixed at (**O**) 0 μM lauroyl CoA, (•) 15 μM lauroyl CoA, and (□) 30 μM lauroyl CoA. (B) 1/v versus 1/[NADH] double-reciprocal plot in which [lauroyl CoA] was fixed at (**O**) 0 μM lauroyl CoA, (•) 15 μM lauroyl CoA, and (□) 30 μM lauroyl CoA.

Ordered water molecules mediate additional interactions in the active site and provide structural evidence for changes in the NADH binding affinity to T276S YpFabV

In order to explore the role of T276 in controlling the order of substrate addition, we crystallized wild-type *Yp*FabV in the same conditions as the previously described variant T276S by Dr. Maria Hirschbeck (PDB: 3ZU3 and Table S2) (*42*). The structures showed no major differences in their tertiary structure. Pairwise comparison between the structures was conducted using the DaliLite server (*98*). The His-tagged and non His-tagged structures of wild-type *Yp*FabV aligned with a root-mean-square deviation (RMSD) of 0.6 Å. Superposition of the wild-type *Yp*FabV with the T276S *Yp*FabV, both without a His-tag, yielded a RMSD value of only 0.4 Å.

Residue T276 displays the same conformation as S276 in the variant—apart from its additional methyl group (Figure 2.8.A). Direct interactions between residue 276 and the cofactor NADH were retained in both structures, including hydrogen bonds between the hydroxyl group of T/S276 and the nicotinamide moiety, as well as to the adjacent phosphate group (Figure 2.8.A). However, the X-ray crystal structure of T276S *Yp*FabV contained two additional bound water molecules in close proximity to S276 that are extruded by the methyl group of T276 in the wild-type structure. One of the water molecules mediates an additional interaction between the sulfhydryl group of C306 and the pyrophosphate of NADH (Figure 2.8.B). Thus, the two bound solvent molecules have a beneficial effect, such that they provide additional interactions that can mediate NADH binding affinity to T276S *Yp*FabV.

We wanted to further explore structural elements that could affect the substrate binding mechanism by comparing the structure of *Yp*FabV to *B. pseudomallei* FabV (*Bp*FabV). *Bp*FabV was selected because it catalyzes substrate reduction via an ordered bi-bi mechanism (Figure 2.9) like the previously characterized FabV enzyme from *B. mallei (40)*. Also, the catalytic efficiencies for enoyl-CoA-based substrates with *Bp*FabV were approximately 5-fold higher than *Yp*FabV (Table 2.5). *Bp*FabV crystallized only in the apo form, which prevented comparison of direct interactions with the cofactor. All residues that were described to contribute to NADH binding in *Yp*FabV are conserved in *Bp*FabV, except L139 in *Yp*FabV is replaced by V139 in *Bp*FabV. The backbone carbonyl oxygen for this residue interacts with the cofactor; thus, this interaction could be present in *Bp*FabV as well. The overall structure of apo *Bp*FabV showed no major differences in comparison to other FabV structures (*42, 99*), and could be superimposed

40

with the structure of wild-type *Yp*FabV with an RMSD value of 1.2 Å. The substrate binding loop is in a closed conformation in which T275 displays the same conformation as in the NADH-bound form of *Yp*FabV, but is shifted by about 1 Å (measured at Cα) due to the slightly different orientation of the substrate binding loop (Figure 2.8.C).

There are four water molecules within 4 Å of T275. Two water molecules act as placeholder for the missing interactions that were observed in the presence of NADH. In contrast to the T276S *Yp*FabV structure, no water molecules are located in close proximity to C306. Based on the structure it still remains unclear why *Bp*FabV catalyzes substrate reduction via an ordered bi-bi mechanism whereas *Yp*FabV follows a random bi-bi mechanism.

Table 2.5 Enzyme catalytic efficiency comparisons of *Yp*FabV and *Bp*FabV using CoA-based substrates.

Substrate	k_{cat}/K_M ($\mu M^{-1} min^{-1}$)	
	*Yp*FabV (15nM)	*Bp*FabV (7.5nM)
trans-2-octenoyl-CoA	2 ± 0.4	9 ± 1
trans-2-decenoyl-CoA	14 ± 2	64 ± 8
trans-2-dodecenoyl-CoA	81 ± 9	408 ± 42
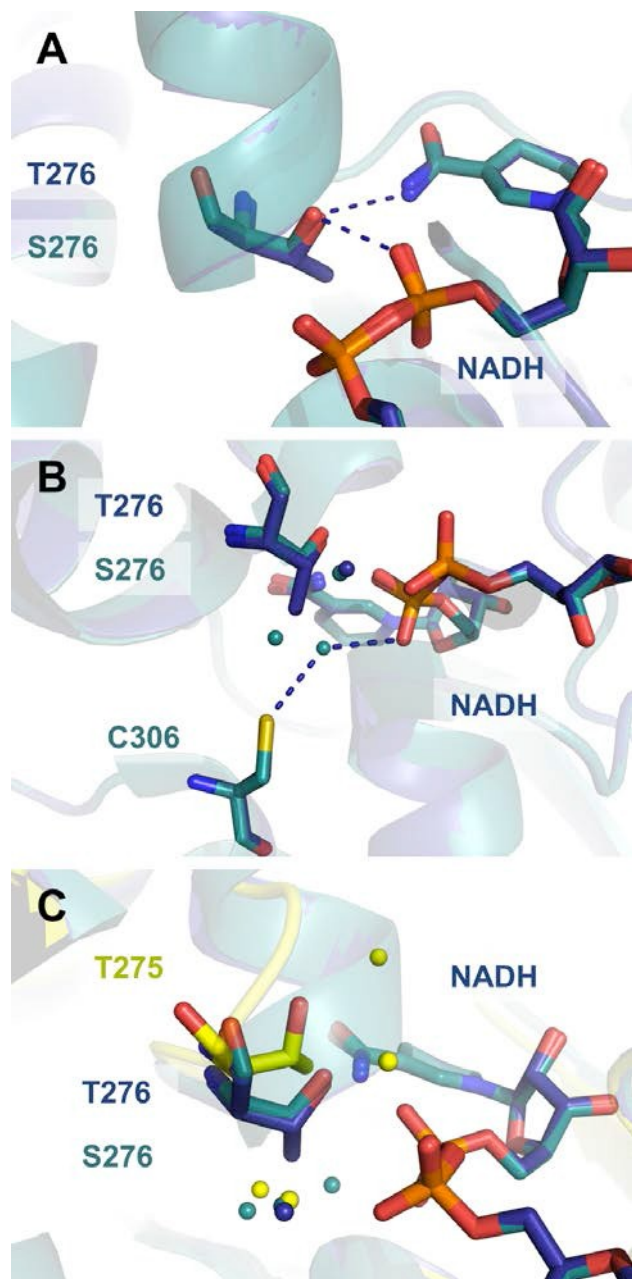
Figure 2.8 Differences in the structures of wild-type *Yp*FabV, T276S *Yp*FabV, and apo *Bp*FabV provided by Dr. Maria Hirschbeck.
(A and B) Superposition of wild-type *Yp*FabV and T276S *Yp*FabV (PDB: 3ZU3) bound to NADH. (C) Superposition of wild-type *Yp*FabV and T276S *Yp*FabV, and apo *Bp*FabV. Wild-type YpFabV is shown in blue; T276S *Yp*FabV is shown in cyan; apo *Bp*FabV is shown in yellow; and hydrogen bonding interaction are represented by dashes. All water molecules are depicted as spheres.

A)

B)
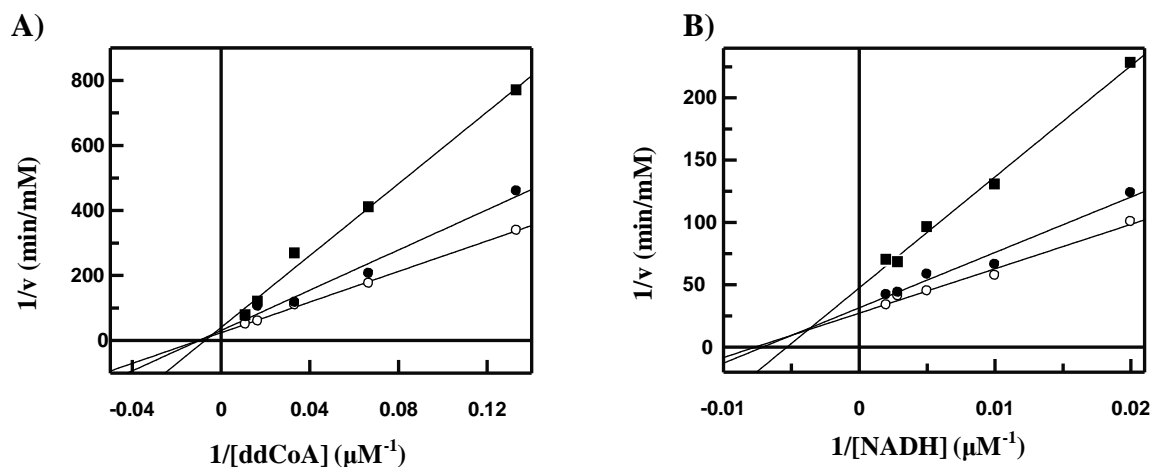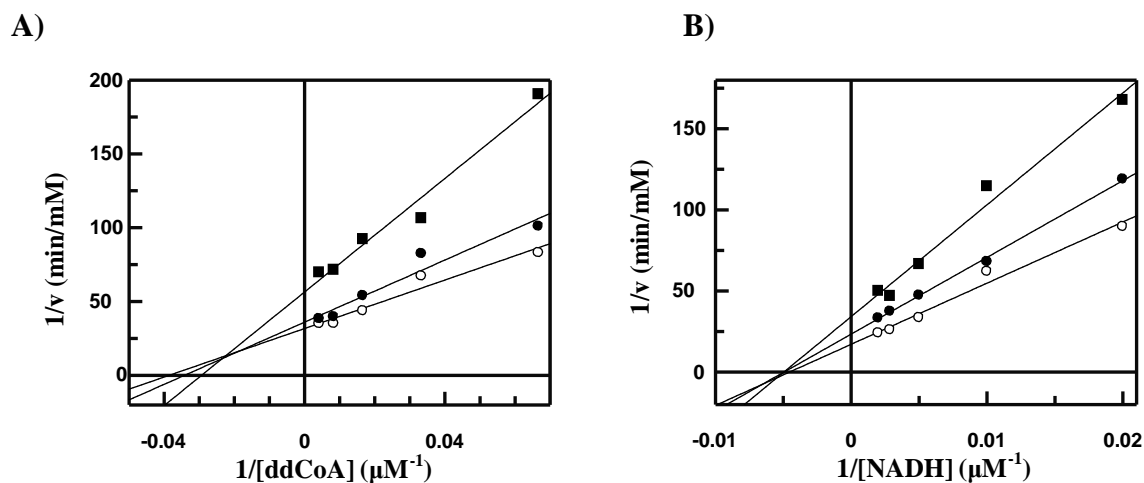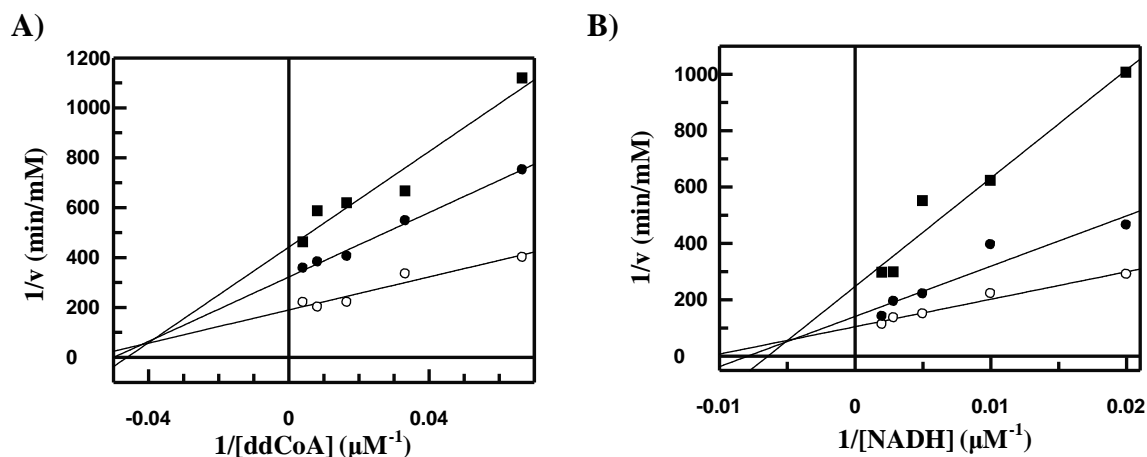

C)

D)
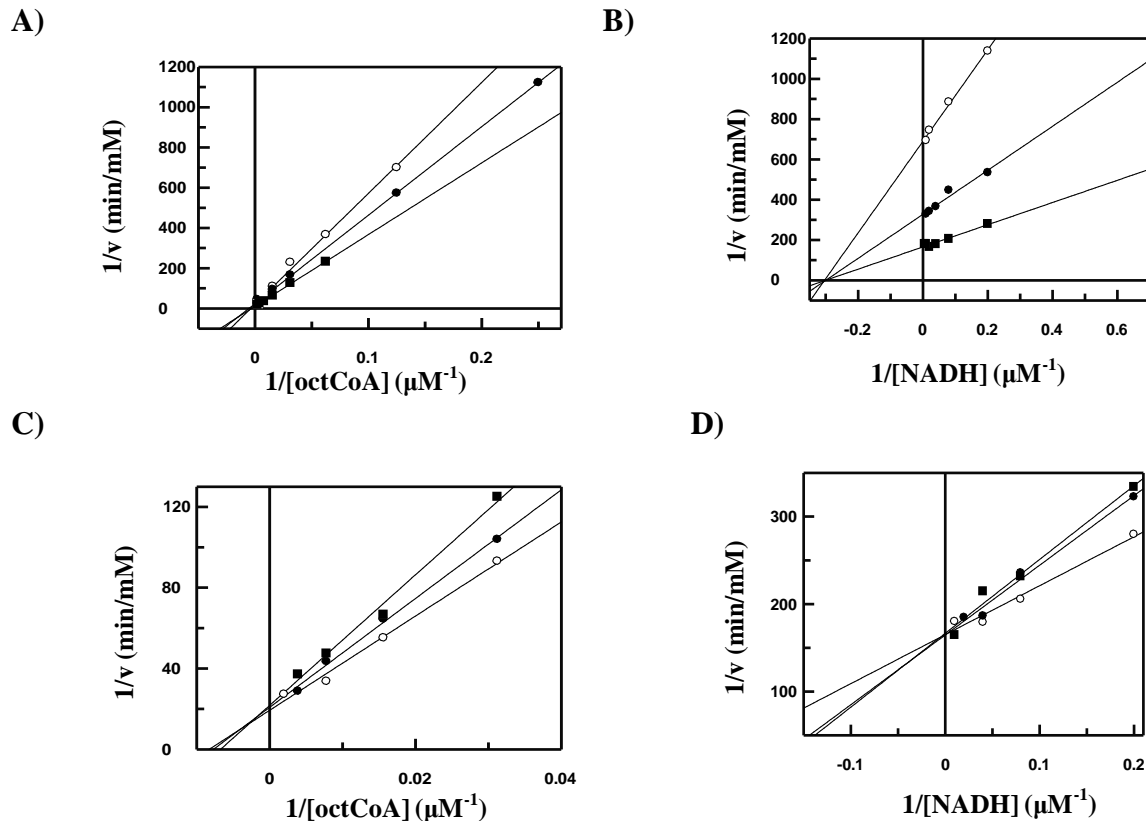
Figure 2.9 Two-substrate steady-state kinetics and product inhibition studies to determine the substrate binding mechanism of *Bp*FabV.
Initial velocity patterns: (A) 1/v versus 1/[octCoA] double-reciprocal plot in which [NADH] was fixed at (O) 50 μM NADH, (•) 100 μM NADH, and (□) 250 μM NADH. (B) 1/v versus 1/[NADH] double-reciprocal plot in which [octCoA] was fixed at (O) 8 μM octCoA, (•) 16 μM octCoA, and (□) 32 μM octCoA. To evaluate product inhibition, one substrate concentration was varied, while the second substrate concentration was fixed and in the presence of NAD^+. Initial velocity patterns: (C) 1/v versus 1/[octCoA] double-reciprocal plot in which [NAD^+] was fixed at (O) 0 μM NAD^+, (•) 50 μM NAD^+, and (□) 100 μM NAD^+. (D) 1/v versus 1/[NADH] double-reciprocal plot in which [NAD^+] was fixed at (O) 0 μM NAD^+, (•) 50 μM NAD^+, and (□) 100 μM NAD^+.

43

Discussion

The structure of T276S *Y. pestis* FabV in complex with NADH was solved by Hirschbeck *et al* (*42*), along with complexes bound to 2-pyridone inhibitors. Structural studies showed the entry of the substrate-mimic inhibitor into the major portal of active site was coupled with the opening of the substrate binding loop, which may resemble the coupling interaction between FabV and its ACP substrate. Although these key structural insights provided a glimpse into substrate recognition, there is currently little mechanistic information available on substrate recognition for wild-type *Yp*FabV. Thus, kinetic analysis of the substrate specificity and binding mechanism for wild-type *Yp*FabV will provide better mechanistic insights for the FabV ENR class.

We found that *Yp*FabV undergoes substrate turnover with an increased catalytic efficiency in the presence of enoyl-ACP substrate, in which k_{cat} was exclusively affected and K_M was unchanged. Since k_{cat} rather than K_m was affected, binding of the ACP-based substrate must stabilize the rate-limiting transition state following substrate binding. The increase in the catalytic efficiency is most likely due to remote substrate binding interactions between the acyl-ACP and enzyme. It is not atypical for enzymes to have remote binding interactions with their substrates; for an example, Whitty *et al* showed that the predominant contribution of a 10^6 increase in k_{cat}/K_M for the 3-oxoacid coenzyme A transferase was due to k_{cat}, which increased by a factor about 10^5 (*100*). Enzymes can utilize remote binding interactions in which they bind to nonreactive portions of the substrates and gain intrinsic binding energy from noncovalent interactions. If this occurs, the transition state can be stabilized to further increase the rate

constant for the reaction *(101, 102)*. An increase in the rate of the reaction for an enzyme-substrate complex can be accomplished by a combination of four different mechanisms: (1) induced fit; (2) destabilization of the substrate; (3) productive binding; and (4) entropy loss (*102, 103*).

The similarity in K_M values for ACP- and CoA-based substrates was unexpected. ACP-based substrates normally bind with higher affinity than CoA-based substrates to the other ENR isoforms, such that the K_M is significantly reduced whereas k_{cat} is unaffected. For example, the K_M values for ACP-based substrates with the FabI ENR isoforms from *B. pseudomallei (94), E. coli (87), F. tularensis, (104)* and *M. tuberculosis (30)* decreased by approximately 7-, 8-, 16-, and 233-fold, in comparison to the CoA-based substrates; yet, k_{cat} remained unchanged. We speculate this observation may be due to differences in structural elements between FabI and FabV. For instance, structural overlays of *E. coli* FabI and T276S *Yp*FabV reveal that FabV lacks the conserved basic residue patch that is needed to bind to ACP. Also, the potential entry portal nearby the ACP substrate recognition helix found in FabI is blocked by two additional β-hairpins that are found in the FabV enzyme. These differences suggest ACP binds to a different basic patch on the FabV enzyme compared to FabI (*42*).

Another interesting finding was that *Yp*FabV catalyzed substrate reduction via a random bi-bi mechanism. This was an unexpected since the studied SDR superfamily ENRs from *B. mallei (40), B. pseudomallei (94), F. tularensis, (104),* and *Staphylococcus aureus (44)* were shown to catalyze substrate reduction via an ordered sequential bi-bi mechanism. There were no

significant differences between the K_d and K_M values for NADH and ddCoA to *Yp*FabV, revealing the substrates can bind to either the free enzyme or binary complex (Table 2.3). Until now, InhA from *M. tuberculosis* was the only other ENR that has a kinetic mechanism that is not strictly ordered. However, InhA was shown to have a preference for NADH to bind first followed by the enoyl-substrate *(30)*.

Direct binding experiments demonstrate that NADH and ddCoA have similar affinity for wild-type *Yp*FabV, supporting the observation of a random bi-bi mechanism. Amino acids in the substrate binding loop that could affect the binding affinity of NADH and ddCoA led us to evaluate the substrate specificity and mechanism of the T276 mutants. We were particularly interested in this position because this threonine residue in *Xanthomonas oryzae* FabV was reported to be essential for enzymatic activity, in which a T276A mutant displayed no detectable NADH oxidation (*99*). Furthermore, this residue is structurally conserved amongst the FabV and FabI ENRs at the N-terminal end of the helical substrate binding loop (Figure 2.10).
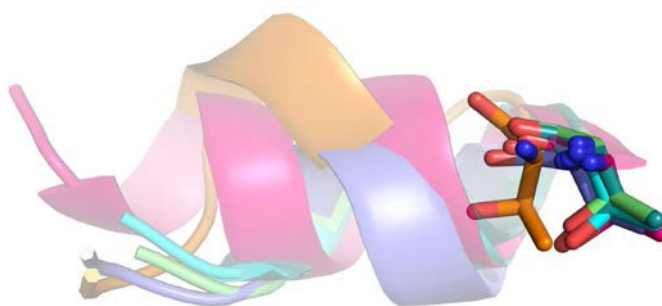
Figure 2.10 Alignment of substrate binding loop for selected FabV and FabI ENRs.
Y. pestis FabV in dark blue; *B. pseudomallei* FabV in orange; *E. coli* FabI (PDB: 1QG6) in light blue; *S. aureus* FabI (PDB: 4ALL) in light green; *F. tularensis* FabI (PDB: 3NRC) in dark green; and *M. tuberculosis* FabI (PDB: 2X22) in pink.

We found that T276 in FabV plays an important role for the binding of both substrates. The hydroxyl side-chain of T276 enhances the binding affinity of NADH in the active site, while the methyl side-chain of T276 enhances the binding affinity of the acyl-CoA substrate. We speculate the T276 mutants' ternary complex reaction classifications are based on (1) productive substrate binding, (2) the formation of enzyme-NADH complex, and (3) stabilization of the rate-limiting transition state. These factors are exemplified through the binding of NADH and ddCoA to T276C YpFabV with K_d values of 1 ± 0.2 μM and 4 ± 0.3 μM; yet, there was no detectable activity. Despite the fact that the mutant does not reduce the enoyl-CoA substrate, it must destablize the rate-limiting transition state on the basis of the reduction of the enoyl-ACP substrate with T276C mutant.

The formation of the E-NADH-ddCoA complex was less favorable if ddCoA binds first to the free enzyme for the Ala, Val, and Tyr mutants (Table 2.3). The ternary complex formation preference is illustrated by higher K_M values for NADH binding to the enzyme-ddCoA complex compared to the K_M values for ddCoA binding to the enzyme-NADH complex for the T276A, T276V, and T276Y YpFabV mutants. As for the T276S and T276G YpFabV mutants, the weaker binding affinity for ddCoA and the increase binding affinity of NADH to the free enzyme may promote an ordered bi-bi substrate binding mechanism, in which NADH binds first to the enzyme.

A Thr to Ser is a modest structural change and at the outset we predict a minimal effect on catalysis. Our data revealed that T276S YpFabV retained a k_{cat}/K_M that was comparable to the wild-type enzyme and this mutant switched the substrate binding mechanism from a random bi-

bi to an ordered bi-bi mechanism, in which NADH binds first to the enzyme. NADH displayed an approximate 8-fold binding affinity preference over ddCoA for T276S *Yp*FabV, and structural evidence supported this finding. In the T276S *Yp*FabV structure, two additional bound water molecules are in close proximity to S276 and one of the water molecules mediates additional hydrogen bonding interactions with C306 and the pyrophosphate of NADH, which is not present in the wild-type structure.

It is not atypical for a mutant to increase binding affinity for a cofactor and consequently alter the order of substrate binding. For example, studies by Rendina *et al* revealed wild-type isocitrate dehydrogenase 1 (IDH1) follows a random sequential mechanism to produce α-ketoglutarate (αKG). Yet, the R132H IDH1 follows an ordered sequential mechanism in which the enzyme has a higher affinity for NADPH than wild-type IDH1 and also alters the reaction such that NADPH-dependent reduction of α-KG to 2-hydroxyglutarate occurs (*106*). Despite the fact that T276S *Yp*FabV displays a sequential ordered bi-bi substrate binding mechanism like *Bp*FabV, it is possible that residue 276 and NADH binding affinity do not directly affect the substrate binding mechanisms for *Bp*FabV.

In conclusion, it is essential to have better mechanistic understanding for the FabV ENR to expand our current knowledge of the ENR classes. In this study, we found that T276 was an important residue for substrate recognition and it is possible that additional residues within or nearby the substrate binding loop contribute to the order of substrate binding. Furthermore, in Chapter 3 we will evaluate the affect that the substrate binding mechanism has on the mode of

inhibition for inhibitors that target FabV because FabV is an unexploited, yet promising drug target in biodefense agents and clinically relevant pathogens.

Chapter 3: Probing the Mode of Inhibition of the *Yersinia pestis* Enoyl-ACP Reductase FabV

Background

Enoyl-ACP Reductase, a Novel Drug Target

The Gram-negative bacterium, *Yersinia pestis*, is the causative agent of plague and it has gained much attention due to its potential use as a biological warfare agent [107]. As a result, *Y. pestis* is now classified as a Tier 1 Biological Select Agent or Toxin (BSAT) by the Centers for Disease Control and Prevention (CDC). Even in the 21st century there have been serious outbreaks of plague in Africa, Asia and the Americas [108]. Although antibiotics such as streptomycin or doxycycline [108] are effective in the treatment of the *Y. pestis* infections, emergence of resistant strains [86, 109, 110] underscores the need for novel chemotherapeutics. The fatty acid biosynthesis type II (FAS-II) pathway synthesizes fatty acid precursors of the phospholipid bilayer of the cell membrane. Since most of the FAS-II enzymes are essential for bacterial viability (*19*), the FAS-II enzymes can be promising drug targets.

The last reaction in the elongation cycle of the FAS-II pathway is catalyzed by the enoyl-ACP reductase (ENR). To date, there are four known ENR classes: FabI, FabK, FabL, and FabV. The biological reasons for bacterial expression of different ENR classes or combinations thereof are currently unknown. Thus, it may be possible that the biosynthesis of fatty acids in certain bacteria will only be fully compromised by inhibition of all the ENRs.

One challenge that arises when targeting ENR classes is their differential sensitivity to inhibitors. The broad spectrum antiseptic triclosan, for example, is a known potent, nano/picomolar, slow-onset inhibitor of the FabI enzymes from *E. coli (91, 93)*, *Francisella tularensis (41)*, and *B. pseudomallei (94)*, but is only a low micromolar, rapid reversible inhibitor of the *Mycobacterium tuberculosis* ENR FabI (InhA) (*89*). *Streptococcus pneumoniae* ENR FabK activity is 100-fold more resistant to triclosan than *E. coli* FabI (*34*). Triclosan is also a high micromolar, rapid reversible inhibitor of the *Bacillus subtilis* ENR FabL (*38*). Furthermore, triclosan was is a low micromolar, rapid reversible inhibitor of *Bm*FabV (*40*), and more recently it was shown that it is a poor high micromolar inhibitor of T726S *Y. pestis* FabV (*42*). Thus, we need to first identify a promising scaffold that generates high affinity inhibitors of FabV ENR class.

Project Goal

*Yp*FabV is an unexploited yet promising drug target because it is the only enoyl-ACP reductase in *Y. pestis* and ENRs have been identified as good drug targets. Our goal is to discover a lead scaffold that can inhibit *Yp*FabV using known FabI inhibitor scaffolds—diphenyl ethers, 2-pyridones, and 4-pyridones (Figure 3.1). We compared the mode of inhibition of each scaffold for wild-type *Yp*FabV and T276S *Yp*FabV because T276S *Yp*FabV is an isolated variant from a pathogenic strain and its inhibition activity was found to be resistant to triclosan.
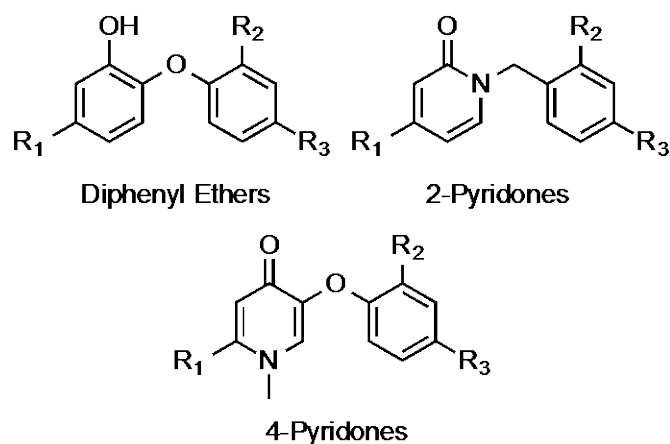
Figure 3.1 FabI inhibitor scaffolds.

Materials and Methods

Materials

His-bind Ni^{2+}-NTA resin was purchased from Invitrogen and the Luria broth was acquired from VWR. The *trans*-2-dodecenoic and *trans*-2-octenoic acids were obtained from TCI and triclosan was purchased from Sigma-Aldrich. All other chemical reagents were purchased from Fisher.

Compound synthesis

The compounds **PT01**-**05** (*111*), **PT10** (*112*), **PT12-13** (*112*), **PT15** (*112*), **PT70** (*113*), **PT91** (*114*), **PT113** (*114*), **PT156-157** (*114*), **PT166** (*114*), **PT171** (*115*), **PT192** (*115*), **PT424** (*115*), and **PT425** (*115*) were synthesized by Dr. Pan Pan, Dr. Gopal R. Bommineni, and Ms. Sonam Shah.

Synthesis of trans-2-dodecenoyl-CoA and trans-2-octenoyl-CoA

The substrates *trans*-2-dodecenoyl-CoA (ddCoA) and *trans*-2-octenoyl-CoA (octCoA) were synthesized from *trans*-2-dodecenoic acid and *trans*-2-octenoic acid using the mixed anhydride method as previously described (*89*).

Expression and purification of enzymes

Y. pestis FabV, *B. pseudomallei* FabV, and *B. pseudomallei* FabI were expressed and purified as previously described using *E. coli* BL21(DE3) pLysS cells (*40, 42, 94*). The concentrations of *Yp*FabV, *Bp*FabV, and *Bp*FabI were spectrophotometrically determined at 280 nm and by using the extinction coefficients 48,360 M^{-1} cm^{-1}, 42,650 $M^{-1}cm^{-1}$, and 13,490 $M^{-1}cm^{-1}$, respectively.

Inhibition assays

The half maximal inhibitory concentration (IC_{50}) values were determined by varying the inhibitor concentration (2% DMSO) in the reactions containing 250 μM NADH and 30 μM ddCoA with *Yp*FabV (15 nM), T276S *Yp*FabV (15 nM), *Bp*FabV (7.5 nM), or *Bp*FabI (30 nM). The experimental data were analyzed using Equation 3.1, in which I is the inhibitor concentration and y represents the percent activity.

$$y = \frac{100\%}{1 + \frac{I}{IC_{50}}}$$

Equation 3.1

Steady-state kinetic analysis

Steady-state kinetics were performed on a Cary 100 Bio spectrophotometer (Varian) at 25 °C in a buffer solution containing 30 mM PIPES, 150 mM NaCl and 1.0 mM EDTA at pH 8.0, as previously reported (*42*). The reaction initial velocities were measured by monitoring the oxidation of NADH to NAD^+ at 340 nm (ε = 6,220 M^{-1} cm^{-1}). Lineweaver-Burk plots were used to determine the inhibition mechanisms at a fixed concentration of 250 μM NADH and varying concentrations of ddCoA and inhibitor. The inhibition constants for competitive, uncompetitive, and noncompetitive inhibitors were analyzed using Equations 3.2-4; where, [S] is the substrate concentration; [I] is the concentration of inhibitor added; K_M is the Michaelis-Menten constant for the substrate; v_{max} is the maximum velocity; and K_i and $K_i^{'}$ are inhibition constants.

$$v_o = \frac{v_{max}[S]}{K_M \left(1 + \frac{[I]}{K_i}\right) + [S]}$$

Equation 3.2

$$v_o = \frac{v_{max}[S]}{K_M + [S](1 + \frac{[I]}{K_i^{'}})}$$

Equation 3.3

$$v_o = \frac{v_{max}[S]}{K_M \left(1 + \frac{[I]}{K_i}\right) + [S](1 + \frac{[I]}{K_i'})}$$

Equation 3.4

Thermal shift assay

ThermoFluor experiments were performed using a CFX96 Real-Time PCR Detection System and C1000 Thermal Cycler (Bio-Rad) to detect the stability of the enzyme and its ternary complex in the presence of the inhibitor. In a total volume of 20 μL, 7.4 μM enzyme, 2.5 mM cofactor (NADH or NAD$^+$) and 25 μM inhibitor (2% DMSO) in a buffer solution containing 30 mM PIPES, 150 mM NaCl and 1.0 mM EDTA at pH 8.0 were added to the wells of a 96-well thin-wall PCR plate (Concord). Upon incubation at 25 °C for 1.5 h, 1 μL of 100 × Sypro Orange (Sigma) was added and the plates were sealed with Microseal 'B' Film (Bio-Rad). The samples were heated from 25 to 90 °C in increments of 0.2 °C/10 s. The Bio-Rad CFX Manager was used to process the data.

Results

Diphenyl ethers can inhibit wild-type YpFabV, yet they are nonspecific for T276S YpFabV

Previous inhibition studies using uncompetitive inhibitors **PT01-PT05** showed that steric properties on the A-ring were important for the binding affinity of triclosan analogues to InhA, in which inhibition constants ranged from 1 to 12 nM (*111*). SAR studies were expanded

55

and uncompetitive inhibitors **PT10, PT12-PT13**, and **PT15** were found to inhibit InhA with inhibition constants ranging from 16 to 40 nM (*112*). Potent compounds, **PT113** and **PT91**, were later synthesized, and they had inhibition constants of 0.1 and 1 nM, respectively (*114*). Therefore, we carried out SAR studies with wild-type *Yp*FabV using these existing FabI inhibitors and triclosan (Table 3.1). We also compared the inhibition of *Yp*FabV to T276S *Yp*FabV, which was an isolated variant from a pathogenic *Y. pestis* stain.
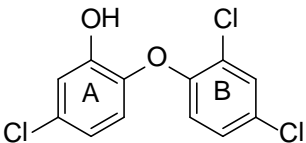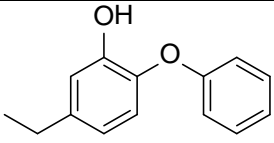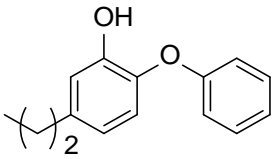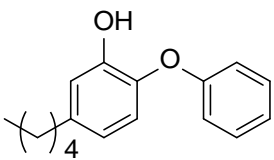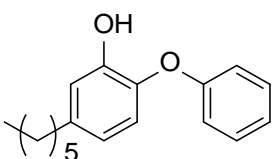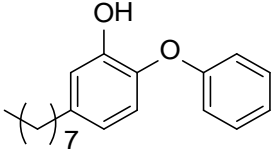
Triclosan inhibited *Yp*FabV with an IC_{50} value around 5 µM, whereas T276S *Yp*FabV lost inhibitor potency by 20-fold with an IC_{50} value greater than 100 µM. To investigate potential steric effects on the A-ring, alkyl groups with different chain lengths were coupled to the 5-position on the inhibitor's A-ring. The alkyl groups would mimic the alkyl-chain of the enoyl substrate. SAR studies revealed that the 3-carbon alkyl chain (**PT02**) was the best inhibitor of *Yp*FabV, and that either increasing or decreasing the chain length weakened inhibitor potency. For example, the 2-carbon alkyl chain decreased inhibitor scaffold potency by 87-fold (**PT01** vs. **PT02**). Compounds **PT01-05** were high micromolar inhibitors of T276S *Yp*FabV with IC_{50} values greater than 100 µM, revealing that diphenyl ethers are not good inhibitors for this mutant.
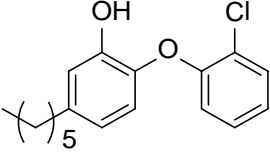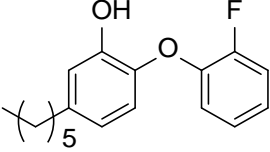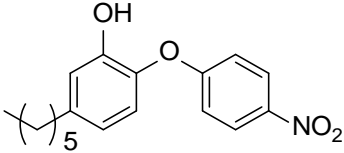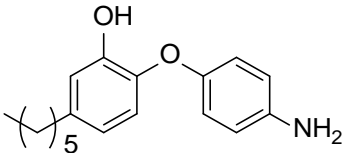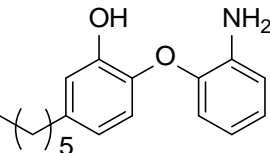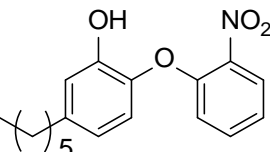
The *ortho*- and *para*- positions on the B-ring were varied to explore interactions between functional groups on the B-ring and *Yp*FabV. Medium and large bulky groups at the *ortho*-position, such as chlorine and nitro (**PT91** and **PT10**), had no significant affect on the binding affinity. However, an electron-withdrawing group with limited steric hindrance, such as a

56

fluorine atom (**PT113**), at the *ortho*-position increased binding 15-fold in comparison to other *ortho* B-ring substituents that contained –Cl, –NH$_2$, and –NO$_2$ (**PT91**, **PT13**, and **PT10**). An electron-withdrawing group at the *para*-position also increased the binding affinity. For example, **PT12** has a *p*-NO$_2$ on its B-ring and it was approximately 17-fold better than **PT15** that has a *p*-NH$_2$. Insertions of a(n) *o*-F group (**PT113**) or *p*-NO$_2$ (**PT12**) on the inhibitor's B-ring also significantly decreased the IC$_{50}$ values for T276S *Yp*FabV to around 5 μM, which is at least 20-fold less than the other tested compounds.

Overall, the best inhibitor for *Yp*FabV was **PT113** with an IC$_{50}$ value of 0.082 ± 0.009 μM. As mentioned above, **PT113** was found to be a potent slow-onset inhibitor against InhA with K_i values of 0.09 ± 0.02 nM (*114*). The slow-onset inhibitor mechanism was not observable with *Yp*FabV (data not shown) and the inhibitor potency decreased by 900-fold for *Yp*FabV.

Table 3.1 Diphenyl ether SAR studies for *Yp*FabV and T276S *Yp*FabV.

Inhibitor	Structure	IC$_{50}$ (µM)	
		[Wt *Yp*FabV] = 15 nM	[T276S *Yp*FabV] = 15 nM
Triclosan		5 ± 1	> 100
Chain Length specificity (at the 5-position)			
PT01		20 ± 3	>100
PT02		0.23 ±0.09	>100
PT03		1.2 ± 0.3	>100
PT04		2.6 ± 0.4	>100
PT05		2.1 ± 0.3	>100
Modification at the *ortho*- and *para*- positions on the B-ring			

PT91		3.8 ± 0.5	>100
PT113		0.082 ± 0.009	8 ± 2
PT12		0.18 ± 0.02	5 ± 1
PT15		3.0 ± 0.4	> 100
PT13		1.8 ± 0.2	45 ± 3
PT10		1.2 ± 0.2	68 ± 14

59

4-Pyridone-based scaffold can promiscuously bind to FabV and FabI ENRs

A diphenyl ether-based scaffold may not be the best inhibitor scaffold because we were able to isolate a variant, T276S *Yp*FabV, from a *Y. pestis* pathogenic strain that lacked diphenyl-ether potency. Since triclosan lost potency for T276S *Yp*FabV compared to wild-type, we speculated T276S *Yp*FabV to be a spontaneous mutation caused by exposure of the pathogenic *Y. pestis* stain to triclosan. In order to find an inhibitor scaffold that can target both wild-type *Yp*FabV and T276S *Yp*FabV which may bypass triclosan resistance, we compared compounds **PT70** (diphenyl ether) (*113*), **PT171** (2-pyridone) (*115*), **PT192** (2-pyridone with bridging oxygen) (*115*), and **PT166** (4-pyridone) (Table 3.2). These scaffolds have an *o*-methyl substituent on the inhibitors' B-ring, and modified A-rings and bridging molecules in comparison to **PT70** (Table 3.2).

The diphenyl ether-based scaffold (**PT70**) inhibited wild-type *Yp*FabV with IC$_{50}$ value of 3 ± 0.5 μM and it was more potent than 2-pyridone (**PT171**) which had an IC$_{50}$ value greater than 50 μM. The inhibitor specificity for T276S *Yp*FabV followed the opposite trend, in which **PT70** inhibited T276S *Yp*FabV with an IC$_{50}$ value greater than 50 μM and **PT171** inhibited T276S *Yp*FabV with IC$_{50}$ value of 6 ± 1 μM. Both wild-type *Yp*FabV and T276S *Yp*FabV, have similar binding preferences for the 4-pyridone-based scaffold (**PT166**) with IC$_{50}$ values ranging between 13 to 23 μM. We expanded our studies to evaluate inhibition of *Bp*FabI and *Bp*FabV with hit compounds that inhibited wild-type *Yp*FabV and/or T276S *Yp*FabV (Table 3.3). The results showed that the diphenyl ether- and 4-pyridone-based scaffolds inhibited *Bp*FabI and *Bp*FabV, while the 2-pyridones were not selective for *Bp*FabV.

60

SAR studies revealed that the diphenyl ethers were a selective inhibitor series for wild-type *Yp*FabV, while the 2-pyridones were a selective inhibitor series for the T276S *Yp*FabV. The best inhibitor scaffold was the 4-pyridones because this scaffold inhibited wild-type *Yp*FabV and T276S *Yp*FabV, along with other ENRs such as *Bp*FabI and *Bp*FabV.

Table 3.2 Inhibitor scaffold preference for *Yp*FabV and its mutant.
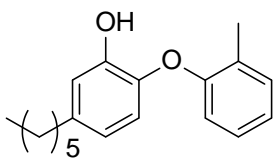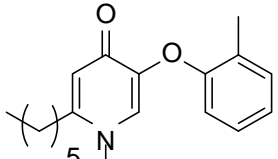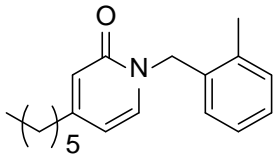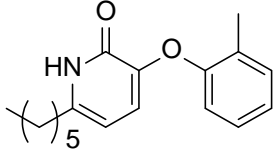
Inhibitor	Structure	IC_{50} (µM) at 15 nM enzyme	
		Wt *Yp*FabV	T276S *Yp*FabV
PT70		3 ± 0.5	> 50
PT166		18 ± 2	23 ± 2
PT171		> 50	6 ± 1
PT192		19 ± 3	> 50

Table 3.3 Enoyl-ACP reductase SAR studies with lead compounds
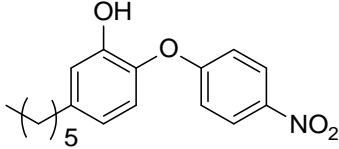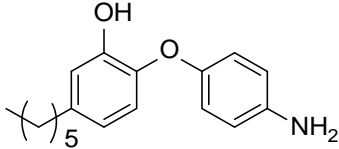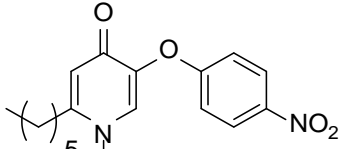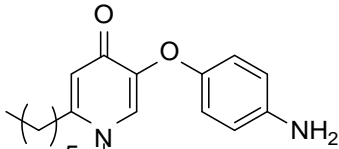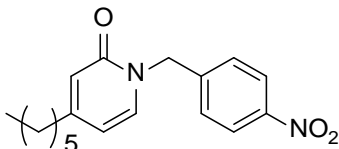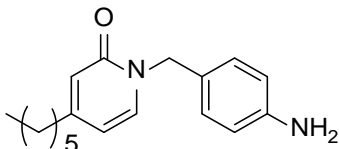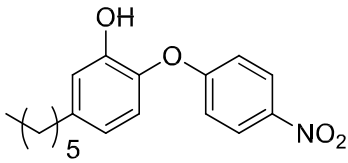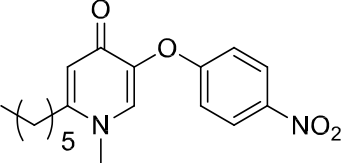
Inhibitor	IC$_{50}$ (μM)			
	Wt *Yp*FabV (15 nM)	T276S *Yp*FabV (15 nM)	*Bp*FabV (7.5 nM)	*Bp*FabI (30 nM)
PT12	0.18 ± 0.02	5 ± 1	0.28 ± 0.09	0.71 ± 0.1
PT15	3 ± 0.4	> 50	3 ± 0.6	0.25 ± 0.05
PT156	0.18 ± 0.04	1.0 ± 0.08	0.56 ± 0.1	0.96 ± 0.1
PT157	0.13 ± 0.03	0.29 ± 0.06	1 ± 0.3	0.87 ± 0.9
PT424	21 ± 7	3 ± 0.3	> 50	28 ± 5
PT425	30 ± 5	6 ± 1	> 50	4 ± 0.8
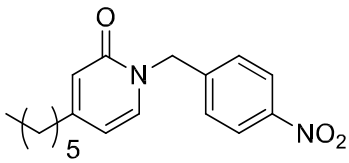
Table 3.4 Mode of inhibition comparison with PT12 (diphenyl ether-based scaffold), PT156 (4-pyridone-based scaffold), and PT424 (2-pyridone-based scaffold).

Enzyme	K_i (µM)			Mode of Inhibition		
	PT12	PT156	PT424	PT12	PT156	PT424
Wt *Yp*FabV	0.14 ± 0.01	0.15 ± 0.03	11 ± 2	U	C	N
T276S *Yp*FabV	6 ± 1	0.50 ± 0.05	4 ± 0.8	N	C	N
*Bp*FabV	0.18 ± 0.005	0.26 ± 0.05	ND	N	C	ND
*Bp*FabI	0.36 ± 0.06	0.48 ± 0.06	ND	C	C	ND

N= noncompetitive; U=uncompetitive; C=competitive
ND=Not Determined

Inhibitor cofactor preference and substrate binding mechanism may alter inhibitor specificity and mode of inhibition

SAR studies provided insights about the inhibitor preference for the FabV enzyme. However, little is known about the mode of inhibition for inhibitors that target *Yp*FabV and

T276S *Yp*FabV, which is essential for further inhibitor optimization. Therefore, compounds **PT12** (diphenyl ether-based scaffold), **PT156** (4-pyridone-based scaffold), and **PT424** (2-pyridone-based scaffold) were selected to explore the mode of inhibition of the three different scaffolds to wild-type *Yp*FabV and T276S *Yp*FabV. The three compounds displayed different binding mechanisms to wild-type *Yp*FabV: uncompetitive (**PT12**), noncompetitive (**PT424**), and competitive (**PT156**) with respect to ddCoA (Table 3.4/Figure 3.2.A-C). Analysis of **PT156** and **PT424** yielded the same results for T276S *Yp*FabV, whereas the binding mechanism of the diphenyl ether (**PT12**) changed from uncompetitive to a noncompetitive mechanism with respect to ddCoA (Table 3.4/Figure 3.2.D-F). Scheme 3.2 (random bi-bi mechanism; wild-type *Yp*FabV) and Scheme 3.3 (ordered bi-bi mechanism; T276S *Yp*FabV) depict the enzyme reaction along with the formation and breakdown of different inhibitor-enzyme complexes.

Thermal shift assays were used to validate the inhibitors' effect on ternary complex formation. The stability of each enzyme in the presence of the inhibitor and NAD^+ or NADH was determined by a shift in the midpoint temperature of the protein-unfolding transition (T_m) (Figure 3.3). In the case of wild-type *Yp*FabV, it is thermodynamically unfavorable for the diphenyl ether-based scaffold **PT12** to solely bind to wild-type *Yp*FabV (Figure 3.3.A). In addition, there were no statistically significant shifts in the T_m between the presence and the removal of inhibitor with the enzyme-NADH (E-NADH) or -NAD^+ (E-NAD^+) complexes. However, combining the analysis of the thermal shift assays with steady-state kinetics, **PT12** will bind only to the wild-type *Yp*FabV-NAD^+ complex since it follows an uncompetitive mechanism with a K_i value of 0.14 ± 0.01 μM (Table 3.4/Figure 3.2.A-C). With regards to T276S

*Yp*FabV, thermal shift assays reveal that **PT12** can bind to the E-NAD$^+$ complex and the free enzyme, but not the E-NADH complex (Figure 1B). This information supports steady-state kinetic analysis, in which **PT12** is a noncompetitive inhibitor of T276S *Yp*FabV with a K_i value of 6 ± 1 μM (Table 3.4/Figure 3.2.D-F).

The mode of inhibition for **PT12** was tested with *Bp*FabV and it was the same as T276S *Yp*FabV (Table 3.4/Figure 3.4.A). The change in mode of inhibition of **PT12** for both enzymes in comparison to wild-type *Yp*FabV may be affected by the substrate binding mechanism since T276S *Yp*FabV and *Bp*FabV catalyzes substrate reduction via an ordered bi-bi mechanism, while wild-type *Yp*FabV utilizes a random bi-bi (Chapter 2). However, the K_i value for **PT12** for *Bp*FabV was 0.18 ± 0.005 μM (Table 3.4), which was comparable to the inhibition constant for wild-type *Yp*FabV. This observation is presumably because both enzymes contain a conserved threonine residue at position 275/276.

A different mode of inhibition for **PT12** was also observed with *Bp*FabI in comparison to other tested enzymes (Table 3.4/Figure 3.4.C), which implies that the binding mechanism may have changed due to other preferential interactions between the FabI enzyme, inhibitor, and cofactor that may not be applicable in the FabV system. **PT12** was found to be a rapid reversible, competitive inhibitor with respect to ddCoA for *Bp*FabI and it had a two-fold lower inhibition constant in comparison to *Bp*FabV.

As for the 2-pyridone-based scaffold (**PT424**), the same mode of inhibition with *Yp*FabV and T276S FabV was observed with only a two-fold difference in the K_i (Table 3.4). The

insignificant difference in binding affinity was unexpected based on SAR data, which showed a potential inhibitor preference of the 2-pyridone-based scaffold with T276S *Yp*FabV over wild-type *Yp*FabV (Table 3.3). The inhibitor potency for wild-type *Yp*FabV may due to favorable interactions between substituent groups on the inhibitor's B-ring and the enzyme. This hypothesis coincides with findings by Hirschbeck *et al* (*42*), in which an extensive hydrogen-bonding network between 2-pyridones with different substituents on the B-ring and T276S *Yp*FabV was found to facilitate reorganization of water molecules and its cofactor NADH.

PT424 was a noncompetitive inhibitor with respect to ddCoA for wild-type *Yp*FabV and T276S *Yp*FabV (Table 3.4/Figure 3.2.C and 3.2.E). Thermal shift assays coincided with the kinetic results (Figure 3.3.A), in which it is possible that the 2-pyridone may bind to the E-NADH and E-NAD$^+$ complexes. In contrast, the addition of **PT424** increased the T_m of the T276S *Yp*FabV-NADH complex by 0.5 ± 0.1 °C, and there was no evidence for binding to T276S *Yp*FabV and the T276S *Yp*FabV-NAD$^+$ complex. This suggests that the 2-pyridone series gains specificity to bind to the E-NADH complex, which is not apparent for wild-type *Yp*FabV (Figure 3.3.B). 2-Pyridones were poor inhibitors of *Bp*FabV and *Bp*FabI, so we did not evaluate the modes of inhibition of **PT424** with these enzymes.

The mode of inhibition for **PT156** was competitive with respect to ddCoA for wild-type and T276S *Yp*FabV, which was expected to be similar based on SAR data (Table 3.4/Figure 3.2.B). **PT156** displayed the most favorable binding affinity to both enzymes compared to the other selected compounds. This compound preferred binding to the E-NADH ternary complex,

which was supported by thermal shift assays where the inhibitor increased the T_m of the E-NADH ternary complex for wild-type and T276S YpFabV by 0.6 ± 0.1 °C and 0.6 ± 0.08 °C, respectively (Figure 3.3). Likewise, the mode of inhibition of **PT156** to BpFabV and BpFabI was competitive with respect to ddCoA (Table 3.4/Figure 3.4.B).

Wild-type _Yp_FabV   **T276 _Yp_FabV**
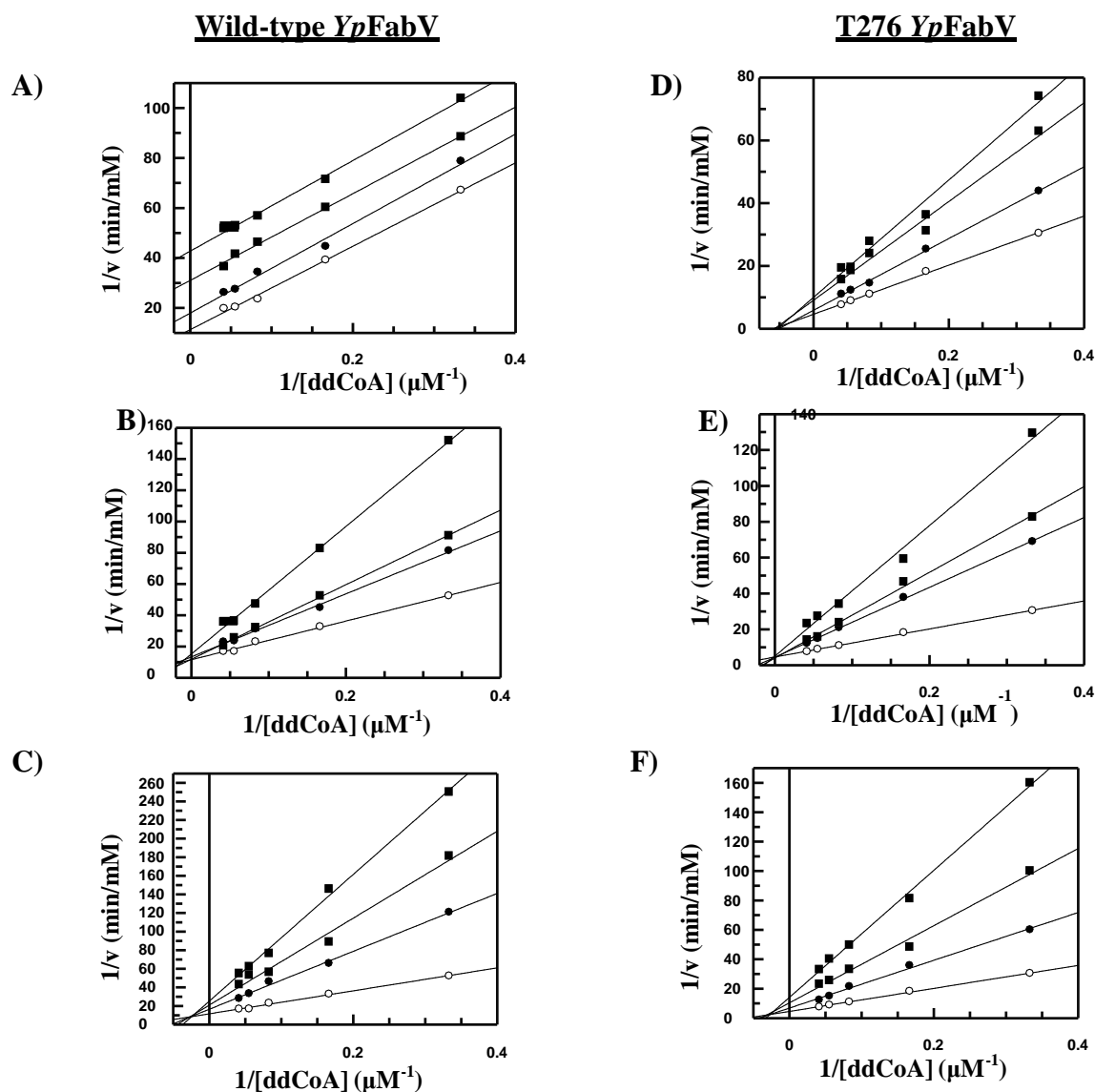
Figure 3.2 Steady-state kinetic analyses of wild-type _Yp_FabV and T276S _Yp_FabV
Inhibition was evaluated with wild-type _Yp_FabV at (A) (○) 0 nM PT12, (•) 100 nM PT12, (□)
200 nM PT12, (■) and 400 nM PT12; (B) (○) 0 nM PT156, (•) 100 nM PT156, (□) 200 nM
PT156, (■) and 400 nM PT156; and (C) (○) 0 μM PT424, (•) 10 μM PT424, (□) 20 μM
PT424, (■) 30 μM PT424. Inhibition was evaluated with wild-type _Yp_FabV at (D) (○) 0 μM
PT12, (•) 1 μM PT12, (□) 5 μM PT12, and (■) 10 μM PT12; (E) (○) 0 μM PT424, (•) 0.5 μM
PT424, (□) 1 μM PT424, and (■) 2 μM PT424; and (F) (○) 0 μM PT424, (•) 1 μM PT424, (□)
5 μM PT424, and (■) 10 μM PT424.
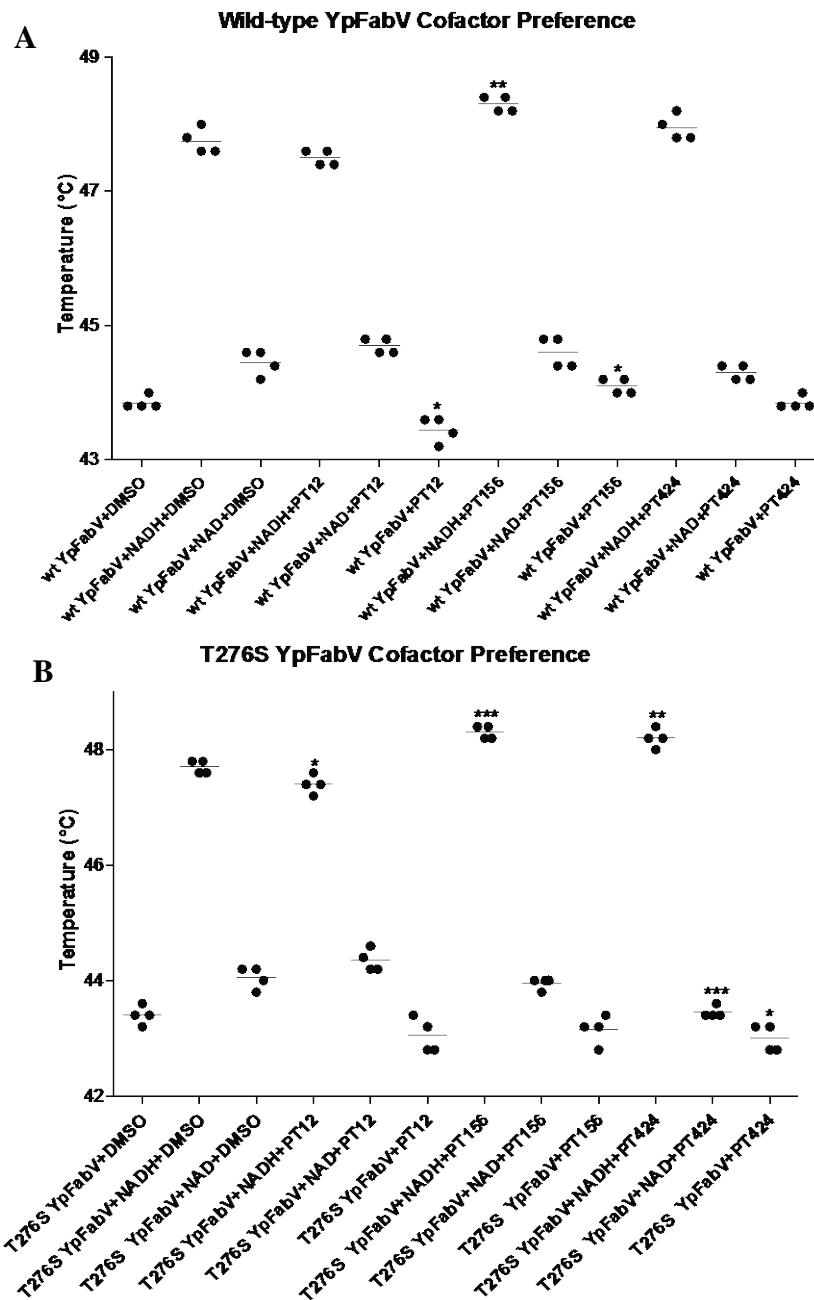
Figure 3.3 Midpoint temperatures of the protein-unfolding transition (T_m)
for (A) Wild-type YpFabV and (B) T276S YpFabV in the presence of inhibitor (25 μM) and
NADH or NAD+ (2.5 mM). Significance was determined by an unpaired t-test analysis between
untreated and treated groups.

69

A)

C)

B)

D)
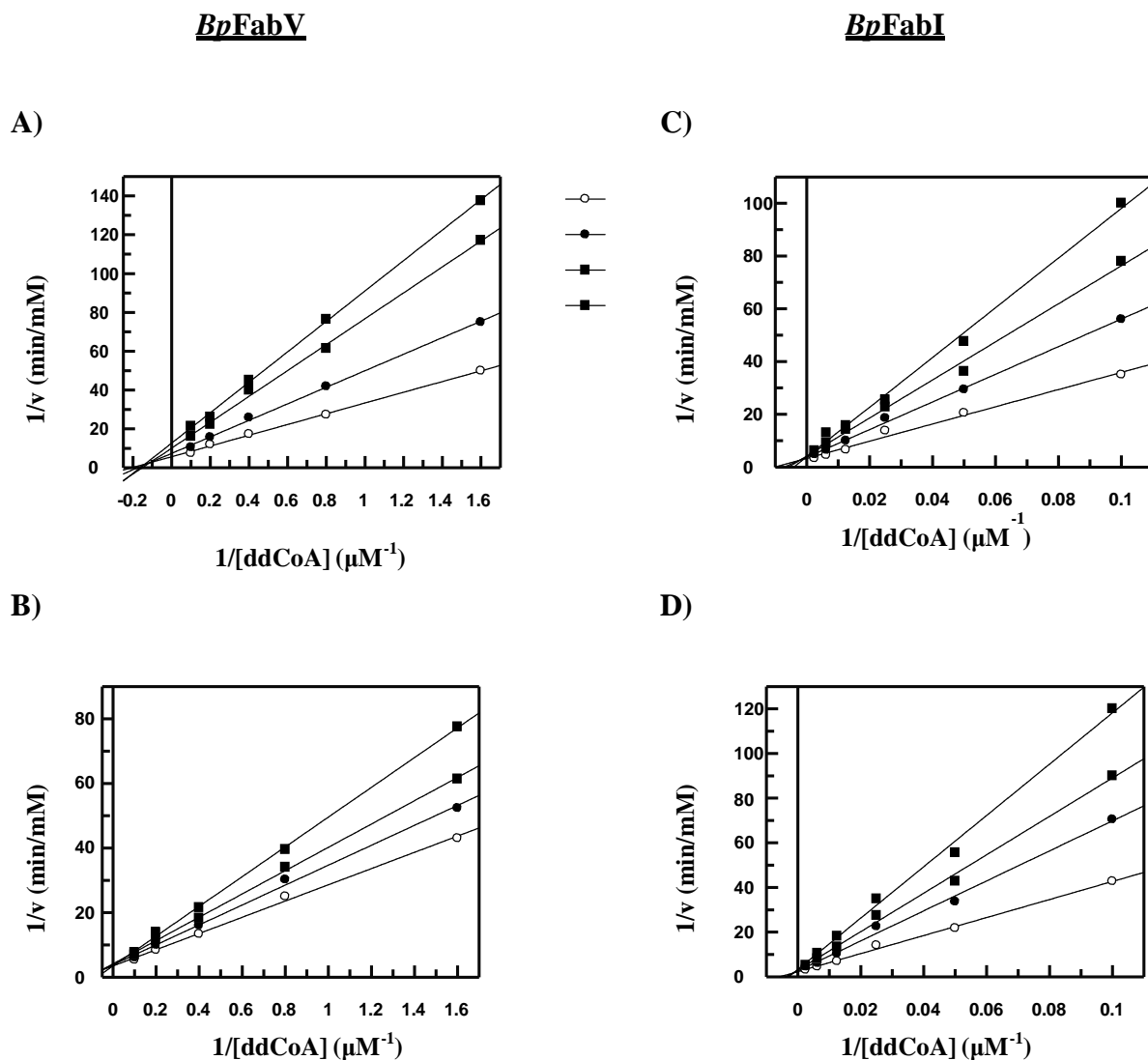
Figure 3.4 Steady-state kinetic analyses of *Bp*FabV and *Bp*FabI.
Inhibition was evaluated against *Bp*FabV at (A) (O) 0 nM PT12, (•) 100 nM PT12, (□) 200 nM PT12, and (■) 400 nM PT12; and (B) (O) 0 nM PT156, (•) 250 nM PT156, (□) 500 nM PT156, and (■) 1000 nM PT156. Inhibition was evaluated against *Bp*FabI by Ms. Weixuan Yu at (C) (O) 0 nM PT12, (•) 400 nM PT12, (□) 800 nM PT12, and (■) 1600 nM PT12; and (D) (O) 0 nM PT156, (•) 400 nM PT156, (□) 800 nM PT156, and (■) 1600 nM PT156.

Discussion

SAR studies of wild-type *Yp*FabV and T276S *Yp*FabV with diphenyl ether-based inhibitors were conducted (Table 3.1). These compounds are triclosan analogues that target the ENR FabI and generally bind to the E-NAD+ complex (*111-114*). Most of the selected diphenyl ether compounds were low micromolar inhibitors of wild-type *Yp*FabV, while the majority of the diphenyl ethers were poor, high micromolar inhibitors of T276S *Yp*FabV. This trend suggests that the T276 methyl group may have favorable hydrophobic interactions within the active site that can influence the binding of the inhibitor. The lack of inhibitor potency to the mutant can be circumvented by additional favorable interactions between substituents on the inhibitor's B-ring and its respective enzyme, which was also consistent for the wild-type enzyme (Table 3.3). However, a diphenyl ether-based scaffold would not be a promising lead scaffold because we isolated T276S *Yp*FabV variant from a pathogenic strain that was speculated to be a single nucleotide point mutation caused by exposure of *Y. pestis* to triclosan.

The lack of inhibitor potency of diphenyl ethers to T276S *Yp*FabV led to the expansion of the SAR studies to 2- and 4-pyridone-based inhibitors (Table 3.2). These scaffolds were shown to have activity against other ENRs. For example, the 2-pyridone inhibitor CG400549 was shown to target *S. aureus* FabI (*72*) and is currently in Phase II clinical trials. Likewise, 4-pyridones were shown to inhibit FabI homologues from *E. coli* (*71*), *St. pneumoniae (73)* and *S. aureus (70, 71)*, along with FabK from *St. pneumoniae (73)*. We found that 2-pyridones inhibited T276S *Yp*FabV with IC_{50} values around 5 μM, while it not specific for the wild-type *Yp*FabV with IC_{50} values greater than 50 μM. It is possible that the 2-pyridone-scaffold may prefer a more hydrophilic surrounding environment within the active site of T276S *Yp*FabV, which could be provided by additive hydrogen bonding interactions between the pyrophosphate of NADH,

71

ordered water molecules, and the enzyme (Chapter 2). This hypothesis also coincides with the difference of ClogP values of inhibitor scaffolds. For instance, T276S *Yp*FabV lacked inhibitor preference with **PT12**, which has a ClogP value of 6.21, yet this mutant exhibited inhibitor specificity with **PT424**, which has a lower ClogP value of 4.57.

The 4-pyridone-based scaffold was the most promising inhibitor scaffold because wild-type *Yp*FabV and T276S *Yp*FabV exhibited comparable inhibition constants. For example, **PT156** inhibited wild-type *Yp*FabV and T276S *Yp*FabV with K_i values of 0.15 ± 0.03 μM and 0.50 ± 0.05 μM, respectively. The inhibition specificity of the 4-pyridone-based scaffold across the tested enzymes (Table 3.3) can be most likely explained due to its resemblance to the enoyl substrate in comparison to the other inhibitor scaffolds.

Given that wild-type *Yp*FabV is known to catalyze substrate reduction via a random bi-bi mechanism while T276S *Yp*FabV utilizes an ordered bi-bi mechanism (Chapter 2), the mode of inhibition may vary between scaffolds and enzymes. If the order of substrate binding affects the mode of inhibition, then ENR inhibitor design can be inherently challenging and dependent on the favorable interactions between the inhibitor, enzyme, NADH and/or NAD^+. Scheme 3.1 and 3.2 represent the formation and breakdown of inhibitor complexes, and each representative inhibitor scaffold differed among the tested enzymes with different substrate binding mechanisms. Based on the steady-state kinetic data, the diphenyl ether, **PT12,** binds only to the E-NAD^+ ternary complex (Scheme 3.1). However, removal of the methyl group allows the inhibitor to bind to other enzyme complexes (Scheme 3.2).
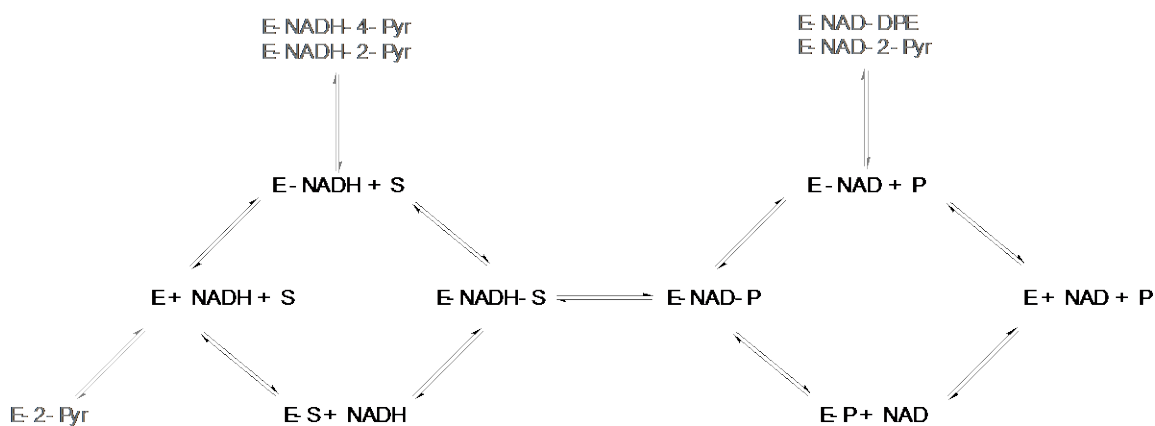
Scheme 3.1 Formation and breakdown of inhibitor scaffold complexes for wild-type
*Yp*FabV.
E= free enzyme; S=substrate; P=product; DPE= diphenyl ether-based inhibitor; 4-Pyr= 4-pyridone-based inhibitor; 2-Pyr= 2-pyridone-based inhibitor.
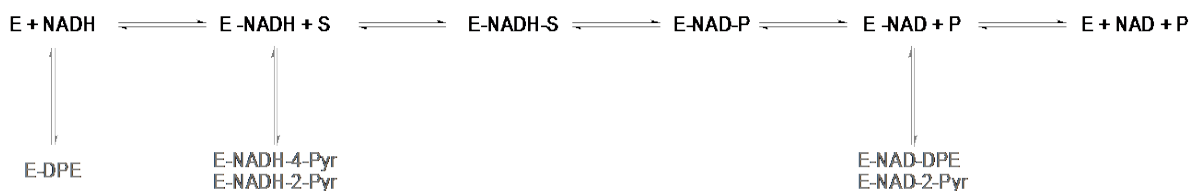
Scheme 3.2 Formation and breakdown of different inhibitor scaffold complexes for T276S
*Yp*FabV.
E= free enzyme; S=substrate; P=product; DPE= diphenyl ether-based inhibitor; 4-Pyr= 4-pyridone-based inhibitor; 2-Pyr= 2-pyridone-based inhibitor.

The mode of inhibition may be affected by the substrate binding mechanism and cofactor binding preferences. The diphenyl ether-, 2-pyridone-, and 4-pyridone- scaffolds exhibited different modes of inhibition for *Yp*FabV based on their cofactor preference. The mode of inhibition for the diphenyl ether-based scaffold differed for *Yp*FabV and T276S *Yp*FabV, whilst the mode was the same for T276S *Yp*FabV and *Bp*FabV. Data suggest that the diphenyl ether-scaffold may be more directly affected by the substrate binding mechanism compared to the other scaffolds. T276S *Yp*FabV and *Bp*FabV catalyze substrate reduction via an ordered bi-bi

73

mechanism (Chapter 2) and they displayed the same mode of inhibition for **PT12**. More importantly, *Yp*FabV and *Bp*FabV display the same inhibitor scaffold specificity as expected since the threonine residue is conserved at the 276/275 position.

Also, additional interactions may influence the inhibitor's mode of inhibition, which was revealed through inhibition against *Bp*FabI (Table 3.4). It is not unusual to switch the mode of inhibition by inhibitor substituent modifications or mutations of the enzyme target. For instance, different substituents on the B-ring of the diphenyl ether-based scaffold were shown to have noncompetitive or uncompetitive mechanisms for *E. coli* FabI, whereas *M. tuberculosis* InhA mutants, Y158F and M161V, changed the mode of inhibition of triclosan from uncompetitive to noncompetitive (*89, 116*).

In conclusion, the data suggests that future SAR studies should focus on the 4-pyridones because the binding mechanism was consistent across all enzymes tested. 4-Pyridones is a selective inhibitor for ENR classes, which addresses one challenge in the optimization of kinetic and thermodynamic properties. This study shows that an inhibitor's scaffold and substituents as well as enzyme mutations and cofactor preference can alter the mode of inhibition.

Chapter 4: MUT056399 and *p*-Fluoro Diphenyl Ethers: Detailed Kinetic Analysis on the Slow Binding Inhibition of Enoyl-ACP Reductase FabI from *Burkholderia pseudomallei*

Background

Melioidosis (Whitmore's Disease)

Melioidosis is a severe disease that predominantly afflicts Southeast Asia and Northern Australia (*117*). Individuals diagnosed with this disease would often have one or more pre-existing condition(s) correlated with an altered immune response. One of the most severe manifestations of this disease is melioidosis septic shock, which is often associated with pneumonia and bacterial dissemination to distant sites (*117*).

The Gram-negative soil-dwelling organism *Burkholderia pseudomallei* is the causative agent of melioidosis. Patients infected with *B. pseudomallei* are usually treated with a 20-week minimum regimen that is divided into an intravenous and oral phase. In the initial phase, intravenous therapy of first-line therapeutics, ceftazidime or carbapenem antibiotics, or second-line therapeutics, beta-lactamase inhibitor combination such as amoxicillin-clavulanate, are given within the first 2 to 6 weeks. During the oral phase of therapy, a combination of trimethoprim-sulfamethoxazole, doxycycline and potentially chloramphenicol are given for the next 3 to 6 months. Whilst *B. pseudomallei* is susceptible to this treatment, mortality is high because relapse often occurs (*118*).

75

In northeast Thailand, 20% of all community-acquired septicaemias and 40% of sepsis-related mortality is due to *B. pseudomallei* infections, in which the choice of antibiotic regimen has not been shown to impact mortality within the first 48 hours of admission (*117, 119, 120*). Additionally, *B. pseudomallei* is naturally resistant to many antibiotics including penicillin, first- and second-generation cephalosporins, macrolides, rifamycins, colistin, and aminoglycosides. Intrinsic multidrug resistance may be due to efflux pumps, which are transport proteins that remove toxic substrates including antibiotics from within the cell to the external environment (*121*). The efflux systems of resistance-nodulation-division (RND) family, AmrAB-OprA and BpeAB-OprB, in *B. pseudomallei* have been associated to the efflux of aminoglycosides and macrolides (*122, 123*). Other drug resistant mechanisms are (1) its cell wall acts as an immunodominant antigen or (2) it produces a hydrated polysaccharide capsule that helps form microcolonies and resists antibiotic penetration (*124, 125*).

The ability to treat *B. pseudomallei* infections has become more pertinent in the recent years because this pathogen can be used in biological warfare. Biological weapons research using *B. pseudomallei* dates back to the former Soviet Union, and unfortunately the magnitude of this research and the likelihood of engineered antibiotic resistant strains are unknown (*81, 119*). Also, other countries, such as the United States and Egypt, have previously shown a military interest in this pathogen (*119*). Present day, *B. pseudomallei* is classified as a Tier 1 Biological Select Agent or Toxin (BSAT) by the Centers for Disease Control and Prevention (CDC). Tier 1 agents pose a threat for large-scale dissemination with deliberate misuse, and potential harm to

public health (*118, 126*). Therefore, there is need to develop chemotherapeutics that can be used to treat *B. pseudomallei* infections.

Targeting the FabI ENR from B. pseudomallei

Metabolic precursors for the bacterial phospholipid membrane are synthesized via fatty acid biosynthesis (FAS), and these precursors are essential for bacterial survival. In addition, due to the low sequence homology and fundamental structural differences of the mammalian FAS system (FAS-I) and bacterial FAS system (FAS-II), the FAS-II pathway is thought to be an attractive antimicrobial target (*58, 91*). In the FAS-II pathway, the enoyl-ACP reductase (ENR) is inferred to be essential for *E. coli* viability, as well as a key regulator of fatty acid biosynthesis (*48*). Thus, the ENR can be a promising drug target.

While the FabI and FabV ENR subtypes coexist in *B. pseudomallei*, studies by Liu *et al* demonstrated that the FabI ENR from *B. pseudomallei* was a suitable drug target (*94*). In these studies, three diphenyl ethers that are analogues of a broad-spectrum inhibitor, triclosan (Figure 4.1.A), were shown to be potent slow-onset inhibitors with binding constants (K_i) ranging between 0.5-2 nM. In addition, these compounds showed a reduction in MIC values in *B. pseudomallei* efflux pump mutant strains (*94*).
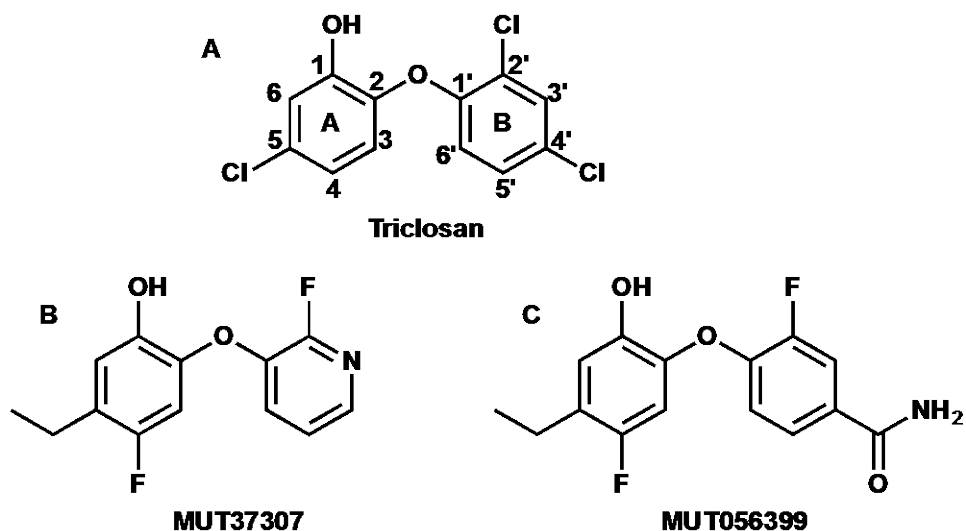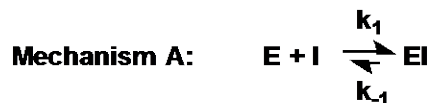
Figure 4.1 FabI inhibitors and possible kinetic mechanisms of slow binding inhibition.
The three possible mechanisms (A, B and C) for slow-binding inhibition are depicted. In addition, MUT37307 (B) and MUT056399 (C) are potent FabI analogs of the broad-spectrum inhibitor Triclosan (A).

Slow Binding Inhibition

Early phase drug discovery focuses on *in vitro* thermodynamic parameters of compound potency, such as the equilibrium dissociation constant (K_d), the inhibition dissociation constant

78

(K_i) and half maximal inhibitory concentration (IC_{50}). However, thermodynamic parameters may be less applicable *in vivo* because drug concentrations are not constant and thermodynamic parameters cannot completely predict target occupancy (*127, 128*). Therefore, both thermodynamic and kinetic parameters should be used to fully understand target engagement and better predict *in vivo* efficacy and selectivity. The kinetic lifetime of a drug-target complex can be described by the dissociation rate constant (k_{off}), residence time ($1/k_{off}$) or dissociative half-life ($0.693/k_{off}$), (*127, 129, 130*).

The formation and breakdown rates of a drug-target complex can be slow leading to residence times of minutes, hours or even days (*129, 131*). There are three possible mechanisms for slow binding inhibition of enzymatic reactions: (1) one-step binding mechanism (Figure 4.1, Mechanism A), (2) an induced-fit, two-step model (Mechanism B), and (3) conformational selection, two-step model (Mechanism C). In the one-step binding mechanism process, the inhibitor can bind to the enzyme to form the binary complex (EI), in which the rate of ligand association (k_{on}) and k_{off} values equal to k_1 and k_{-1} (*127, 129*).

In the induced-fit, two-step model, the inhibitor initially binds to the enzyme in a conformational state (E) that is not optimal for enzyme-inhibitor interactions. Subsequently, the initial enzyme-inhibitor complex (EI) isomerizes to a new state (EI*) in which enzyme-inhibitor interactions are maximized. The affinity for the initial complex is given by K_d, (k_{-1}/k_1) while the affinity of the inhibitor for the final complex is given by K_d*, ($k_{-1}/(k_1 + k_1 k_2/k_{-2})$) (*127, 129*).

79

In the conformational selection, two-step model, the enzyme is in equilibrium between two conformational states (E and E*) and only one conformation (E*) is able to bind the inhibitor. As the concentration of inhibitor increases, the population of the free E* state decreases to form the binary complex (E*I). The interconversion between the two enzyme states is slow relative to the binding of the inhibitor to the E* state. In this mechanism, the affinity of the inhibitor for the initial final complex (K_d*) is given by k_{-2}/k_2 (*127, 129*). Although conformational selection is possible, the most common slow binding mechanisms are the one-step and two-step induced-fit models.

MUT056399 and p-Fluoro Diphenyl Ethers

Mutabilis FabI inhibitor, MUT37307, (Figure 4.1.B) is a diphenyl ether that targets the FabI ENR (*132*). The addition of a *p*-fluoro group in the Gerusz *et al* compound series led to a small improvement of enzymatic potency by a 2-fold decrease in the IC_{50} value against *S. aureus* FabI (*133*). Further optimization led to a second-generation inhibitor (MUT056399) (Figure 4.1.C), which is a potent antistaphylococcal clinical candidate (*133, 134*). Translation of MUT056399 inhibitory activity to other FabI enzymes, such as *Bp*FabI, would help determine if this compound can be used to treat other bacterial infections. Also, SAR studies will shed light on the significance of the *p*-fluorine introduction on diphenyl ethers' kinetic and thermodynamic properties.

80

Project Goals

There is a growing interest in developing chemotherapeutics that can be used to treat *B. pseudomallei* infections because of limitations of current treatment, high mortality and relapse, and threat of biological warfare. Therefore, we performed SAR studies with MUT056399 and other *p*-fluoro diphenyl ethers to identify structural features that were favorable for inhibition of *Bp*FabI. We optimized kinetic and thermodynamic properties to determine their effects on the transition and ground states of the enzyme-inhibitor binary complexes in order to propose additional analogs. In addition, the antibacterial activity of the lead *Bp*FabI inhibitor was evaluated in an acute *B. pseudomallei* mouse model of infection.

Materials and Methods

Materials

Luria broth was purchased from VWR and His-bind Ni^{2+}-NTA resin was purchased from Invitrogen. Crotonyl coenzyme A (crot-CoA) was purchased from Sigma-Aldrich and *trans*-2-octenoic acid was purchased from TCI. MUT056399 was a gift from Anacor Pharmaceuticals. All other chemical reagents were obtained from Fisher. Curve fitting was performed using KaleidaGraph Version 4.1.

Expression and purification of BpFabI

The FabI enoyl-ACP reductase from *Burkholderia pseudomallei* was cloned, expressed, and purified as previously reported (*94*). Briefly, Dr. Nina Liu cloned the *fabI* gene from *Burkholderia mallei* ATCC 23344 which is 100% identical to the *fabI* gene from *Burkholderia pseudomallei*. The PCR product was digested with NdeI and BamHI, and ligated into pET15b plasmid (Novagen), in which the hexa-histidine tag was encoded at the N-terminus of the protein sequence. Protein expression was performed using the *E. coli* BL21(DE3) pLysS cells in Luria Broth containing 0.2 mg/mL ampicillin. The cell culture was incubated at 37 °C and induced at OD_{600} of 1.0 with 1 mM isopropyl-1-thio-β-D-galactopyranoside (IPTG). Cells were incubated for an additional 16 h at 25 °C and harvested by centrifugation at 5000 rpm for 20 min at 4 °C. After the cell lysis by sonication, *Bp*FabI was purified using His affinity chromatography. The protein purity was verified by 15% SDS–PAGE, which gave an apparent molecular weight of ~28 kDa. The concentration of *Bp*FabI was spectrophotometrically determined, using an extinction coefficient of 13, 490 M^{-1} cm^{-1}. This value was calculated from the primary sequence of the protein using ExPASy ProtParam tool.

Synthesis of substrates and compounds

The substrate *trans*-2-octenoyl-CoA (oct-CoA) was synthesized from *trans*-2-octenoic acid using the mixed anhydride method (*89*) as previously described. Dr. Gopal R. Bommineni synthesized all inhibitors in this study.

Thermal shift assay

ThermoFluor experiments were performed as previously described in Chapter 3 to determine inhibitor cofactor preference (*135*). Briefly, 7.4 μM enzyme, 2.5 mM cofactor (NADH or NAD^+) and 25 μM inhibitor (2% DMSO) were added to a 96-well thin-wall PCR plate (Concord) containing a buffer solution of 30 mM PIPES, 150 mM NaCl and 1.0 mM EDTA at pH 8.0. After 1.5 h incubation at 25 °C, 1 μL of 100 × Sypro Orange (Sigma) was added to each well and the plate was sealed with Microseal 'B' Film (Bio-Rad). The samples were heated from 25 to 90 °C in increments of 0.2 °C/10 s. Bio-Rad CFX Manager was used to process the data.

Preincubation inhibition assay

Preincubation inhibition assays were performed as previously described using a Cary 100 Bio (Varian) spectrophotometer at 25 °C in glycerol (8% *v/v*), bovine serum albumin (0.1 mg/mL), 30 mM PIPES, 150 mM NaCl, and 1.0 mM EDTA, at pH 8.0 (*136*). Assays were performed to determine the apparent inhibition constants for slow binding inhibitors. *Bp*FabI (30 nM) was preincubated with fixed concentrations of DMSO (2% *v/v*), NAD^+ (10-200 μM), NADH (250 μM), and inhibitor (0-1000 nM) for 16 h at 4°C. The reaction mixture was warmed to room temperature, and initiated by the addition of oct-CoA (30 μM). The apparent inhibition

constant K_i' was determined using Equation 4.1, in which v and v_o are the initial velocities in the presence and absence of inhibitor, and [I] is the inhibitor concentration.

$$v = \frac{v_o}{1 + \frac{[I]}{K_i'}}$$

Equation 4.1

The K_i' values obtained at different NAD^+ concentrations were then fitted to Equation 4.2 to describe the binding of the inhibitor to E-NAD^+ (K_1).

$$K_i' = K_1(1 + \frac{K_{m,NAD}}{[NAD]})$$

Equation 4.2

Progress curve analysis

Slow-onset inhibition kinetics were monitored at 340 nM on a Cary 100 spectrophotometer (Varian) at 25 °C. The reactions were initiated by the addition of enzyme (2 nM) to a mixture containing glycerol (8% *v/v*), bovine serum albumin (0.1 mg/mL), DMSO (2% *v/v*), crot-CoA (750 μM), NADH (250 μM), NAD^+ (200 μM) and inhibitor (0-500 nM). All reactions were monitored until steady-state was reached, which was indicated by linearity of the progress curve. Moreover, low enzyme and high substrate concentrations ensured substrate depletion would not significantly affect the reaction rates, such that in the absence of inhibitor the progress curves were linear for over a period of 30 min (*93, 135, 137*). Data were analyzed as previously described (*41, 136*) and fitted to the Morrison & Walsh integrated rate equation (Equation 4.3), where; A_t and A_0 are the absorbance at time t and 0; v_i and v_s are the initial and

84

steady-state velocities; and k_{obs} is the observed pseudo-first rate order constant for the approach to steady-state.

$$A_t = A_0 - v_s t - (v_i - v_s) * \frac{1 - e^{-k_{obs}t}}{k_{obs}}$$

Equation 4.3

The plot of fractional steady-state velocities as a function of inhibitor concentration was fit to the isotherm equation (Equation 4.4) to determine the K_i', such that the values corresponded to the steady-state inhibition IC_{50}. The parameters v_s, v_c, and [I] represent the steady-state velocity, the uninhibited reaction velocity, and the inhibitor concentration.

$$\frac{v_s}{v_c} = \frac{1}{1 + \frac{[I]}{K_i'}}$$

Equation 4.4

The dissociation rate of the inhibitor, k_{-1}, was calculated from each progress curve using Equation 4.5.

$$k_{-1} = k_{obs} * \frac{v_s}{v_i}$$

Equation 4.5

The association rate of the inhibitor, k_1, was calculated from each progress curve using Equation 4.6.

$$k_1 = \frac{k_{-1}}{K_i'}$$

<div align="right">**Equation 4.6**</div>

Equation 4.7 was used to calculate the inhibition constant, K_i.

$$K_i = \frac{k_{-1}}{k_1}$$

<div align="right">**Equation 4.7**</div>

Direct dissociation assay

Using ^{32}P-NAD$^+$, the direct dissociation rate (k_{off}) was determined by Ms. Weixuan Yu. Briefly, a mixture of 15 μM bpFabI, 20 μM NAD$^+$, ^{32}P-NAD$^+$ (800 Ci/mmol) and 200 μM inhibitor was preincubated at 4 °C overnight in the reaction buffer containing 30 mM PIPES, 150 mM NaCl and 1.0 mM EDTA at pH 8.0. Excess free ligand was removed by gel filtration and the 500 μL reaction mixture was diluted into 60 mL reaction buffer to initiate inhibitor dissociation. 600 μL aliquots from the diluted mixture were withdrawn at different time points, followed by an immediate ultracentrifugation at 13,400 rpm for 90 s. The radioactivity in the flow-through was quantified by LS5801 scintillation counter. Data were fitted to Equation 4.8.

$$C(t) = C(0) + C_{max} * (1 - e^{-k_{off}t})$$

<div align="right">**Equation 4.8**</div>

Minimum inhibitory concentration determination

Dr. Jason Cummings from Colorado State University performed MIC determinations. *B. pseudomallei* 1026b (efflux-proficient) and *B. pseudomallei* Bp400 (1026b Δ[*bpeAB-oprB*] Δ[*amrAB-oprA*]) were grown to an OD$_{600}$ of ~0.6, frozen at -80 °C in 10% glycerol and were

used as standard bacterial stocks for these studies. For each evaluation bacteria were prepared fresh by growth from the standard stocks on Luria-Bertani (LB) Agar, Miller (BD) grown at 37 °C for 48-72 h. Bacteria recovered from the LB plates were used to inoculate 10 mL LB Broth. Broth cultures were then incubated for 18 h at 37 °C passed 1:100 and incubated for an additional 6 h at 37 °C. Bacteria were then diluted to a concentration of 1×10^6 colony forming units (CFU)/mL in cation-adjusted Mueller-Hinton broth (CAMHB; BD, Franklin Lakes, NJ) and 50 μL added to each well for each test plate. For MIC determination, compounds were added to a 96-well plate starting at 256 μg/mL in the first column and serially diluted 1:2 to column 12 for a final concentration of 0.125 in CAMHB. MIC plates were incubated at 37 °C for 18 h at which time MIC was determined as the lowest concentration that inhibits visible growth.

Evaluation of efficacy in acute B. pseudomallei mouse model of infection.

Dr. Jason Cummings from Colorado State University performed efficacy studies. 5-6 week old BALB/c female mice (Charles River Laboratories, Wilmington, MA) were challenged by intranasal infection with 5,000 CFU/mouse *B. pseudomallei* Bp400 (1026b Δ[amrAB-oprA] Δ[bpeAB-oprB]) (*138*). Animals were anesthetized with a mixture of 100 mg/kg ketamine and 10 mg/kg xylazine delivered intraperitoneally. The bacteria were diluted to the appropriate concentration in PBS to achieve an inoculum concentration of 2.5×10^5 CFU/mL. This inoculum was then delivered dropwise in alternating nostrils. Ceftazidime was formulated in PBS and test compounds in a lipid-based delivery system as previously described (*139*). Compounds were

delivered intraperitoneally, b.i.d. (twice daily) starting at time of infection. The number of viable bacteria in lung and spleen was determined at 60 h post-infection by plating serial 10-fold dilutions of homogenates on LB agar and incubating for 48 h at 37 °C. Bacterial burden was assessed and difference in group means was determined using a one-way analysis of variance (ANOVA) followed by Tukey's multiple comparisons test. Significance was determined by a P value < 0.05.

Results

Mutabilis compound, MUT056399, is a slow-onset inhibitor of BpFabI

   *Bp*FabI was shown to be sensitive to diphenyl ethers, in which these compounds were slow-onset inhibitors with K_i values of 0.5-2 nM (*94*). Therefore, we expanded our study to MUT056399, *p*-fluoro diphenyl ether. MUT056399 is a potent antistaphylococcal clinical candidate that inhibits *S. aureus* FabI with an IC_{50} value of 12 nM (*133, 134*). The apparent binding affinity (K_i^{app}) and residence time of MUT056399 for *Bp*FabI were 209 ± 28 nM and 35 ± 8 min, respectively (Table 4.1). Since *Bp*FabI was shown to be sensitive to MUT056399, the affect of *p*-fluorine introduction on the inhibitor's kinetic and thermodynamic properties should be evaluated and optimized.

The p-fluorine introduction may destabilize the transition state and ground state.

The diphenyl ether **PT04** was shown to be a potent nanomolar slow-onset inhibitor for FabI enzymes from *S. aureus* and *Francisella tularensis (41, 135)*. **PT04** was also found to completely rescue mice from death in a *F. tularensis* infection model, although it did not cause a significant reduction in bacterial burden in a methicillin-resistant *S. aureus* infection model (*104, 140*). Optimization of this compound series by Pan *et al* led to the synthesis of **PT91**, in which investigators demonstrated that **PT91** has efficacy in a *M. tuberculosis* infection model (*141*). Therefore, both **PT04** and **PT91** were selected to examine the effect of *p*-fluorine introduction.

The *p*-fluorine introduction on **PT91** (**PT417**) showed no significant effect on the k_{off} or residence time (tR) in comparison to **PT91** (Table 4.1). The binding affinity weakened by 5-fold after the introduction of *p*-fluorine on **PT417**, and the association rate (k_{on}) decreased by ~5 fold. This suggests a higher transition state barrier upon binding and the k_{off} was not affected because of kinetic-thermodynamic compensation between the ground state and transition state.

Interestingly, the K_i^{app} for **PT417** was comparable to those compounds with no B-ring substituents (**PT04**), while the residence time of **PT417** was similar to that of **PT91**. It is possible that modifications to the A-ring may predominantly affect ground state, while modifications to the B-ring will more likely affect transition state.

p-Fluoro diphenyl ethers' B-ring substituents may affect ground and/or transition states.

The trend of ground and transition states destabilization observed between **PT91** and **PT417** was hypothesized to be translated to **PT01** and Mutabilis FabI inhibitor (**PT411**) because they also differed by a *p*-fluorine on the A-ring (*133*) (Table 4.1). However, **PT01** and **PT411** had comparable k_{off}, k_{on}, and K_i^{app} values. Therefore, it is possible that both a *p*-fluoro group on the inhibitor's A-ring and an *ortho-* substituent on the inhibitor's B-ring were thought to be important for destabilization of the ground and/or transition states of EI*, which was seen for **PT417**. The introduction of an o-NO_2 group on the B-ring decreased the k_{on} and weakened the binding affinity by approximately 10-fold and 6-fold, respectively, whilst there was only a 2-fold difference in k_{off} (**PT411** vs. **PT412**). Conversely, an *o*-fluoro group on the B-ring enhanced K_i by approximately 4-fold, which led to a ~5-fold change in the k_{off} value with no change in k_{on} (**PT405** vs. **PT411**). The comparison of **PT405**, **PT411**, and **PT412** implies that less bulky substituents at the *ortho*-position on the B-ring will have little to no effect on the inhibitor affinity compared to larger substituents.

SAR studies were performed with a medium-sized substituent at the *ortho*-position on the B-ring (*o*-Cl group) in analogs that also contained a *p*-NH_2 (**PT403**) or *p*-NO_2 (**PT404**) group. Both compounds had comparable K_i values similar to **PT411**. However, the *p*-NO_2 group decreased k_{on} 20-fold (**PT411** vs. **PT404**), while the *p*-NH_2 group had little effect on k_{on} (**PT411** vs. **PT403**). This implies that the size of the substituent or electron-withdrawing groups at the *para*-position may have an affect on the association kinetics. The *p*-NO_2 group on the B-ring also decreased the k_{off} by 11-fold compared to *p*-NH_2 group (**PT403** vs. **PT404**).

The K_i^{app}, k_{on}, or k_{off} values were modulated by the addition of substituents on the inhibitor's B-ring. Surprisingly, the association rates for the tested *p*-fluoro diphenyl ethers display a strong linear correlation to K_i^{app} in a double logarithmic plot, whilst there was no significant correlation between the dissociation rates and K_i^{app} (Figure 4.2). This suggests that the energetics involved in residence time differentiation is related to the k_{on} of the final enzyme-inhibitor complex and not k_{off}. This is unexpected because there is more emphasis on the relationship between the kinetic parameters k_{off} and residence time (*127, 129, 130*).
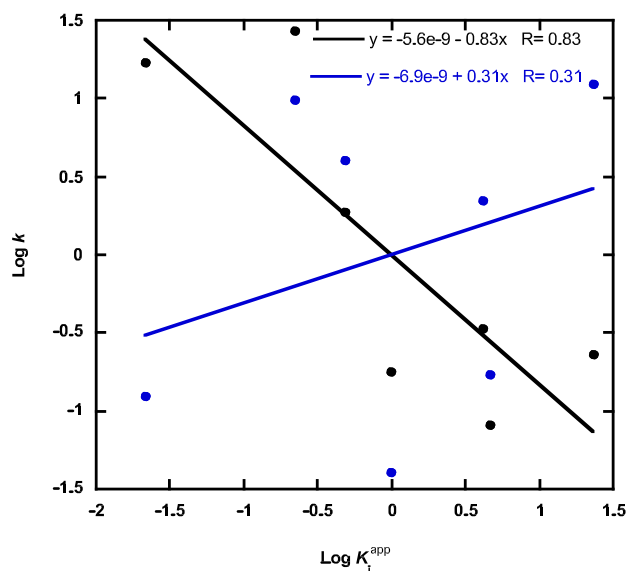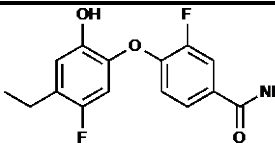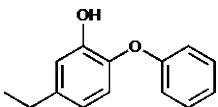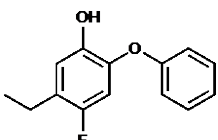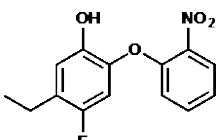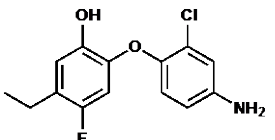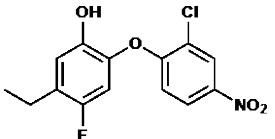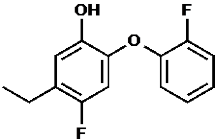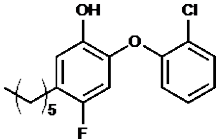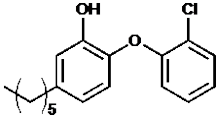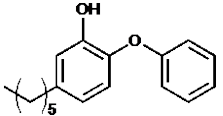
Figure 4.2 Kinetic and thermodynamic correlation.
A double logarithmic plot depicts a strong correlation between thermodynamic affinity and association kinetics (black) and a weak correlation between affinity and dissociation kinetics (blue). On each axis, logarithmic values were normalized such that their mean is approaching zero.

Table 4.1 Kinetic and thermodynamic parameters for inhibitors against *Bp*FabI

Compound	Structure	$K_i{}^{app}$ (nM)	K_i (nM)	$k_{on}{}^{app}$ $(M^{-1}min^{-1})$ [b]	k_{off} (min^{-1})	tR (min)
MUT056399		209 ± 28 [b]	177 ± 44 [d]	1.60×10^5	0.0284 ± 0.007 [b]	35 ± 8 [b]
PT01		28 ± 2 [b]	22 ± 4 [d]	2.08×10^6	0.0466 ± 0.009 [b]	19 ± 9 [b]
PT411		26 ± 3 [a] 26 ± 3 [b]	17 ± 3 [d]	1.36×10^6	0.0235 ± 0.004 [b] 0.0344 ± 0.002 [c]	41 ± 7 [b] 29 ± 1 [c]
PT412		51 ± 8 [a] 102 ± 7 [b]	100 ± 28 [d]	1.40×10^5	0.0133 ± 0.004 [b] 0.0125 ± 0.0009 [c]	91 ± 16 [b] 80 ± 6 [c]
PT403		50 ± 6 [a] 27 ± 3 [b]	27 ± 5 [d]	6.10×10^5	0.0167 ± 0.003 [b] 0.0163 ± 0.001 [c]	66 ± 5 [b] 61 ± 4 [c]
PT404		364 ± 7 [a] 66 ± 12 [b]	20 ± 7 [e]	7.00×10^4	0.0029 ± 0.002 [b] 0.0014 ± 0.0005 [c]	400 ± 250 [b] 713 ± 25 [c]
PT405		4 ± 0.2 [b]	4 ± 0.3 [d]	1.01×10^6	0.00446 ± 0.00033 [b]	225 ± 16 [b]

PT417	164 ± 25 [a] 130 ± 11 [b]	100 ± 12 [e]	5.0×10^4	0.00515 ± 0.002 [b] 0.00504 ± 0.0006 [c]	227 ± 30 [b] 198 ± 26 [c]
PT91	26 ± 3 [b]	20 ± 6 [d]	2.8×10^5	0.00551 ± 0.00169 [b]	196 ± 71 [b]
PT04	133 ± 3 [b]	90 ± 20 [d]	1.1×10^6	0.0996 ± 0.023 [b]	10 ± 2 [b]

(a) Determined by fitting data obtained from preincubation assays.
(b) Determined by fitting progress curve.
(c) Determined by fitting the ^{32}P-NAD-based dissociation curve.
(d) Affinity was calculated using k_{-1} and k_1 values obtained from progress curve analysis.
(e) Affinity was calculated using the k_{-1} value obtained from the ^{32}P-NAD dissociation assay since the dissociation rate was too slow. The k_1 value was obtained from forward progress curve analysis.

p-Fluoro diphenyl ethers bind to BpFabI via one-step binding mechanism

A plot of pseudo-first order rate constant (k_{obs}) as a function of inhibitor concentration revealed a linear fit for all tested compounds. A representative k_{obs} plot is depicted in Figure 4.3. This is a characteristic of a simple one-step binding mechanism and it unambiguously rules out the possibility of a conformational selection mechanism. Also, v_i remained unchanged at varying inhibitor concentrations coinciding with an one-step binding mechanism (*136*). Therefore, the data support these compounds bind to *Bp*FabI via one-step binding mechanism.
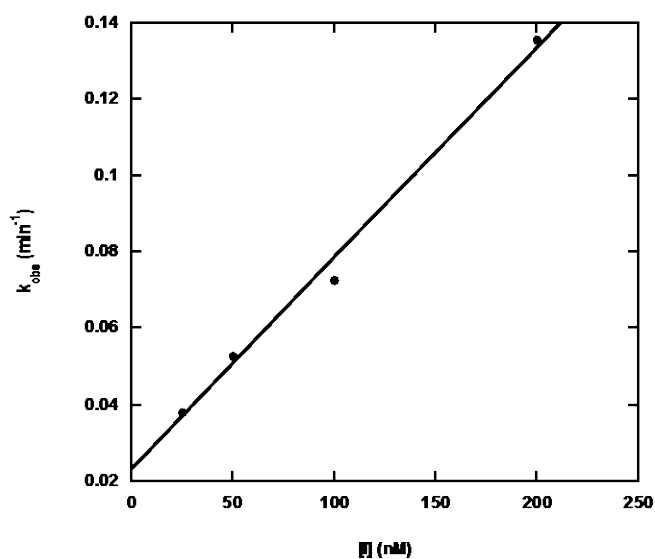
Figure 4.3 Representative plot of pseudo-first order rate constant (k_{obs}) as a function of inhibitor concentration.
Selected compound **PT403** gave a linear fit with a R^2=0.99.

p-Fluoro diphenyl ethers form an E-NAD$^+$-I complex with NAD$^+$ generated from catalysis and exogenous NAD$^+$

94

Thermal shift assays were performed to determine the preferred ternary complex that is formed in the presence of the inhibitor and either excess NADH or NAD^+. Cofactor preference was determined by shifts in the midpoint temperatures of the protein-unfolding transition (T_m). For example, the T_m shifted by approximately 10 °C for **PT412** in the presence of NAD^+ in comparison to NADH (Figure 4.4). Furthermore, all tested diphenyl ether inhibitors preferred binding to the enzyme-NAD^+ (E-NAD^+) complex with comparable T_m shifts as **PT412**.
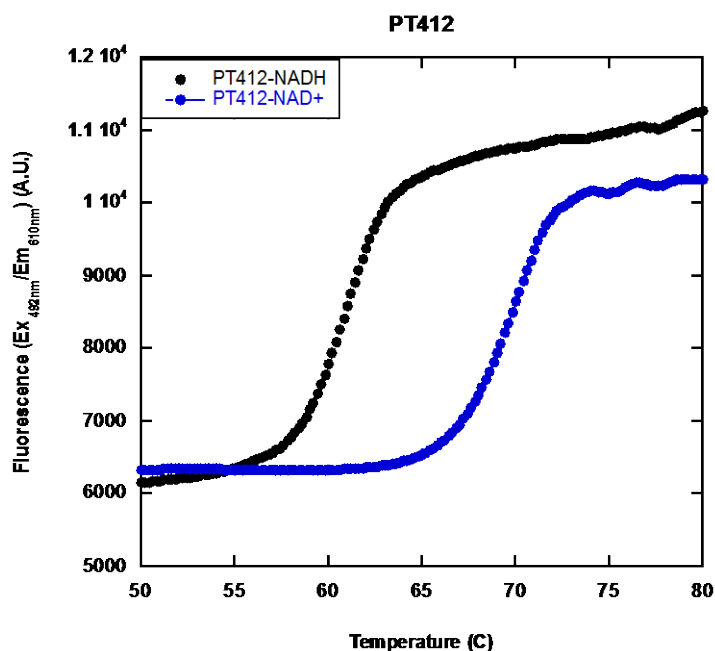
Figure 4.4 Midpoint temperatures of the protein-unfolding transition (T_m) for **PT412** in the presence of NADH (black) or NAD^+ (blue).

To examine whether the formation of E-NAD^+ product complex is dependent on oxidized cofactor generated from catalysis or from exogenous NAD^+, the concentration of enzyme or NAD^+ was varied. First, progress curves were performed at 200 μM and 1000 μM NAD^+, while

95

the concentration of enzyme and inhibitor (**PT403**) were held constant. The best-fit parameters for the k_{obs} and steady-state velocity (v_s) are 0.033 min^{-1} and 0.0091 $\mu M^{-1}min^{-1}$ at 200 μM NAD^+, and 0.048 min^{-1} and 0.0098 $\mu M^{-1}min^{-1}$ at 1000 μM NAD^+, respectively. Although v_s at both NAD^+ concentrations remained relatively unchanged with only a 7% difference, k_{obs} changed approximately 31%. The percent change for the rate constant conversion, from initial velocity phase to the steady-state velocity phase, was similar to the k_{obs} observed for only double the inhibitor concentration. Moreover, the residence time decreased insignificantly by 1.4-fold, from approximately 70 to 50 min.

The next set of progress curves were performed at different enzyme concentrations, 2 nM and 8 nM with compound **PT417**, in which increasing the enzyme concentration would increase the onset of the enzyme-inhibitor equilibrium. This resulted in a decrease in residence time approximately 4.5-fold from 227 ± 30 min to 64 ± 2 min with a 4-fold change in enzyme concentration. To confirm if we are underestimating or overestimating residence time, the residence time was also measured by a direct dissociation assay. The residence time was 198 ± 26 min and this value coincided with the residence time measured from progress curve analysis at lower enzyme concentration.

Taken together the two sets of controls, the formation of E-NAD^+-I complex is dependent on oxidized cofactor generated from catalysis and binding to free enzyme (Scheme 4.1).

$$k_{cat} \quad E\text{-}NAD\text{-}P$$

E–NADH–S

$$k_{on,S}\,[S]$$

E–NADH

$$k_{on,NAD}\,[NAD] \qquad k_{off,NAD}$$

$$E\text{-}NAD \xrightleftharpoons[k_{-1}]{k_1\,[I]} E\text{-}NAD\text{-}I$$

$$k_{on,NADH}\,[NADH] \qquad E$$
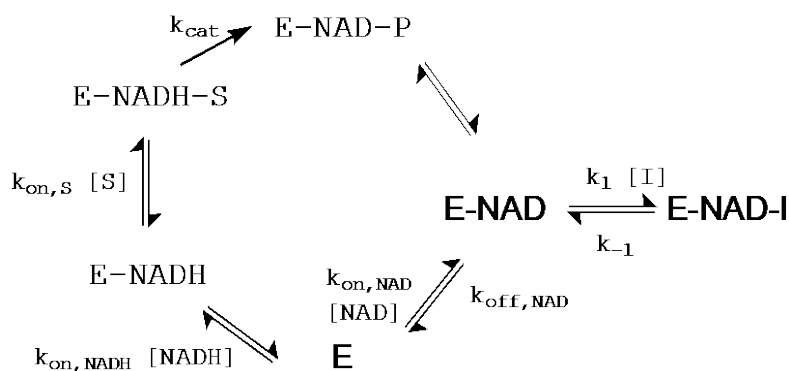
Scheme 4.1 Detailed kinetic mechanism for inhibition of *Bp*FabI by *p*-fluoro diphenyl ether

In vivo efficacy of PT405

Lead compound **PT405** had MIC values of 0.5 μg/mL and 0.125 μg/mL in wild-type *B. pseudomallei* (Bp1026b) and an efflux pump knockout (Bp400), respectively. Efficacy of **PT405** was evaluated in the acute *B. pseudomallei* animal model using the efflux knockout strain Bp400 (Figure 4.5). Mice were challenged with 5000 CFU and bacterial burden was assessed at 60 h post infection in lung and spleen homogenate. Efficacy of **PT405** was measured against an untreated control group and a positive control, 200 mg/kg ceftazidime treated group. There was no significant reduction in lung burden; however, **PT405** showed a significant reduction (P <0.001) of 1.69 Log_{10} CFU/mL in bacterial burden in the spleen.

A

B
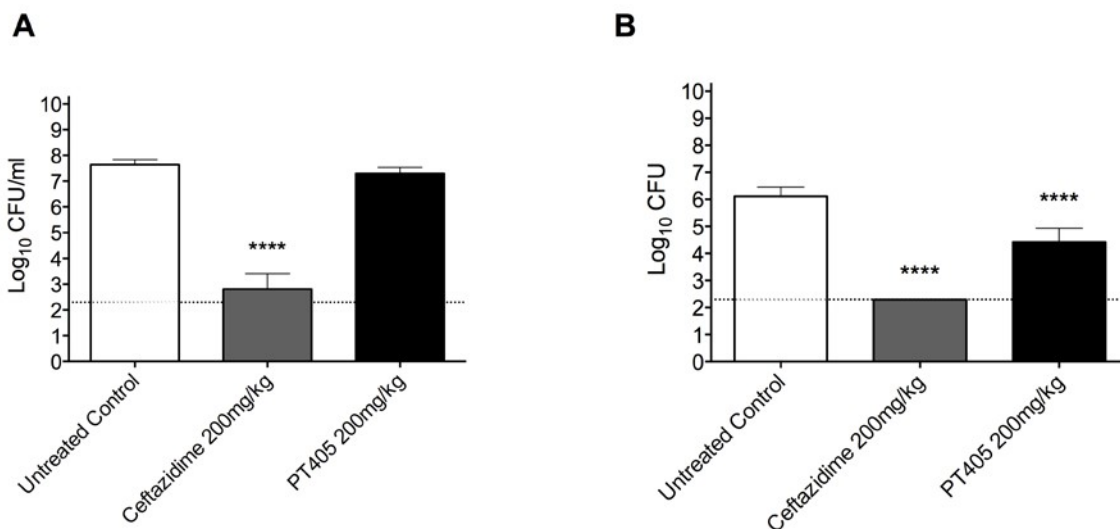
Figure 4.5. Bacterial burden in mouse lung (A) and spleen (B) at 60 h post infection.
The mean of each group was plotted and error bars indicating +/- standard deviation. Significance was determined by one-way ANOVA and Tukey's multiple comparison post-test (**** $P<0.0001$). Dotted line represents limit of detection. Figure provided by Dr. Jason Cummings.

Discussion

Mutabilis FabI inhibitor, MUT37307, is a first-generation p-fluoro analog of triclosan, and it was found to be specific for organisms that contain only FabI ENR isoenzymes (*132*). MUT056399 was later synthesized as a second-generation p-fluoro diphenyl ether inhibitor (*133, 134*). MUT056399 displayed inhibitory activity for BpFabI with a K_i and residence time of ~177 nM and ~35 min, respectively. This compound exhibited a weaker binding affinity and shorter dissociation kinetics for BpFabI compared to *S. aureus* FabI, in which K_i and residence time for MUT056399 were ~0.08 nM and ~223 min, respectively (*140*). This finding was expected

98

since MUT056399 was optimized to target *S. aureus* FabI and is currently undergoing clinical development to treat Staph infections in humans (*133, 134*). SAR studies were then conducted to understand kinetic and thermodynamic properties of *p*-fluorine introduction and how this modulated binding to *Bp*FabI.

Diphenyl ethers are known to preferentially bind to the E-NAD$^+$ product complex (*91, 94, 116, 142*), which was consistent with all tested *p*-fluoro diphenyl ethers. In this study, the origin of the E-NAD$^+$ complex is through catalysis and binding of NAD$^+$ to the free enzyme. Surprisingly, all tested compounds follow a one-step binding mechanism. This was unexpected because Liu *et al* demonstrated that slow-onset diphenyl ethers target *Bp*FabI though an induced-fit, two-step model (*94*). However, a one-step binding mechanism is kinetically indistinguishable from a special case induced-fit, two-step mechanism. In a special case induced-fit model, the EI* is much lower in free energy than EI. Under this circumstance, initial inhibition cannot be detected at low inhibitor concentrations while steady-state velocity can be affected. It is not unusual for slow-onset inhibitors to follow a special case induced-fit model with FabI ENRs, since it was shown in the *S. aureus* FabI system (*135*). If the *p*-fluoro diphenyl ethers follow a special case induced-fit binding mechanism, then slow binding may be due to the binding affinity to the initial complex, not k_{on}. Unfortunately, this factor is not kinetically distinguishable in our system and structural studies of inhibitors in complex with *Bp*FabI will be needed to provide more information on the slow binding mechanism.

SAR studies that included modifications on the inhibitor's B-ring revealed changes in the K_i^{app}, k_{on}, or k_{off} values. Remarkably, the association kinetics of the *p*-fluoro diphenyl ethers displayed a strong linear correlation to binding affinity in a double logarithmic plot, while there was no significant correlation between binding affinity and the dissociation kinetics. This suggests that the energetics involved in residence time differentiation is related to the k_{on} of the final enzyme-inhibitor complex. This is interesting because the transition state energy barrier upon inhibitor binding has been overlooked and there is a greater focus on the kinetic parameters k_{off} and residence time (*127, 129, 130*). To our knowledge, this trend is unique to analogs of Mutabilis second-generation compounds since studies by Chang *et al* revealed a strong correlation between dissociation rates and thermodynamic affinity in a logarithmic plot for diphenyl ethers (*135*). Taken together, we speculate that the *p*-fluoro on the inhibitor's A-ring along with *ortho*-substituents on the B-ring may affect k_{on} and K_i.

Although there were no significant differences in inhibitor conformations between Triclosan and **PT404** bound to *Bp*FabI (Figure 4.6.A), investigators have shown that the C−OH rotational barrier height in *p*-fluorophenols decreases as well as the −OH torsional vibration frequency (*143, 144*). Therefore, increasing the degree of freedom of −OH may be unfavorable for the k_{on} of *p*-fluoro diphenyl ethers. It is possible that the removal of the fluoro-group on the A-ring allows the C−OH to be more rigid and positioned in a favorable conformation to hydrogen bond to the active site Y156 (Figure 4.6.B). Therefore, we speculate the slower k_{on} for the tested diphenyl ethers may be due to the time consequence to form a favorable hydrogen bond with the active site residue.

Additionally, the *p*-fluoro group in **PT404** is in proximity of hydrophobic residues A197, I200, and F203 (Figure 4.6.C). Longer acyl chain substituents next to *p*-fluorine on the inhibitor's A- ring may adopt conformations that could enhance hydrophobic interactions between the C-F and acyl chain. This can be unfavorable for the inhibitor's acyl chain to initially enter the hydrophobic substrate binding tunnel, which will eventually weaken the binding affinity as seen in the comparison of **PT91** and **PT417**. Based on our results, unfavorable inhibitor conformations may be circumvented by having a shorter acyl chains next to the *p*-fluorine (**PT01** vs. **PT411**).
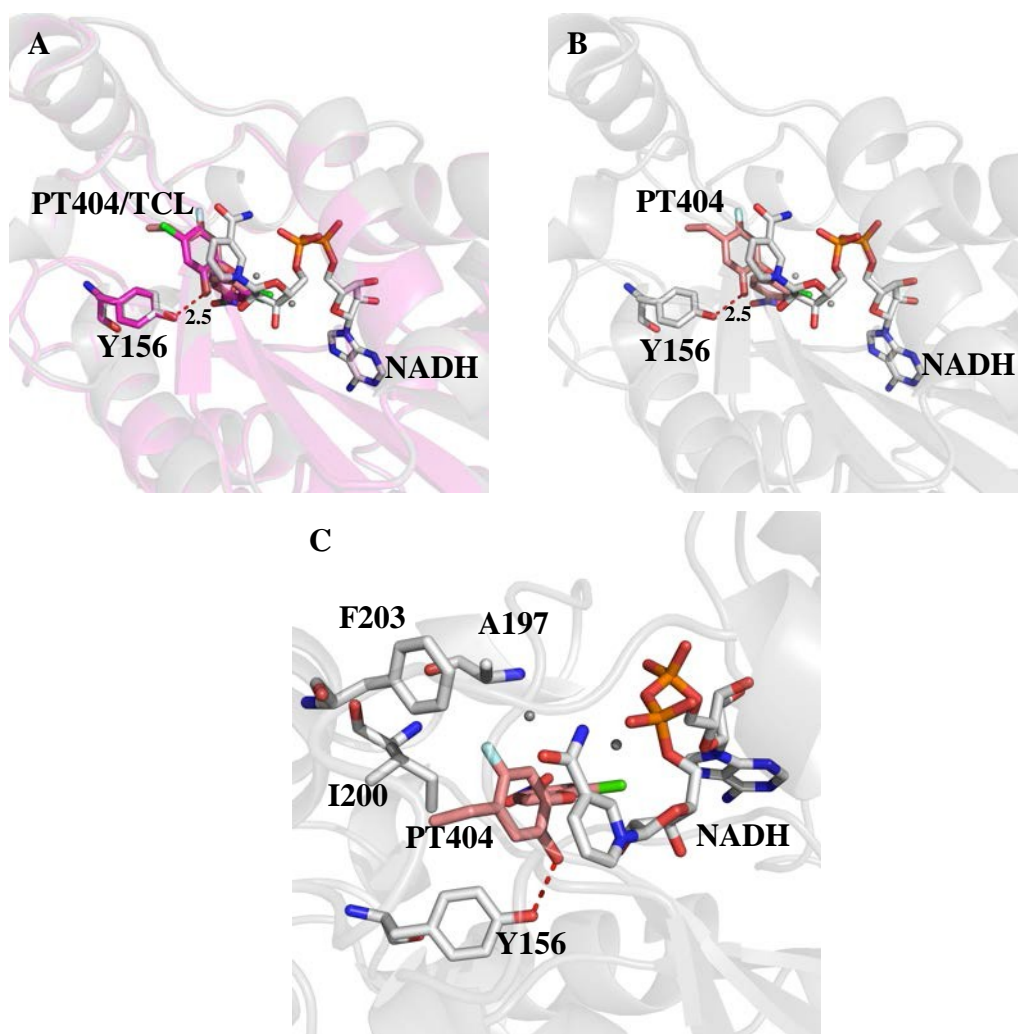
Figure 4.6 Differences in the structures for PT404 and Triclosan in complex with *Bp*FabI and NADH.
(A) Superposition of *Bp*FabI bound to PT404 and triclosan (TCL), along with NADH (unpublished structures). (B) PT404 in complex with *Bp*FabI and NADH (unpublished structure). (C) Hydrophobic residues in proximity to the *p*-fluoro group. TCL in complex with *Bp*FabI is shown in dark pink; PT404 in complex with *Bp*FabI is shown in grey; and hydrogen bonding interactions are represented by dashes.

Throughout our SAR studies, we evaluated optimal values for the parameters K_i^{app}, k_{on}, and k_{off}, with a focus on k_{on}. It is important to note that one limitation in decreasing k_{on} is that *in vivo* metabolism will have a greater impact on the rate of target engagement. This is important since diphenyl ethers are susceptible to Phase II conjugation reactions (*69*). There may not be a direct effect on residence time by k_{on} if interactions between the inhibitor and the enzyme are optimized. This is exemplified by **PT405,** in which the ground state of the FabI-NAD$^+$ product complex is stabilized. Lead compound **PT405** was later selected for animal studies for three reasons. First, it had a strong thermodynamic affinity to *Bp*FabI with a K_i^{app} value of 4 ± 0.2 nM. Second, it had a long residence time of 225 ± 16 min. Third, it had antimicrobial activity with MIC values of **PT405** are 0.5 µg/mL and 0.125 µg/mL in wild-type *B. pseudomallei* and an efflux pump knockout strain. Interestingly, **PT405** had efficacy in the animal model of melioidosis, causing a reduction in bacterial burden in the spleen by 1.69 Log$_{10}$ CFU/mL.

In conclusion, Mutabilis second-generation analogs provided a unique mechanistic insight, in which k_{on} correlated well with K_i^{app}. SAR studies will need to be expanded in order to determine when k_{on} or k_{off} would directly impact residence time for this compound series. Further optimization of these promising candidates can provide potential drug candidates for anti-bacterial activity against *B. pseudomallei*, which was shown with our *in vivo* efficacy animal model.

Chapter 5: Translating the Slow-onset Inhibitor Mechanism from a FabI ENR to FabV ENR

Background

Structural basis for slow-onset inhibitor mechanism

The lifetime of the enzyme-inhibitor complex is important to consider *in vivo* because inhibitor concentration is generally not constant. One parameter that provides information on the lifetime of the drug-target complex is residence time, which is the inverse of the rate of dissociation ($1/k_{off}$) (*129*). For some inhibitors, the equilibrium between the free and enzyme-bound inhibitor forms is established slowly with respect to the time scale for enzymatic turnover. (*136, 145*).

Although many inhibitors display slow binding character, in most cases the structural basis for this remains unknown. For example, kinetic analyses have shown that triclosan and its analogues are slow, tight binding inhibitors of the enoyl-ACP reductase (ENR) FabI class in several organisms (*41, 44, 91, 93, 94, 111, 113, 146, 147*). In some of these systems, overlays of X-ray crystal structures of the free enzyme and enzyme-inhibitor complexes revealed slow binding inhibition may be caused by changes in the substrate recognition loop, which becomes ordered upon inhibitor binding (Figure 5.1.A) (*142, 148*). However, the same mechanism does not apply to the FabV ENR since this loop remains ordered even in the apo form and then becomes disordered in the presence of rapid reversible inhibitors (Figure 5.1.B) (*42*). In addition,

104

to our knowledge there are currently no known slow-onset inhibitors against the ENR FabV class hindering our ability to study time dependent inhibition in this system.

Inhibitor entry into the binding pocket of T276S YpFabV

Structural differences of substrate recognition loops within different ENR classes inspired a new working hypothesis on the structural basis of slow-onset inhibition. Our lab recently published a structural and energetic model for slow-onset inhibition of *M. tuberculosis* FabI (*149*). In this model, the substrate binding loop adopts an open or closed conformation upon inhibitor binding, representing the EI and EI* states (Figure 5.2) (*149*). Thus, it is possible that slow binding may be due to an enzyme-inhibitor complex approaching a conformationally stable closed-state, and the ordering of the substrate loop consequently created the energy barrier for the slow step. On the basis of this hypothesis, we re-evaluated the entry of 2-pyridone inhibitors into the T276S *Yp*FabV binding pocket because these are the only X-ray structures of the FabV class to date that could provide information on inhibitor and substrate binding (*42*). Figure 5.3.A portrays a surface map of T276S *Yp*FabV (PDB 3ZU5), in which the substrate-mimic inhibitor (grey) and cofactor (green) are bound to the enzyme. If this model represents the open conformation of the enzyme-inhibitor complex, it is possible that the inhibitor could rapidly dissociate and/or re-associate from the major portal since the portal remains predominantly open.

105

A)

B)
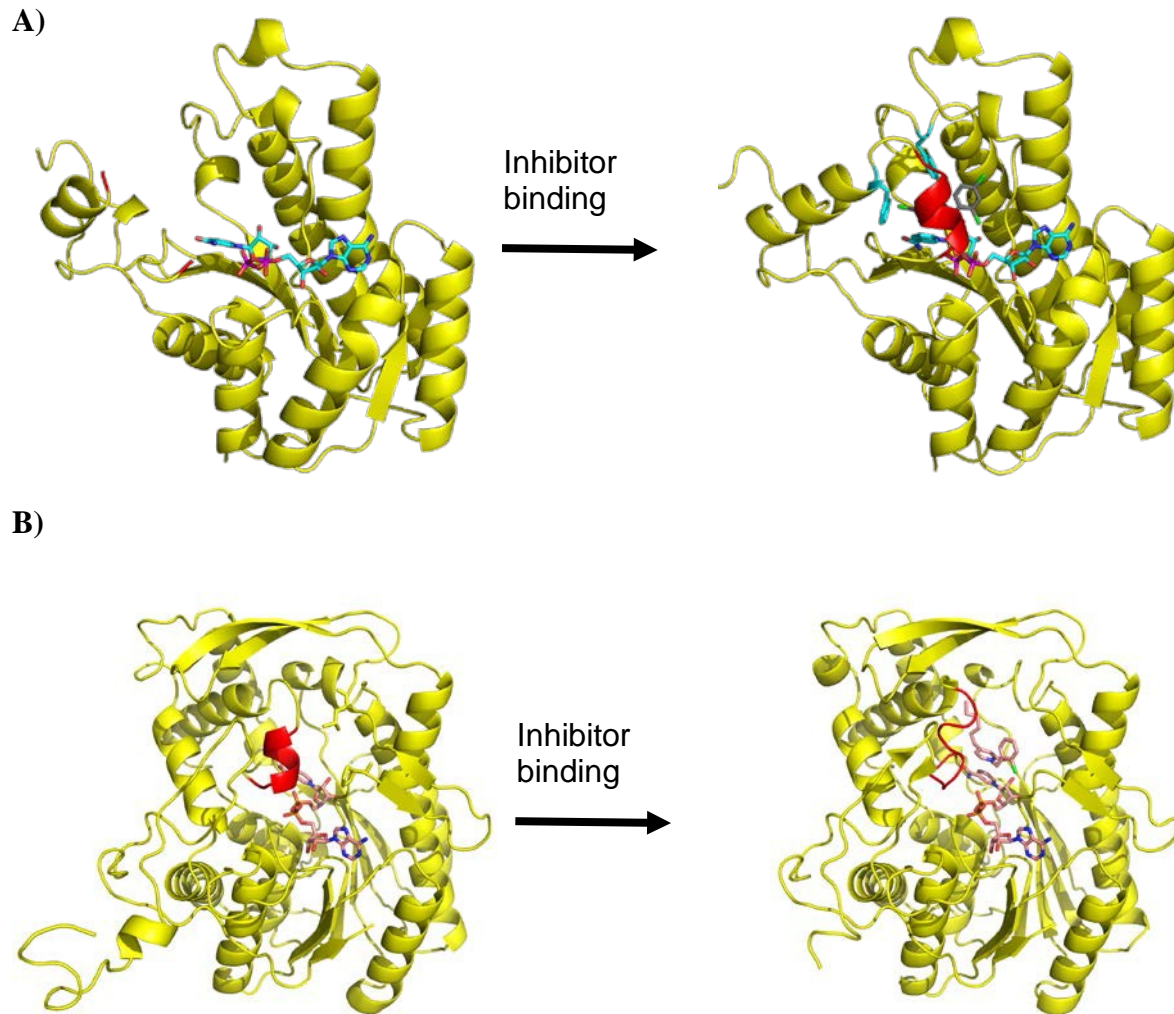
Figure 5.1 Structural insights into the folding and unfolding states of the substrate binding loop for FabI and FabV.

(A) Substrate binding loop of FabI from *M. tuberculosis* becomes ordered upon binding to a slow-onset inhibitor adapted from Luckner *et al* (*113*) (B) Substrate binding loop of FabV from *Y. pestis* becomes disordered upon binding to a rapid reversible inhibitor (unpublished structure and PDB 3ZU2). The substrate binding loop is shown in red.

Open Conformation (E, EI)   Closed Conformation (EI*)
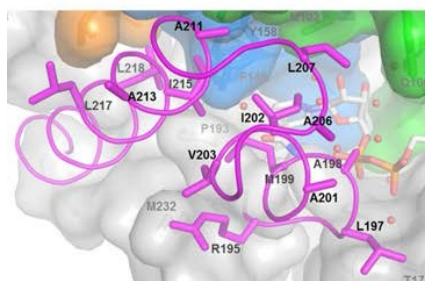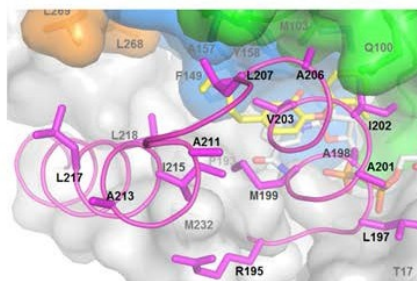
Figure 5.2 Structural insights into the open and closed conformations of the substrate binding loop for *M. tuberculosis* FabI.
Adapted from Li and Lai *et al* (*149*).

Our approach is to mutate the enzyme to form a conformationally stable closed-state that will consequently create an energy barrier for either inhibitor association or dissociation. We determined that Pro142 is a good candidate for mutagenesis using computational analysis which revealed that a Trp at this position would favor a conformationally stable closed-state (Figure 5.3.B). In turn, we could gain slow-onset inhibition for an inhibitor that displays rapid-reversible binding kinetics for the wild-type enzyme.

Project Goals

In order to gain slow-onset inhibition for *Yp*FabV, we need to understand how to induce an open and closed conformation on the enzyme-inhibitor binding coordinate. Therefore, we mutated residues near the active site that can permit the transition from a rapid reversible to a slow-onset inhibitor mechanism for *Yp*FabV. We also performed inhibition studies and progress curve analysis with lead compounds that target both P142W mutant and wild-type *Yp*FabV.
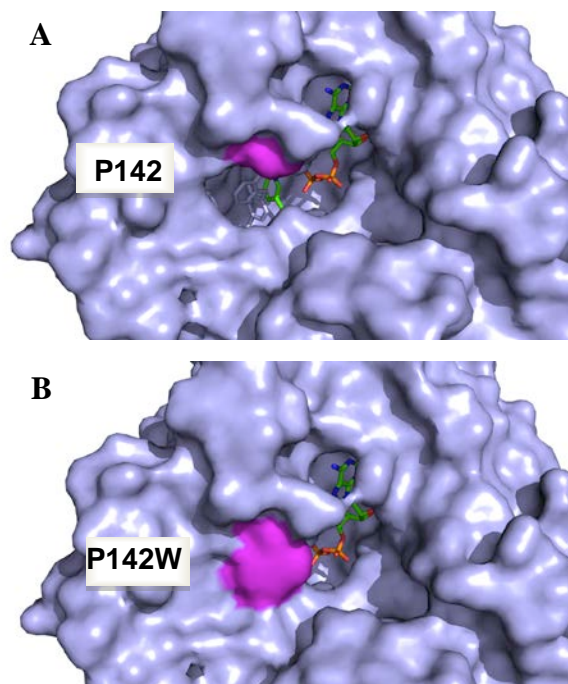
Figure 5.3 Inhibitor entrance into the binding pocket of T276S *Yp*FabV (PDB 3ZU5)
(A) Surface map of T276S *Yp*FabV bound to substrate-mimic inhibitor (grey) and NADH (green). Residue P142 is shown in pink and (B) the surface area of proposed mutant closes the major binding portal.

Materials and Methods

Materials

   His-bind Ni^{2+}-NTA resin was purchased from Invitrogen, and Luria broth was obtained from VWR. *trans*-2-Dodecenoic acid was purchased from TCI. Lauroyl and crotonyl coenzyme A (crot-CoA) was purchased from Sigma-Aldrich. All other chemical reagents were obtained from Fisher. All progress curve fitting was performed using KaleidaGraph Version 4.1. All

product inhibition plots were fitted using GraFit. All thermal shift plots were analyzed using GraphPad Prism.

Synthesis of trans-2-dodecenoyl-CoA (ddCoA)

ddCoA was synthesized from *trans*-2-dodecenoic acid using the mixed anhydride method as previously described (*89*). Product formation was confirmed by ESI mass spectrometry.

Site-directed mutagenesis, expression, and purification of P142W YpFabV

P142W *Yp*FabV mutant was prepared using the primers: 5' CTATAGCCTTGCTTCATGGCGACGCACCCATCCG3', 5'CGGATGGGTGCGTCGCCATGAAGCAAGGCTATAG3', and the forward and reverse primers for wild-type *Yp*FabV (Table 2.1). The amplified PCR product that contained the mutated FabV gene was digested with XhoI and EcoRI and inserted into a pET15b vector (Novagen). The sequence of the mutant plasmid was confirmed by DNA sequencing. Protein expression and purification for both the wild-type *Yp*FabV and P142W *Yp*FabV were performed as described previously using *E. coli* BL21(DE3) and BL21(DE3) pLysS cells (*42*). The concentration of wild-type and P142W *Yp*FabV was spectrophotometrically determined at 280 nm, using the extinction coefficients of 48,360 M^{-1} cm^{-1} and 53,860 M^{-1} cm^{-1}, as calculated from the primary sequences of the proteins (ExPASy ProtParam tool).

Cloning, expression, and purification of PaFabV.

The *fabV* gene was amplified by PCR from *Pseudomonas aeruginosa* CO92 with the forward primer 5' GGAATTC<u>CATATG</u>ATCATCAAACCGCGCGTGCGTGGCTTC3' and reverse primer 5' CGC<u>GGATCCT</u>CAGGCCTGGATCAGGTTGGCGATCTG 3'. The PCR amplified product were treated with NdeI and BamHI and inserted into the pET15b vector (Novagen), such that a hexa-histidine tag was encoded at the N-terminus. The construct was transformed, purified and sequenced as described above. The concentration was spectrophotometrically determined at 280 nm and by using an extinction coefficient of 48,360 $M^{-1}cm^{-1}$.

Direct binding experiments.

A titration fluorescence assay was used to determine the dissociation constant, K_d, of the substrate in reaction buffer containing 30 mM PIPES, 150 mM NaCl, 1.0 mM EDTA at pH 8.0. Briefly, the substrate was titrated into a sample containing 0.5 μM enzyme and reaction buffer at 25 °C. The sample was monitored at the excitation and emission wavelengths of 280 and 332 nm with slit widths of 4.0 and 2.0 mm, respectively. The K_d values were calculated using a Scatchard equation (*90*) from the software GraFit (Equation 5.1).

$$y = \frac{\lfloor L \rfloor \times Cap}{K_d + [L]}$$

Equation 5.1

110

Where, y is the amount of ligand bound per the amount of receptor; *Cap* is the capacity for the binding ligand; [L] is the concentration of the free ligand; and K_d is the dissociation constant of the ligand from the receptor.

Steady-state kinetic analysis

Steady-state kinetics were performed on a Cary 100 Bio (Varian) spectrophotometer at 25 °C in a buffer solution containing 30 mM PIPES, 150 mM NaCl and 1.0 mM EDTA at pH 8.0 (*42*). The initial velocities were measured by monitoring the oxidation of NADH to NAD^+ at 340 nm (ε = 6,220 M^{-1} cm^{-1}). Substrate specificity was analyzed using the Michaelis-Menten equation (Equation 5.2) by measuring initial velocities at varying concentrations of CoA-based substrates and a fixed concentration of NADH (250 µM), where, v_{max} is the maximum velocity; [S] is the substrate concentration; and K_M is the Michaelis-Menten constant for the substrate.

$$v_o = \frac{v_{max}[S]}{K_M + [S]}$$

Equation 5.2

The substrate binding mechanism was analyzed by measuring initial velocities at varying concentrations of one substrate, while fixing the other substrate concentration at sub/saturating concentrations.

The product inhibition mechanisms were analyzed using Lineweaver-Burk plots by measuring the initial velocities at a fixed concentration of NADH (250 µM) and varying concentrations of ddCoA and inhibitor. Inhibition constants for competitive, uncompetitive, and

noncompetitive inhibitors were analyzed using Equations 5.3-5, where [S] is the substrate concentration; [I] is the inhibitor concentration; K_M is the Michaelis-Menten constant for the substrate; v_{max} is the maximum velocity; and K_i and K_i' are inhibition constants.

$$v_o = \frac{v_{max}[S]}{K_M\left(1 + \frac{[I]}{K_i}\right) + [S]}$$

Equation 5.3

$$v_o = \frac{v_{max}[S]}{K_M + [S]\left(1 + \frac{[I]}{K_i'}\right)}$$

Equation 5.4

$$v_o = \frac{v_{max}[S]}{K_M\left(1 + \frac{[I]}{K_i}\right) + [S]\left(1 + \frac{[I]}{K_i'}\right)}$$

Equation 5.5

Inhibition assays

The half maximal inhibitory concentration, IC_{50}, values were determined by varying the inhibitor concentration (2% DMSO) in the reactions containing 250 μM NADH and 30 μM ddCoA with 15 nM enzyme. The experimental data were analyzed using Equation 5.6, such that I is the inhibitor concentration and y represents the percent activity.

$$y = \frac{100\%}{1 + \frac{I}{IC_{50}}}$$

Equation 5.6

Complex formation assay

A complex formation assay was adapted and modified from a ^{32}P dissociation kinetic method developed by lab member Ms. Weixuan Yu (*135*). A mixture of 15 µM enzyme, 20 µM NADH, and 0-200 µM inhibitor was incubated at 4 °C overnight. The sample was loaded onto a G25 Sephadex spin column and centrifuged at 2500 rpm for 2 min. An absorbance spectrum of the flow-through was taken and quantified using a Cary 300 Bio (Varian) spectrophotometer at 25°C.

Thermal shift assay

ThermoFluor experiments were performed as previously described to determine inhibitor cofactor preference (*135*). To a 96-well thin-wall PCR plate (Conrad), 7.4 µM enzyme, 2.5 mM cofactor (NADH or NAD$^+$), and 25 µM inhibitor (2% DMSO) was added to a solution containing 30 mM PIPES, 150 mM NaCl and 1.0 mM EDTA at pH 8.0. Samples were incubated at 25°C for 1.5 h. After incubation, 1 µL of 100 × Sypro Orange (Sigma) was added to each well and the plate was sealed with Microseal 'B' Film (Bio-Rad). The samples were heated from 25 to 90 °C in increments of 0.2 °C/10 s. Bio-Rad CFX Manager was used to process the data.

Progress curve analysis

Slow-onset inhibition kinetics were monitored at 340 nM on a Cary 100 Bio (Varian) spectrophotometer at 25 °C. The reactions were initiated by the addition of the enzyme (5 nM) to a mixture containing glycerol (8%), bovine serum albumin (0.1 mg/mL), DMSO (2% *v/v)*, crot-CoA (900 µM), NADH (250 µM), NAD$^+$ (200 µM) and an inhibitor (0-8000 nM). All reactions were monitored until steady-state was reached, which was indicated by linearity of the progress curve (*93, 135, 137*).

Data were analyzed as previously described (*41, 136*) and fitted to the Morrison & Walsh integrated rate equation (Equation 5.7), where; A_t and A_0 are the absorbance at time t and 0; v_i and v_s are the initial and steady-state velocities; and k_{obs} is the observed pseudo-first rate order constant for the approach to steady-state.

$$A_t = A_0 - v_s t - (v_i - v_s) * \frac{1 - e^{-k_{obs}t}}{k_{obs}}$$

Equation 5.7

The plot of fractional initial (v_i) and steady-state (v_s) velocities as a function of inhibitor concentration was fitted to the isotherm equation to determine the inhibition constants for initial and final binding to enzyme, K_i^{app} and $K_i^{*,app}$ (Equation 5.8 and 5.9). The parameters v_c and [I] represent the uninhibited reaction velocity and the inhibitor concentration. The dissociation rate of the inhibitor, k_{-1}, was calculated from each progress curve using Equation 5.10. For induced-

fit slow-onset kinetics, the association rate of the inhibitor for the second step ($k_{\text{on, 2nd step}}$) and overall association rate of the inhibitor ($k_{\text{on, overall}}$), were calculated from each progress curve using Equation 5.11 and Equation 5.12.

$$\frac{v_i}{v_c} = \frac{1}{1 + \frac{[I]}{K_i^{app}}}$$

Equation 5.8

$$\frac{v_s}{v_c} = \frac{1}{1 + \frac{[I]}{K_i^{*,app}}}$$

Equation 5.9

$$k_{-1} = k_{obs} * \frac{v_s}{v_i}$$

Equation 5.10

$$k_{on,2nd\ step} = \frac{(k_{obs} - k_{off})(K_i^{app} + [I])}{[I]}$$

Equation 5.11

$$k_{on,overall} = \frac{k_{on,2nd\ step}}{K_i^{app}}$$

Equation 5.12

Results

P142W YpFabV co-purified with chloramphenicol acetyltransferase

The purification of P142W *Yp*FabV was verified using a 15% SDS PAGE gel, and a contaminant was co-purified with the enzyme (Figure 5.4.A). The contaminant was in-gel

digested and confirmed by the Stony Brook University Proteomics Facility MALDI-TOF (Figure

5.4.B). The most likely candidate was *E. coli* chloramphenicol acetyltransferase. Since this

protein is from the chloramphenicol-resistant plasmid found in *E. coli* BL21(DE3) pLysS host

strains, we changed the expression cell line to E. *coli* BL21(DE3) and the contaminant was

successfully removed (Figure 5.4.C).
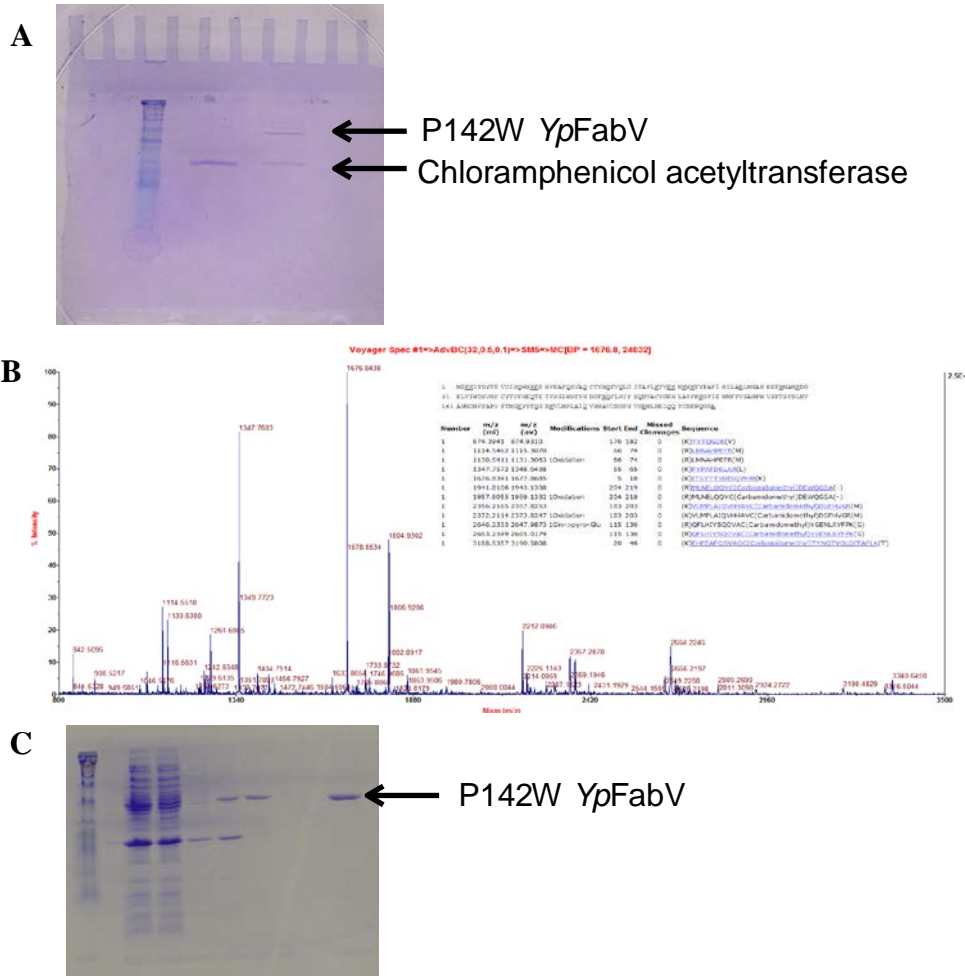
Figure 5.4 Identification of contaminant co-purified with P142W *Yp*FabV
(A) 15% SDS-PAGE gel of purified P142W *Yp*FabV expressed in *E.coli* BL21(DE3) PlysS.
Protein ladder (left), peak 1 from size exclusion chromatography (middle), peak 2 from size
exclusion chromatography (right). (B) MALDI-TOF analysis of in-gel trypsin digest of
contaminant by Dr. Antonius Koller. (C) 15% SDS-PAGE gel of purified P142W *Yp*FabV

expressed in *E.coli* BL21(DE3). From left to right: Protein ladder; cell lysate; cell lysate flow-through from His-bind resin; wash 1 sample; wash 2 sample; peak 1 from His-bind resin; and peak 1 from size exclusion chromatography.

P142W catalyzes substrate reduction via an ordered bi-bi mechanism, in which NADH binds first to the enzyme

The steady-state kinetic parameters k_{cat}, K_M, and k_{cat}/K_M for ddCoA with P142W *Yp*FabV are 3866 ± 243 min^{-1}, 12 ± 2 µM, and 349 ± 60 µM^{-1}min^{-1}, respectively. These values were comparable to the kinetic parameters for ddCoA with wild-type *Yp*FabV and FabVs from other pathogens under the optimized expression and purification conditions (Table 5.1). As expected, analysis of the double-reciprocal plots showed that the substrate binding mechanism was comparable to wild-type *Yp*FabV, in which substrate reduction follows a ternary complex mechanism (data not shown). Interestingly, high µM concentrations of NAD$^+$ did not inhibit P142W *Yp*FabV; therefore, we conducted product inhibition plots with lauroyl coenzyme A (CoA). The product inhibition studies revealed that lauroyl CoA follows a mixed pattern with respect to NADH and a noncompetitive pattern with respect to ddCoA (Figure 5.5). The product inhibition pattern indicates that the substrates bind through an ordered bi-bi mechanism, in which NADH binds first to the enzyme (*95, 96*).

Table 5.1 Comparison of steady-state kinetics for FabV enzymes

Enzyme	$K_{M, ddCoA}$ (μM)	$k_{cat, ddCoA}$ (min^{-1})	k_{cat}/K_M (μM^{-1}min^{-1})
wild-type *Yp*FabV	12 ± 2	5468 ± 426	456 ± 84
P142W *Yp*FabV	12 ± 2	3866 ± 243	349 ± 60
B pseudomallei FabV	1.9 ± 0.2	815 ± 21	429 ± 46
P. aeruginosa FabV	4.2 ± 0.2	1553 ± 36	370 ± 20
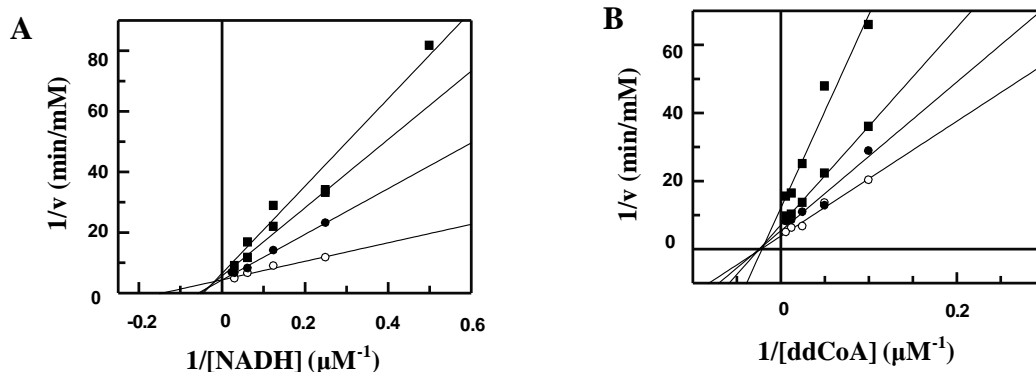
Figure 5.5 Product inhibition studies to determine the substrate binding mechanism of P142W *Yp*FabV

To evaluate product inhibition, one substrate concentration was varied, while the second substrate concentration was fixed and in the presence of lauroyl CoA. Initial velocity patterns: (A) 1/v versus 1/[NADH] double-reciprocal plot in which [lauroyl CoA] was fixed at (O) 0 μM lauroyl CoA (•) 4 μM lauroyl CoA ($\square$) 8 μM lauroyl CoA, and (■) 16 μM lauroyl CoA; and (B) 1/v versus 1/[ddCoA] double-reciprocal plot in which [lauroyl CoA] was fixed at (O) 0 μM lauroyl CoA (•) 4 μM lauroyl CoA ($\square$) 8 μM lauroyl CoA, and (■) 16 μM lauroyl CoA.

Fluorescence binding experiments revealed K_d values of 6 ± 0.2 µM and 56 ± 2 µM for NADH and ddCoA, respectively, in which NADH had an approximate 9-fold binding affinity preference over ddCoA to the free enzyme (Table 5.2). However, substrate binding preference shifts for the ternary complex, which showed ddCoA had a 5-fold binding affinity preference for the ternary complex over NADH. These results coincide with the product inhibition plots, in which NADH will bind first to the enzyme, and then ddCoA will bind to the binary complex.

Table 5.2 Comparison of binding constants to the free enzyme and ternary complex
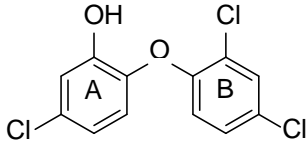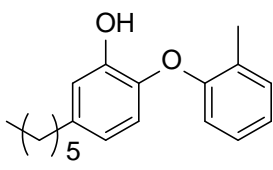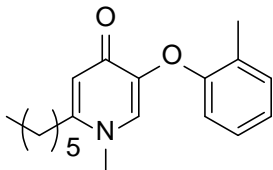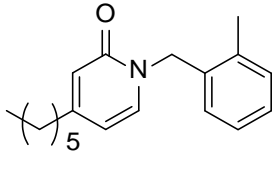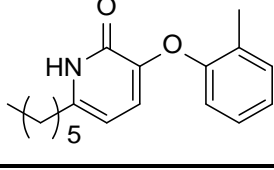
$K_{d,\,ddCoA}$ (µM)	$K_{d,\,NADH}$ (µM)	$K_{m,\,ddCoA}$ (µM)	$K_{m,\,NADH}$ (µM)
56 ± 2	6 ± 0.2	12 ± 2	55 ± 8

4-Pyridone-based scaffold can promiscuously bind to YpFabV and its mutant

In Chapter 3, we showed that the diphenyl ethers selectively inhibited wild-type *Yp*FabV, while the 2-pyridones selectively inhibited T276S *Yp*FabV. We also showed that the best inhibitor scaffold was the 4-pyridones because this scaffold inhibited wild-type *Yp*FabV and T276S *Yp*FabV, along with other ENRs such as *Bp*FabI and *Bp*FabV. Therefore, we screened the same inhibitor scaffolds against the P142W mutant, which included triclosan and compounds **PT70** (diphenyl ether) (*113*), **PT171** (2-pyridone) (*115*), **PT192** (2-pyridone with bridging oxygen) (*115*), and **PT166** (4-pyridone) (Table 5.3). Compounds **PT70** and **PT192** inhibited wild-type *Yp*FabV with IC_{50} values of 3 ± 0.5 µM and 19 ± 3 µM, respectively, while **PT171** had a high micromolar affinity against wild-type *Yp*FabV with IC_{50} value greater than 50

119

μM. However, the inhibitor specificity for P142W YpFabV followed the opposite trend, in which **PT171** inhibited P142W YpFabV with an IC_{50} value of 6 ± 2 μM. Also, **PT70** and **PT192** lost potency for P142W YpFabV compared to the wild-type YpFabV with IC_{50} values greater than 32 μM. Both wild-type YpFabV and P142W YpFabV were inhibited with a similar binding affinity using a 4-pyridone-based scaffold, **PT166**, with IC_{50} values ranging from 12-18 μM.

Table 5.3 Inhibitor scaffold preference for *Yp*FabV and P142W *Yp*FabV.

Inhibitor	Structure	IC$_{50}$ (µM) at 15 nM enzyme	
		Wt *Yp*FabV	P142W *Yp*FabV
Triclosan		5 ± 1	66 ± 12
PT70		3 ± 0.5	> 32
PT166		18 ± 2	12 ± 5
PT171		> 50	6 ± 2
PT192		19 ± 3	> 32
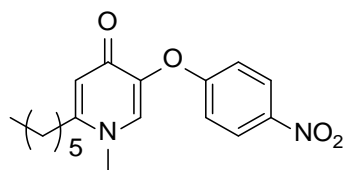
Figure 5.6 Structure of hit compound, PT156

121

PT156 is a slow-onset inhibitor against P142W YpFabV

We screened 4-pyridone-based inhibitors from our compound library against P142W *Yp*FabV, and we found one slow-onset inhibitor, **PT156** (Figure 5.6). Thermal shift assays revealed this compound preferentially binds to the enzyme-NADH complex with a p-value <0.0001 (Figure 5.7).
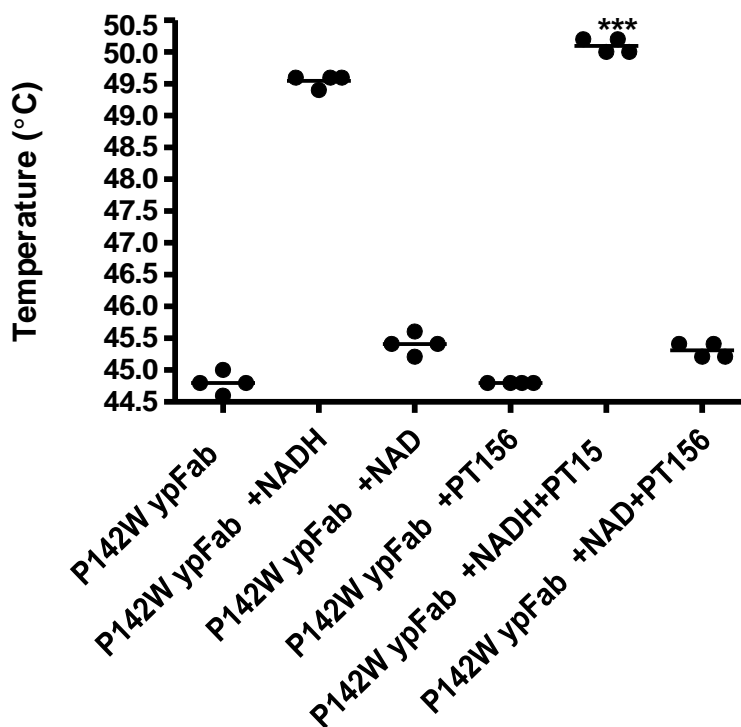
Figure 5.7 Midpoint temperatures of the protein-unfolding transition (T_m)
for P142W *Yp*FabV in the presence of inhibitor (25 μM) and NADH or NAD+ (2.5 mM). Significance was determined by an unpaired t-test analysis between untreated and treated groups. Data by Mrs. Shabnam Davoodi.

Since **PT156** binds preferentially to the enzyme-NADH complex, a qualitative complex formation assay was developed and used to evaluate if it is a slow-onset inhibitor based on the isolation of this cofactor-inhibitor complex. In this assay, we assume a slow binding inhibitor in complex with enzyme-NADH can be isolated using size-exclusion chromatography, whilst a rapid reversible inhibitor complex cannot be isolated. Additionally, this inhibitor complex can be monitored at the absorbance of 340 nm because the inhibitor would dissociate slowly from an enzyme-NADH complex. This assumption was validated with control samples, in which we recovered 76% of the enzyme with little breakthrough NADH from the size-exclusion spin column (Figure 5.8.A). In the presence of compound **PT156**, we observed recovery of the enzyme along with NADH, suggesting that **PT156** is a slow-onset inhibitor that dissociates slowly from an enzyme-NADH complex (Figure 5.8.B).

In contrast to wild-type *Yp*FabV, progress curve analysis confirmed that **PT156** was a slow-onset inhibitor of P142W *Yp*FabV (Figure 5.9). The kinetic and thermodynamic parameters were determined for the inhibition of P142W *Yp*FabV by **PT156** through progress curve analysis at varying inhibitor concentrations (Table 5.4). A plot of k_{obs} as a function of inhibitor concentration revealed a hyperbolic function as the inhibitor concentration increases (Figure 5.10). From these findings we concluded that **PT156** follows an induced-fit, two-step slow-onset mechanism, in which the enzyme undergoes isomerization (Scheme 5.1).
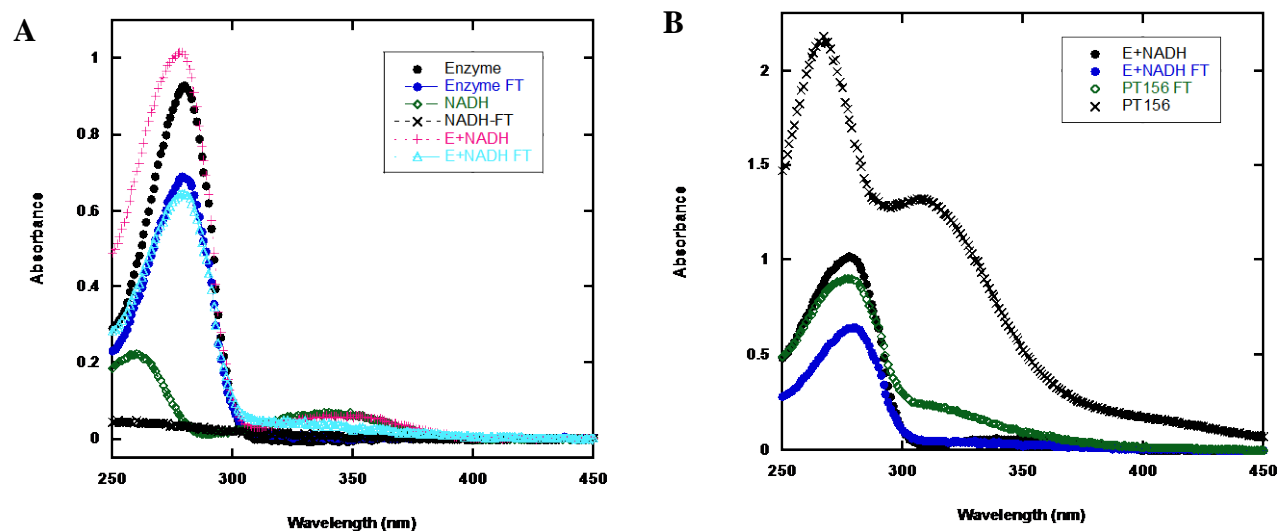
Figure 5.8 Complex formation assay for P142W *Yp*FabV
(A) Control samples to validate complex formation assay that consisted of free enzyme, NADH, and enzyme with NADH. (B) Samples consisted of enzyme with NADH was tested in the presence and absence of compound **PT156**. Abbreviations: FT, flow-through sample after desalting using size-exclusion chromatography.
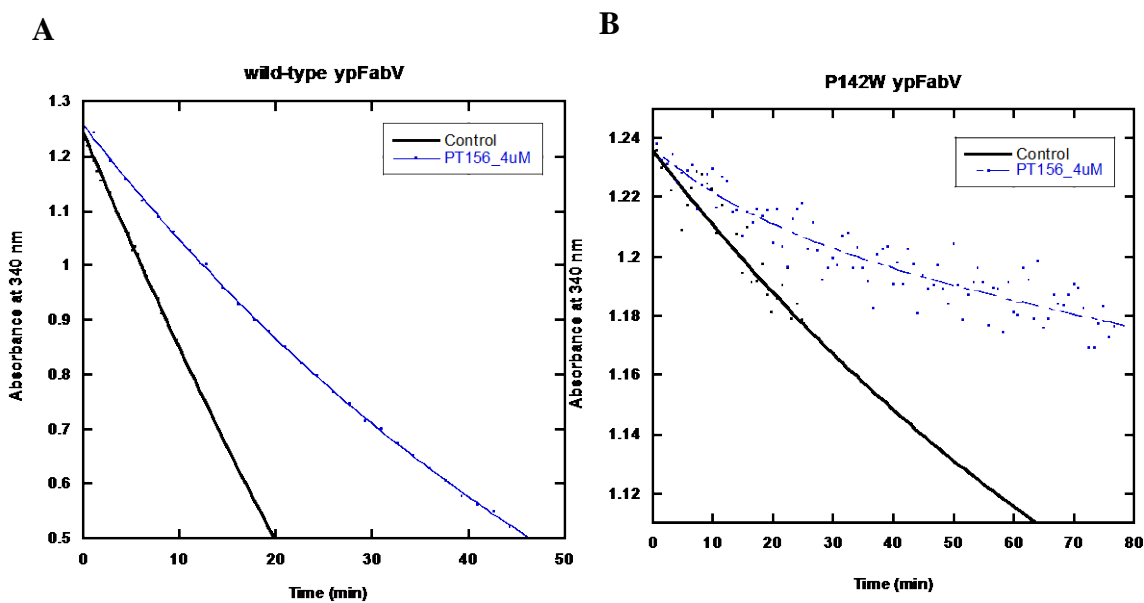
Figure 5.9 Representative examples of progress curves for an enzymatic reaction in the presence of PT156
(A) for wild-type *Yp*FabV ($R^2 = 0.99$) and (B) P142W *Yp*FabV ($R^2 = 0.90$).

124

Table 5.4 Kinetic parameters for PT156 against P142W YpFabV.

tR (min)	k_{on}^{app} (2nd step) $(nM^{-1}min^{-1})$	k_{on}^{app} (overall) $(nM^{-1}min^{-1})$	k_{off} (min^{-1})	K_i^{app} (nM)	$K_i^{*,app}$ (nM)
72 ± 5	0.081 ± 0.0078	1.1×10^{-5}	0.014 ± 0.00088	7630 ± 1010	918 ± 102
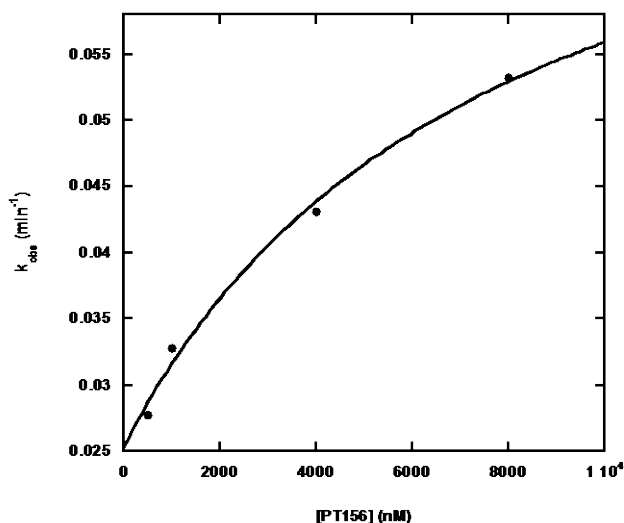
Figure 5.10 A replot of pseudo-first order rate constant (k_{obs}) for P142W YpFabV progress curves as a function of inhibitor concentration
R^2=0.99
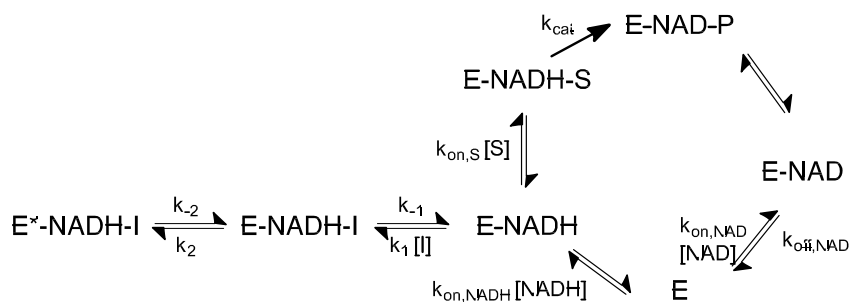
Scheme 5.1 Detailed kinetic mechanism for inhibition of P142W YpFabV by PT156

125

Discussion

Previous reports have shown that triclosan analogues are slow-onset inhibitors of FabI but not of the FabV ENR class (*40, 94*). Kinetic analysis of ENR classes can provide insights into the structural basis affecting the lifetime of the drug-target complex. Given that the binding kinetics of FabV is unknown, it is difficult to devise slow-onset inhibitors. In this study, we devised a method to induce a slow-onset inhibitor mechanism of a known rapid reversible inhibitor by mutating the protein of interest. This rational inhibitor design provides insights on how to translate a slow-onset inhibitor mechanism from a FabI to FabV ENR class.

The P142W *Yp*FabV mutant had a comparable catalytic efficiency as other FabVs, including wild-type *Yp*FabV, *B. pseudomallei* FabV, and *P. aeruginosa* FabV. The substrate binding mechanism of P142W *Yp*FabV switched to an ordered bi-bi mechanism as opposed to the random bi-bi mechanism observed for wild-type *Yp*FabV. The enzyme substrate binding preference may have shifted to allow NADH to bind to the enzyme first. Molecular dynamic simulations of wild-type and P142W *Yp*FabV in the absence and presence of NADH was performed by Dr. Cheng- Tsung Lai. These computational studies supported our structural and kinetic analysis, in which the edge of the indole covers the major portal and throughout the molecular dynamic simulation it remains predominantly in this position (not published).

Interestingly, replacement of P142 with Trp led to time dependent inhibition of the enzyme by **PT156**. Based on our modeling, we hypothesize that the P142W mutation results in

126

formation of a closed-state conformation, that leads to slow-onset inhibition. The kinetic parameters for inhibition of P142W FabV by **PT156** indicate that the slow-onset inhibition is driven by a reduction in the overall association rate constant (k_{on}) and weak initial binding affinity (K_i^{app}) with values of 1.1×10^{-5} nM^{-1}min^{-1} and 7630 ± 1010 nM, respectively. (*127, 129, 130*).

Our ability to engineer *Yp*FabV so that slow-onset inhibition is recovered provides an important platform for understanding time-dependent enzyme inhibition. Future work will focus on obtaining X-ray structures of this enzyme in order to confirm the role of loop dynamics in slow-onset inhibition.

Bibliography

1. Landsberg, H. (1949) Prelude to the Discovery of Penicillin., *Isis 40*, 225-227.

2. Bosch, F., and Rosich, L. (2008) The contributions of Paul Ehrlich to pharmacology: a tribute on the occasion of the centenary of his Nobel Prize, *Pharmacology 82*, 171-179.

3. Aminov, R. I. (2010) A brief history of the antibiotic era: lessons learned and challenges for the future, *Front Microbiol 1*, 134.

4. Wright, G. D. (2007) The antibiotic resistome: the nexus of chemical and genetic diversity, *Nat Rev Microbiol 5*, 175-186.

5. McGowan, J. E., Jr. (2006) Resistance in nonfermenting gram-negative bacteria: multidrug resistance to the maximum, *Am J Infect Control 34*, S29-37; discussion S64-73.

6. Chopra, I., Hodgson, J., Metcalf, B., and Poste, G. (1996) New approaches to the control of infections caused by antibiotic-resistant bacteria. An industry perspective, *JAMA 275*, 401-403.

7. Levy, S. B., and Marshall, B. (2004) Antibacterial resistance worldwide: causes, challenges and responses, *Nat Med 10*, S122-129.

8. McDevitt, D., and Rosenberg, M. (2001) Exploiting genomics to discover new antibiotics, *Trends Microbiol 9*, 611-617.

9. Pucci, M. J. (2006) Use of genomics to select antibacterial targets, *Biochem Pharmacol 71*, 1066-1072.

10.   Lange, R. P., Locher, H. H., Wyss, P. C., and Then, R. L. (2007) The targets of currently used antibacterial agents: Lessons for drug discovery, *Curr Pharm Design 13*, 3140-3154.

11.   Walsh, C. (2003) Where will new antibiotics come from?, *Nat Rev Microbiol 1*, 65-70.

12.   Gwynn, M. N., Portnoy, A., Rittenhouse, S. F., and Payne, D. J. (2010) Challenges of antibacterial discovery revisited, *Ann N Y Acad Sci 1213*, 5-19.

13.   Payne, D. J., Gwynn, M. N., Holmes, D. J., and Pompliano, D. L. (2007) Drugs for bad bugs: confronting the challenges of antibacterial discovery, *Nature reviews. Drug discovery 6*, 29-40.

14.   Chirala, S. S., Huang, W. Y., Jayakumar, A., Sakai, K., and Wakil, S. J. (1997) Animal fatty acid synthase: functional mapping and cloning and expression of the domain I constituent activities, *Proc Natl Acad Sci U S A 94*, 5588-5593.

15.   Tsay, J. T., Oh, W., Larson, T. J., Jackowski, S., and Rock, C. O. (1992) Isolation and characterization of the beta-ketoacyl-acyl carrier protein synthase III gene (fabH) from Escherichia coli K-12, *J Biol Chem 267*, 6807-6814.

16.   Clough, R. C., Matthis, A. L., Barnum, S. R., and Jaworski, J. G. (1992) Purification and characterization of 3-ketoacyl-acyl carrier protein synthase III from spinach. A condensing enzyme utilizing acetyl-coenzyme A to initiate fatty acid synthesis, *J Biol Chem 267*, 20992-20998.

17.   Waller, R. F., Keeling, P. J., Donald, R. G., Striepen, B., Handman, E., Lang-Unnasch, N., Cowman, A. F., Besra, G. S., Roos, D. S., and McFadden, G. I. (1998) Nuclear-

encoded proteins target to the plastid in Toxoplasma gondii and Plasmodium falciparum, *Proc Natl Acad Sci U S A 95*, 12352-12357.

18.   Payne, D. J., Warren, P. V., Holmes, D. J., Ji, Y., and Lonsdale, J. T. (2001) Bacterial fatty-acid biosynthesis: a genomics-driven target for antibacterial drug discovery, *Drug Discov Today 6*, 537-544.

19.   Heath, R. J., and Rock, C. O. (2004) Fatty acid biosynthesis as a target for novel antibacterials, *Curr Opin Investig Drugs 5*, 146-153.

20.   Heath, R. J., White, S. W., and Rock, C. O. (2001) Lipid biosynthesis as a target for antibacterial agents, *Prog Lipid Res 40*, 467-497.

21.   Cronan, J. E., and Waldrop, G. L. (2002) Multi-subunit acetyl-CoA carboxylases, *Prog Lipid Res 41*, 407-435.

22.   Marrakchi, H., Zhang, Y. M., and Rock, C. O. (2002) Mechanistic diversity and regulation of Type II fatty acid synthesis, *Biochem Soc T 30*, 1050-1055.

23.   Ruch, F. E., and Vagelos, P. R. (1973) Characterization of a Malonyl-Enzyme Intermediate and Identification of Malonyl Binding-Site in Malonyl Coenzyme-a-Acyl Carrier Protein Transacylase of Escherichia-Coli, *J Biol Chem 248*, 8095-8106.

24.   White, S. W., Zheng, J., Zhang, Y. M., and Rock, C. O. (2005) The structural biology of type II fatty acid biosynthesis, *Annu Rev Biochem 74*, 791-831.

25.   Price, A. C., Zhang, Y. M., Rock, C. O., and White, S. W. (2001) Structure of beta-ketoacyl-[acyl carrier protein] reductase from Escherichia coli: Negative cooperativity and its structural basis, *Biochemistry 40*, 12772-12781.

26. Leesong, M., Henderson, B. S., Gillig, J. R., Schwab, J. M., and Smith, J. L. (1996) Structure of a dehydratase-isomerase from the bacterial pathway for biosynthesis of unsaturated fatty acids: Two catalytic activities in one active site, *Structure 4*, 253-264.

27. Kimber, M. S., Martin, F., Lu, Y. J., Houston, S., Vedadi, M., Dharamsi, A., Fiebig, K. M., Schmid, M., and Rock, C. O. (2004) The structure of (3R)-hydroxyacyl-acyl carrier protein dehydratase (FabZ) from Pseudomonas aeruginosa, *J Biol Chem 279*, 52593-52602.

28. Massengo-Tiasse, R. P., and Cronan, J. E. (2009) Diversity in enoyl-acyl carrier protein reductases, *Cell Mol Life Sci 66*, 1507-1517.

29. Rafferty, J. B., Simon, J. W., Baldock, C., Artymiuk, P. J., Baker, P. J., Stuitje, A. R., Slabas, A. R., and Rice, D. W. (1995) Common Themes in Redox Chemistry Emerge from the X-Ray Structure of Oilseed Rape (Brassica-Napus) Enoyl Acyl Carrier Protein Reductase, *Structure 3*, 927-938.

30. Quemard, A., Sacchettini, J. C., Dessen, A., Vilcheze, C., Bittman, R., Jacobs, W. R., and Blanchard, J. S. (1995) Enzymatic Characterization of the Target for Isoniazid in Mycobacterium-Tuberculosis, *Biochemistry 34*, 8235-8241.

31. Kawaguchi, A., Yoshimura, T., Saito, K., Seyama, Y., Kasama, T., Yamakawa, T., and Okuda, S. (1980) Stereochemical Course of Enoyl Reduction Catalyzed by Fatty-Acid Synthetase - Stereochemistry of Hydrogen Incorporation from Reduced Pyridine-Nucleotide, *J Biochem-Tokyo 88*, 1-7.

131

32.   Banerjee, A., Dubnau, E., Quemard, A., Balasubramanian, V., Um, K. S., Wilson, T., Collins, D., Delisle, G., and Jacobs, W. R. (1994) Inha, a Gene Encoding a Target for Isoniazid and Ethionamide in Mycobacterium-Tuberculosis, *Science 263*, 227-230.

33.   Levy, C. W., Roujeinikova, A., Sedelnikova, S., Baker, P. J., Stuitje, A. R., Slabas, A. R., Rice, D. W., and Rafferty, J. B. (1999) Molecular basis of triclosan activity, *Nature 398*, 383-384.

34.   Heath, R. J., and Rock, C. O. (2000) Microbiology - A triclosan-resistant bacterial enzyme, *Nature 406*, 145-146.

35.   Parikh, S., Moynihan, D. P., Xiao, G. P., and Tonge, P. J. (1999) Roles of tyrosine 158 and lysine 165 in the catalytic mechanism of InhA, the enoyl-ACP reductase from Mycobacterium tuberculosis, *Biochemistry 38*, 13623-13634.

36.   Massengo-Tiasse, R. P., and Cronan, J. E. (2008) Vibrio cholerae FabV defines a new class of enoyl-acyl carrier protein reductase, *Journal of Biological Chemistry 283*, 1308-1316.

37.   Marrakchi, H., Dewolf, W. E., Jr., Quinn, C., West, J., Polizzi, B. J., So, C. Y., Holmes, D. J., Reed, S. L., Heath, R. J., Payne, D. J., Rock, C. O., and Wallis, N. G. (2003) Characterization of Streptococcus pneumoniae enoyl-(acyl-carrier protein) reductase (FabK), *Biochemical Journal 370*, 1055-1062.

38.   Heath, R. J., Su, N., Murphy, C. K., and Rock, C. O. (2000) The enoyl-[acyl-carrier-protein] reductases FabI and FabL from Bacillus subtilis, *J Biol Chem 275*, 40128-40133.

132

39. Tipparaju, S. K., Joyasawal, S., Forrester, S., Mulhearn, D. C., Pegan, S., Johnson, M. E., Mesecar, A. D., and Kozikowski, A. P. (2008) Design and synthesis of 2-pyridones as novel inhibitors of the Bacillus anthracis enoyl-ACP reductase, *Bioorg Med Chem Lett 18*, 3565-3569.

40. Lu, H., and Tonge, P. J. (2010) Mechanism and inhibition of the FabV enoyl-ACP reductase from Burkholderia mallei, *Biochemistry 49*, 1281-1289.

41. Lu, H., England, K., am Ende, C., Truglio, J. J., Luckner, S., Reddy, B. G., Marlenee, N. L., Knudson, S. E., Knudson, D. L., Bowen, R. A., Kisker, C., Slayden, R. A., and Tonge, P. J. (2009) Slow-onset inhibition of the FabI enoyl reductase from francisella tularensis: residence time and in vivo activity, *ACS Chem Biol 4*, 221-231.

42. Hirschbeck, M. W., Kuper, J., Lu, H., Liu, N., Neckles, C., Shah, S., Wagner, S., Sotriffer, C. A., Tonge, P. J., and Kisker, C. (2012) Structure of the Yersinia pestis FabV enoyl-ACP reductase and its interaction with two 2-pyridone inhibitors, *Structure 20*, 89-100.

43. Zhu, L., Lin, J. S., Ma, J. C., Cronan, J. E., and Wang, H. H. (2010) Triclosan Resistance of Pseudomonas aeruginosa PAO1 Is Due to FabV, a Triclosan-Resistant Enoyl-Acyl Carrier Protein Reductase, *Antimicrob Agents Chemother 54*, 689-698.

44. Xu, H., Sullivan, T. J., Sekiguchi, J., Kirikae, T., Ojima, I., Stratton, C. F., Mao, W., Rock, F. L., Alley, M. R., Johnson, F., Walker, S. G., and Tonge, P. J. (2008) Mechanism and inhibition of saFabI, the enoyl reductase from Staphylococcus aureus, *Biochemistry 47*, 4228-4236.

45.   Vilcheze, C., Morbidoni, H. R., Weisbrod, T. R., Iwamoto, H., Kuo, M., Sacchettini, J. C., and Jacobs, W. R. (2000) Inactivation of the inhA-encoded fatty acid synthase II (FASII) enoyl-acyl carrier protein reductase induces accumulation of the FASI end products and cell lysis of Mycobacterium smegmatis, *Journal of bacteriology 182*, 4059-4067.

46.   Zhang, Y. M., White, S. W., and Rock, C. O. (2006) Inhibiting bacterial fatty acid synthesis, *J Biol Chem 281*, 17541-17544.

47.   Bergler, H., Fuchsbichler, S., Hogenauer, G., and Turnowsky, F. (1996) The enoyl-[acyl-carrier-protein] reductase (FabI) of Escherichia coli, which catalyzes a key regulatory step in fatty acid biosynthesis, accepts NADH and NADPH as cofactors and is inhibited by palmitoyl-CoA, *Eur J Biochem 242*, 689-694.

48.   Heath, R. J., and Rock, C. O. (1995) Enoyl-acyl carrier protein reductase (fabI) plays a determinant role in completing cycles of fatty acid elongation in Escherichia coli, *J Biol Chem 270*, 26538-26542.

49.   Kwon, Y. J., Fang, Y., Xu, G. H., and Kim, W. G. (2009) Aquastatin A, a New Inhibitor of Enoyl-Acyl Carrier Protein Reductase from Sporothrix sp FN611, *Biol Pharm Bull 32*, 2061-2064.

50.   Kim, Y. J., Sohn, M. J., and Kim, W. G. (2012) Chalcomoracin and Moracin C, New Inhibitors of Staphylococcus aureus Enoyl-Acyl Carrier Protein Reductase from Morus alba, *Biol Pharm Bull 35*, 791-795.

134

51. Yao, J. J., Zhang, Q. Y., Min, J., He, J., and Yu, Z. N. (2010) Novel enoyl-ACP reductase (FabI) potential inhibitors of Escherichia coli from Chinese medicine monomers, *Bioorg Med Chem Lett 20*, 56-59.

52. Zheng, C. J., Sohn, M. J., Chi, S. W., and Kim, W. G. (2010) Methyl-Branched Fatty Acids, Inhibitors of Enoyl-ACP Reductase with Antibacterial Activity from Streptomyces sp A251, *J Microbiol Biotechn 20*, 875-880.

53. Kim, N., Sohn, M. J., Kim, C. J., Kwon, H. J., and Kim, W. G. (2012) Verrulactones A and B, new inhibitors of Staphylococcus aureus enoyl-ACP reductase produced by Penicillium verruculosum F375, *Bioorg Med Chem Lett 22*, 2503-2506.

54. Zheng, C. J., Sohn, M. J., and Kim, W. G. (2009) Vinaxanthone, a new FabI inhibitor from Penicillium sp., *J Antimicrob Chemoth 63*, 949-953.

55. Zheng, C. J., Sohn, M. J., and Kim, W. G. (2006) Atromentin and leucomelone, the first inhibitors specific to enoyl-ACP reductase (FabK) of Streptococcus pneumoniae, *J Antibiot (Tokyo) 59*, 808-812.

56. Zheng, C. J., Sohn, M. J., Lee, S., Hong, Y. S., Kwak, J. H., and Kim, W. G. (2007) Cephalochromin, a FabI-directed antibacterial of microbial origin, *Biochem Biophys Res Commun 362*, 1107-1112.

57. Dayan, F. E., Ferreira, D., Wang, Y. H., Khan, I. A., McInroy, J. A., and Pan, Z. (2008) A pathogenic fungi diphenyl ether phytotoxin targets plant enoyl (acyl carrier protein) reductase, *Plant Physiol 147*, 1062-1071.

58.   Baldock, C., Rafferty, J. B., Sedelnikova, S. E., Baker, P. J., Stuitje, A. R., Slabas, A. R., Hawkes, T. R., and Rice, D. W. (1996) A mechanism of drug action revealed by structural studies of enoyl reductase, *Science 274*, 2107-2110.

59.   Grassberger, M. A., Turnowsky, F., and Hildebrandt, J. (1984) Preparation and antibacterial activities of new 1,2,3-diazaborine derivatives and analogues, *J Med Chem 27*, 947-953.

60.   Baldock, C., de Boer, G. J., Rafferty, J. B., Stuitje, A. R., and Rice, D. W. (1998) Mechanism of action of diazaborines, *Biochem Pharmacol 55*, 1541-1549.

61.   Davis, M. C., Franzblau, S. G., and Martin, A. R. (1998) Syntheses and evaluation of benzodiazaborine compounds against M. tuberculosis H37Rv in vitro, *Bioorg Med Chem Lett 8*, 843-846.

62.   Rozwarski, D. A., Grant, G. A., Barton, D. H., Jacobs, W. R., Jr., and Sacchettini, J. C. (1998) Modification of the NADH of the isoniazid target (InhA) from Mycobacterium tuberculosis, *Science 279*, 98-102.

63.   Rawat, R., Whitty, A., and Tonge, P. J. . (2003) The isoniazid-NAD adduct is a slow, tight-binding inhibitor of InhA, the Mycobacterium tuberculosis enoyl reductase: adduct affinity and drug resistance, *Proc Natl Acad Sci U S A 100*, 13881-13886.

64.   McMurry, L. M., Oethinger, M., and Levy, S. B. (1998) Triclosan targets lipid synthesis, *Nature 394*, 531-532.

136

65.	Heath, R. J., Yu, Y. T., Shapiro, M. A., Olson, E., and Rock, C. O. (1998) Broad spectrum antimicrobial biocides target the FabI component of fatty acid synthesis, *Journal of Biological Chemistry 273*, 30316-30320.

66.	Chhibber, M., Kumar, G., Parasuraman, P., Ramya, T. N., Surolia, N., and Surolia, A. (2006) Novel diphenyl ethers: design, docking studies, synthesis and inhibition of enoyl ACP reductase of Plasmodium falciparum and Escherichia coli, *Bioorg Med Chem 14*, 8086-8098.

67.	Freundlich, J. S., Yu, M., Lucumi, E., Kuo, M., Tsai, H. C., Valderramos, J. C., Karagyozov, L., Jacobs, W. R., Jr., Schiehser, G. A., Fidock, D. A., Jacobus, D. P., and Sacchettini, J. C. (2006) Synthesis and biological activity of diaryl ether inhibitors of malarial enoyl acyl carrier protein reductase. Part 2: 2'-substituted triclosan derivatives, *Bioorg Med Chem Lett 16*, 2163-2169.

68.	Perozzo, R., Kuo, M., Sidhu, A., Valiyaveettil, J. T., Bittman, R., Jacobs, W. R., Jr., Fidock, D. A., and Sacchettini, J. C. (2002) Structural elucidation of the specificity of the antibacterial agent triclosan for malarial enoyl acyl carrier protein reductase, *J Biol Chem 277*, 13106-13114.

69.	Wang, L. Q., Falany, C. N., and James, M. O. (2004) Triclosan as a substrate and inhibitor of 3'-phosphoadenosine 5'-phosphosulfate-sulfotransferase and UDP-glucuronosyl transferase in human liver fractions, *Drug Metab Dispos 32*, 1162-1169.

70.	Takahata, S., Iida, M., Yoshida, T., Kumura, K., Kitagawa, H., and Hoshiko, S. (2007) Discovery of 4-Pyridone derivatives as specific inhibitors of enoyl-acyl carrier protein
137

reductase (FabI) with antibacterial activity against Staphylococcus aureus, *J Antibiot (Tokyo) 60*, 123-128.

71.   Kitagawa, H., Kumura, K., Takahata, S., Iida, M., and Atsumi, K. (2007) 4-Pyridone derivatives as new inhibitors of bacterial enoyl-ACP reductase FabI, *Bioorg Med Chem 15*, 1106-1116.

72.   Yum, J. H., Kim, C. K., Yong, D., Lee, K., Chong, Y., Kim, C. M., Kim, J. M., Ro, S., and Cho, J. M. (2007) In vitro activities of CG400549, a novel FabI inhibitor, against recently isolated clinical staphylococcal strains in Korea, *Antimicrob Agents Chemother 51*, 2591-2593.

73.   Kitagawa, H., Ozawa, T., Takahata, S., Iida, M., Saito, J., and Yamada, M. (2007) Phenylimidazole derivatives of 4-pyridone as dual inhibitors of bacterial enoyl-acyl carrier protein reductases FabI and FabK, *Journal of Medicinal Chemistry 50*, 4710-4720.

74.   Perry, R. D., and Fetherston, J. D. (1997) Yersinia pestis--etiologic agent of plague, *Clin Microbiol Rev 10*, 35-66.

75.   Drancourt, M., and Raoult, D. (2002) Molecular insights into the history of plague, *Microbes and Infection 4*, 105-109.

76.   Bacot, A. W., and Martin, C. J. (1914) LXVII. Observations on the mechanism of the transmission of plague by fleas, *J Hyg (Lond) 13*, 423-439.

77.   Rollins, S. E., Rollins, S. M., and Ryan, E. T. (2003) Yersinia pestis and the plague, *Am J Clin Pathol 119 Suppl*, S78-85.

78. Riedel, S. (2005) Plague: from natural disease to bioterrorism, *Proc (Bayl Univ Med Cent) 18*, 116-124.

79. Riedel, S. (2004) Biological warfare and bioterrorism: a historical review, *Proc (Bayl Univ Med Cent) 17*, 400-406.

80. Derbes, V. J. (1966) De Mussis and the great plague of 1348. A forgotten episode of bacteriological warfare, *JAMA 196*, 59-62.

81. Alibek, K. a. H., S. (1999) Biohazard., *New York: Random House*.

82. Pohanka, M., and Skladal, P. (2009) Bacillus anthracis, Francisella tularensis and Yersinia pestis. The most important bacterial warfare agents - review, *Folia Microbiol (Praha) 54*, 263-272.

83. Meyer, K. F. (1950) Modern therapy of plague, *JAMA 144*, 982-985.

84. Inglesby, T. V., Dennis, D. T., Henderson, D. A., Bartlett, J. G., Ascher, M. S., Eitzen, E., Fine, A. D., Friedlander, A. M., Hauer, J., Koerner, J. F., Layton, M., McDade, J., Osterholm, M. T., O'Toole, T., Parker, G., Perl, T. M., Russell, P. K., Schoch-Spana, M., Tonat, K., and Biodefense, W. G. C. (2000) Plague as a biological weapon - Medical and public health management, *Jama-J Am Med Assoc 283*, 2281-2290.

85. Galimand, M., Guiyoule, A., Gerbaud, G., Rasoamanana, B., Chanteau, S., Carniel, E., and Courvalin, P. (1997) Multidrug resistance in Yersinia pestis mediated by a transferable plasmid, *New Engl J Med 337*, 677-680.

86. Guiyoule, A., Gerbaud, G., Buchrieser, C., Galimand, M., Rahalison, L., Chanteau, S., Courvalin, P., and Carniel, E. (2001) Transferable plasmid-mediated resistance to

streptomycin in a clinical isolate of Yersinia pestis, *Emerging Infectious Diseases 7*, 43-48.

87.   Bergler, H., Wallner, P., Ebeling, A., Leitinger, B., Fuchsbichler, S., Aschauer, H., Kollenz, G., Hogenauer, G., and Turnowsky, F. (1994) Protein Envm Is the Nadh-Dependent Enoyl-Acp Reductase (Fabi) of Escherichia-Coli, *J Biol Chem 269*, 5493-5496.

88.   Tonge, P. J., Kisker, C., and Slayden, R. A. (2007) Development of modern InhA inhibitors to combat drug resistant strains of Mycobacterium tuberculosis, *Curr Top Med Chem 7*, 489-498.

89.   Parikh, S. L., Xiao, G., and Tonge, P. J. (2000) Inhibition of InhA, the enoyl reductase from Mycobacterium tuberculosis, by triclosan and isoniazid, *Biochemistry 39*, 7645-7650.

90.   Henis, Y. I., and Levitzki, A. (1976) An analysis on the slope of Scatchard plots, *Eur J Biochem 71*, 529-532.

91.   Lu, H., and Tonge, P. J. (2008) Inhibitors of FabI, an enzyme drug target in the bacterial fatty acid biosynthesis pathway, *Accounts Chem Res 41*, 11-20.

92.   Sivaraman, S., Zwahlen, J., Bell, A. F., Hedstrom, L., and Tonge, P. J. (2003) Structure-activity studies of the inhibition of FabI, the enoyl reductase from Escherichia coli, by triclosan: kinetic analysis of mutant FabIs, *Biochemistry 42*, 4406-4413.

93.   Ward, W. H. J., Holdgate, G. A., Rowsell, S., McLean, E. G., Pauptit, R. A., Clayton, E., Nichols, W. W., Colls, J. G., Minshull, C. A., Jude, D. A., Mistry, A., Timms, D.,

Camble, R., Hales, N. J., Britton, C. J., and Taylor, I. W. F. (1999) Kinetic and structural characteristics of the inhibition of enoyl (acyl carrier protein) reductase by triclosan, *Biochemistry 38*, 12514-12525.

94.   Liu, N., Cummings, J. E., England, K., Slayden, R. A., and Tonge, P. J. (2011) Mechanism and inhibition of the FabI enoyl-ACP reductase from Burkholderia pseudomallei, *J Antimicrob Chemother. 66*, 564-573.

95.   Cleland, W. W. (1963) The kinetics of enzyme-catalyzed reactions with two or more substrates or products. II. Inhibition: nomenclature and theory, *Biochimica et biophysica acta 67*, 173-187.

96.   Segel, I. H. (1975) *Enzyme Kinetics*, Wiley, New York.

97.   Gregoret, L. M., Rader, S. D., Fletterick, R. J., and Cohen, F. E. (1991) Hydrogen-Bonds Involving Sulfur-Atoms in Proteins, *Proteins 9*, 99-107.

98.   Holm, L., and Park, J. (2000) DaliLite workbench for protein structure comparison, *Bioinformatics 16*, 566-567.

99.   Li, H., Zhang, X., Bi, L., He, J., and Jiang, T. (2011) Determination of the crystal structure and active residues of FabV, the enoyl-ACP reductase from Xanthomonas oryzae, *PloS one 6*, e26743.

100.   Whitty, A., Fierke, C. A., and Jencks, W. P. (1995) Role of Binding-Energy with Coenzyme-a in Catalysis by 3-Oxoacid Coenzyme-a Transferase, *Biochemistry 34*, 11678-11689.

141

101. Pauling, L. (1946) Molecular architecture and biological reactions, *Chem Eng News 24*, 1375–1377.

102. Jencks, W. (1969) Binding Energy, Specificity, and Enzymatic Catalysis: The Circe Effect, In *Catalysis in chemistry and enzymology*, pp 615-726.

103. Meister, A. (1975) Advances in enzymology and related areas of molecular biology *43*, 219-410.

104. Lu, H. (2010) Mechanism and Inhibition of Bacterial Enoyl-ACP Reductases: Towards Novel Antibacterial Drugs, *PhD Dissertation*.

105. Menger, F. M. (1992) Analysis of ground-state and transition-state effects in enzyme catalysis, *Biochemistry 31*, 5368-5373.

106. Rendina A.R., P. B., Smallwood A., Zhao H., Qi H., Quinn C., Adams N.D., Concha N.O., Duraiswami C., Thrall S.H., Sweitzer S.M., and Schwartz B.J. (2013) Mutant IDH1 Enhances Production of 2-Hydroxyglutarate Due to Its Kinetic Mechanism, *Biochemistry*.

107. Richards, J. L., and Grimes, D. E. (2008) Bioterrorism: Class A agents and their potential presentations in immunocompromised patients, *Clin J Oncol Nurs 12*, 295-302.

108. Butler, T. (2009) Plague into the 21st century, *Clin Infect Dis 49*, 736-742.

109. Galimand, M., Carniel, E., and Courvalin, P. (2006) Resistance of Yersinia pestis to antimicrobial agents, *Antimicrob Agents Chemother 50*, 3233-3236.

110. Guiyoule, A., Rasoamanana, B., Buchrieser, C., Michel, P., Chanteau, S., and Carniel, E. (1997) Recent emergence of new variants of Yersinia pestis in Madagascar, *J Clin Microbiol 35*, 2826-2833.

111. Sullivan, T. J., Truglio, J. J., Boyne, M. E., Novichenok, P., Zhang, X., Stratton, C. F., Li, H. J., Kaur, T., Amin, A., Johnson, F., Slayden, R. A., Kisker, C., and Tonge, P. J. (2006) High affinity InhA inhibitors with activity against drug-resistant strains of Mycobacterium tuberculosis, *ACS Chem Biol 1*, 43-53.

112. am Ende, C. W., Knudson, S. E., Liu, N., Childs, J., Sullivan, T. J., Boyne, M., Xu, H., Gegina, Y., Knudson, D. L., Johnson, F., Peloquin, C. A., Slayden, R. A., and Tonge, P. J. (2008) Synthesis and in vitro antimycobacterial activity of B-ring modified diaryl ether InhA inhibitors, *Bioorg Med Chem Lett 18*, 3029-3033.

113. Luckner, S. R., Liu, N., am Ende, C. W., Tonge, P. J., and Kisker, C. (2010) A slow, tight binding inhibitor of InhA, the enoyl-acyl carrier protein reductase from Mycobacterium tuberculosis, *J Biol Chem 285*, 14330-14337.

114. Pan, P. (2012) Lead Optimization and Slow-Onset Inhibition of the Enoyl-ACP Reductase (InhA) from Mycobacterium Tuberculosis, *PhD Dissertation*.

115. Shah, S. (2012) Design, Synthesis and Evaluation of Inhibitors of the enoyl-ACP reductase from Staphylococcus aureus and Yesinia pestis, *Master Thesis*.

116. Sivaraman, S., Sullivan, T. J., Johnson, F., Novichenok, P., Cui, G., Simmerling, C., and Tonge, P. J. (2004) Inhibition of the bacterial enoyl reductase FabI by triclosan: a

structure-reactivity analysis of FabI inhibition by triclosan analogues, *J. Med. Chem. 47*, 509-518.

117. Wiersinga, W. J., van der Poll, T., White, N. J., Day, N. P., and Peacock, S. J. (2006) Melioidosis: insights into the pathogenicity of Burkholderia pseudomallei, *Nat Rev Microbiol 4*, 272-282.

118. Gilad, J., Harary, I., Dushnitsky, T., Schwartz, D., and Amsalem, Y. (2007) Burkholderia mallei and Burkholderia pseudomallei as bioterrorism agents: National aspects of emergency preparedness, *Israel Med Assoc J 9*, 499-503.

119. Cheng, A. C., and Currie, B. J. (2005) Melioidosis: Epidemiology, pathophysiology, and management, *Clin Microbiol Rev 18*, 383-+.

120. White, N. J., Chaowagul, W., Wuthiekanun, V., Dance, D. A. B., Wattanagoon, Y., and Pitakwatchara, N. (1989) Halving of Mortality of Severe Melioidosis by Ceftazidime, *Lancet 2*, 697-701.

121. Webber, M. A., and Piddock, L. J. V. (2003) The importance of efflux pumps in bacterial antibiotic resistance, *J Antimicrob Chemoth 51*, 9-11.

122. Moore, R. A., DeShazer, D., Reckseidler, S., Weissman, A., and Woods, D. E. (1999) Efflux-mediated aminoglycoside and macrolide resistance in Burkholderia pseudomallei, *Antimicrob Agents Ch 43*, 465-470.

123. Chan, Y. Y., Tan, T. M. C., Ong, Y. A., and Chua, K. L. (2004) BpeAB-OpRB, a multidrug efflux pump in Burkholderia pseudomallei, *Antimicrob Agents Ch 48*, 1128-1135.

144

124.   White, N. J. (2003) Melioidosis, *Lancet 361*, 1715-1722.

125.   Harland, D. N., Dassa, E., Titball, R. W., Brown, K. A., and Atkins, H. S. (2007) ATP-binding cassette systems in Burkholderia pseudomallei and Burkholderia mallei, *Bmc Genomics 8*.

126.   Rotz, L. D., Khan, A. S., Lillibridge, S. R., Ostroff, S. M., and Hughes, J. M. (2002) Public health assessment of potential biological terrorism agents, *Emerg Infect Dis 8*, 225-230.

127.   Tummino, P. J., and Copeland, R. A. (2008) Residence time of receptor-ligand complexes and its effect on biological function, *Biochemistry 47*, 5481-5492.

128.   Swinney, D. C. (2009) The role of binding kinetics in therapeutically useful drug action, *Curr. Opin. Drug Disc. 12*, 31-39.

129.   Copeland, R. A., Pompliano, D. L., and Meek, T. D. (2006) Drug-target residence time and its implications for lead optimization, *Nature reviews. Drug discovery 5*, 730-739.

130.   Zhang, R., and Monsma, F. (2009) The importance of drug-target residence time, *Curr. Opin. Drug Disc. 12*, 488-496.

131.   Lu, H., and Tonge, P. J. (2010) Drug-target residence time: critical information for lead optimization, *Curr Opin Chem Biol 14*, 467-474.

132.   Silver, L. L. (2011) Challenges of antibacterial discovery, *Clin Microbiol Rev 24*, 71-109.

133.   Gerusz, V., Denis, A., Faivre, F., Bonvin, Y., Oxoby, M., Briet, S., LeFralliec, G., Oliveira, C., Desroy, N., Raymond, C., Peltier, L., Moreau, F., Escaich, S., Vongsouthi, V., Floquet, S., Drocourt, E., Walton, A., Prouvensier, L., Saccomani, M., Durant, L.,

Genevard, J. M., Sam-Sambo, V., and Soulama-Mouze, C. (2012) From triclosan toward the clinic: discovery of nonbiocidal, potent FabI inhibitors for the treatment of resistant bacteria, *J Med Chem 55*, 9914-9928.

134. Escaich, S., Prouvensier, L., Saccomani, M., Durant, L., Oxoby, M., Gerusz, V., Moreau, F., Vongsouthi, V., Maher, K., Morrissey, I., and Soulama-Mouze, C. (2011) The MUT056399 Inhibitor of FabI Is a New Antistaphylococcal Compound, *Antimicrob Agents Ch 55*, 4692-4697.

135. Chang, A., Schiebel, J., Yu, W. X., Bommineni, G. R., Pan, P., Baxter, M. V., Khanna, A., Sotriffer, C. A., Kisker, C., and Tonge, P. J. (2013) Rational Optimization of Drug-Target Residence Time: Insights from Inhibitor Binding to the Staphylococcus aureus FabI Enzyme-Product Complex, *Biochemistry 52*, 4217-4228.

136. Copeland, R. A. (2005) Evaluation of enzyme inhibitors in drug discovery. A guide for medicinal chemists and pharmacologists, *Method Biochem Anal 46*, 1-265.

137. Kapoor, M., Reddy, C. C., Krishnasastry, M. V., Surolia, N., and Surolia, A. (2004) Slow-tight-binding inhibition of enoyl-acyl carrier protein reductase from Plasmodium falciparum by triclosan, *Biochem J 381*, 719-724.

138. Mima, T., and Schweizer, H. P. (2010) The BpeAB-OprB efflux pump of Burkholderia pseudomallei 1026b does not play a role in quorum sensing, virulence factor production, or extrusion of aminoglycosides but is a broad-spectrum drug efflux system, *Antimicrob Agents Chemother 54*, 3113-3120.

146

139. Cummings, J. E., Beaupre, A. J., Knudson, S. E., Liu, N., Yu, W., Neckles, C., Wang, H., Khanna, A., Bommineni, G. R., Trunck, L. A., Schweizer, H. P., Tonge, P. J., and Slayden, R. A. (2014) Substituted diphenyl ethers as a novel chemotherapeutic platform against Burkholderia pseudomallei, *Antimicrob Agents Chemother 58*, 1646-1651.

140. Chang, A. (2013) S. aureus FabI: Linking Catalysis, Inhibition and Cellular Effects, *Dissertation*.

141. Pan, P., Knudson, S. E., Bommineni, G. R., Li, H. J., Lai, C. T., Liu, N., Garcia-Diaz, M., Simmerling, C., Patil, S. S., Slayden, R. A., and Tonge, P. J. (2014) Time-Dependent Diaryl Ether Inhibitors of InhA: Structure-Activity Relationship Studies of Enzyme Inhibition, Antibacterial Activity, and in vivo Efficacy, *ChemMedChem 9*, 776-791.

142. Stewart, M. J., Parikh, S., Xiao, G. P., Tonge, P. J., and Kisker, C. (1999) Structural basis and mechanism of enoyl reductase inhibition by triclosan, *J Mol Biol 290*, 859-865.

143. Zierkiewicz, W. M., Danuta; and Hobza, Pavel (2004) The barrier to internal rotation and electronic effects in para-halogenophenols: theoretical study, *Chem Phys Lett 386*, 95-100.

144. Zierkiewicz, W. M., Danuta; Czarnik-Matusewicz, Bogusłwa; and Rospenk, Maria (2003) Molecular Structure and Infrared Spectra of 4-Fluorophenol: A Combined Theoretical and Spectroscopic Study, *J. Phys. Chem. 107*, 4547-4554.

145. Morrison, J. F., and Walsh, C. T. (1988) The behavior and significance of slow-binding enzyme inhibitors, *Adv Enzymol Relat Areas Mol Biol 61*, 201-301.

147

146.   Kapoor, M., Dar, M. J., Surolia, A., and Surolia, N. (2001) Kinetic determinants of the interaction of enoyl-ACP reductase from Plasmodium falciparum with its substrates and inhibitors, *Biochem Biophys Res Commun 289*, 832-837.

147.   Marcinkeviciene, J., Jiang, W., Kopcho, L. M., Locke, G., Luo, Y., and Copeland, R. A. (2001) Enoyl-ACP reductase (FabI) of Haemophilus influenzae: steady-state kinetic mechanism and inhibition by triclosan and hexachlorophene, *Arch Biochem Biophys 390*, 101-108.

148.   Pidugu, L. S., Kapoor, M., Surolia, N., Surolia, A., and Suguna, K. (2004) Structural basis for the variation in triclosan affinity to enoyl reductases, *J Mol Biol 343*, 147-155.

149.   Li, H. J., Lai, C. T., Pan, P., Yu, W., Liu, N., Bommineni, G. R., Garcia-Diaz, M., Simmerling, C., and Tonge, P. J. (2014) A Structural and Energetic Model for the Slow-Onset Inhibition of the Mycobacterium tuberculosis Enoyl-ACP Reductase InhA, *Acs Chem Biol*.